ARISTOTLE UNIVERSITY OF THESSALONIKI AND
ÉCOLE POLYTECHNIQUE FÉDÉRALE DE LAUSANNE

MASTER THESIS

NUMERICAL SIMULATIONS OF THE APOLLO 4 REENTRY TRAJECTORY

A thesis submitted in fulfillment of the requirements
for the degree of Master of Mechanical engineering

Author's name:

Ermioni Papadopoulou

Supervisors:

Dr. Penelope Leyland
Nikhil Banerji
Elise Fay

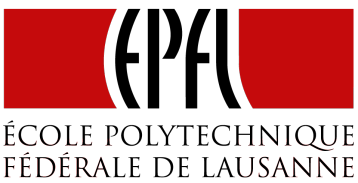

Lausanne, Suisse, March 2013

Acknowledgments

During this project there have been numerous people that contributed time and thoughts in order the present work to be fulfilled. My thanks are addressed to:

Dr. Penelope Leyland, who allowed me to work on this project as a member of the Interdisciplinary Aerodynamics Group (IAG) and her dedication and help throughout the project.

My colleagues and friends, Nikhil Banerji, for his supervision and moral support, Rik Geuns, Jeremy Mora-Monteros, Elise Fay, Oleg Kotsur, Gennady Plyushchev, for the every day support and the good times we spent in and out of the office and Angelo Casagrande for his support and patience.

Special thanks should be addressed to my supervisor in Greece, Prof. Anestis I.Kalfas, for giving me this opportunity to do my Master's thesis in EPFL and for his constant control and support for this project.

Abstract

Sample return capsules, as the Apollo Command Module have been widely used to advance the knowledge and planning of manned lunar and planetary return missions. Such reentry vehicles undergo extreme thermal conditions, caused by shock-heated air during their super-orbital atmospheric re-entry. Such extreme conditions can result in failure of the aeroshell structure and loss of important payload. This technological challenge is addressed by the use of ablative thermal protection systems (TPS), which dissipate the heat away from the vehicles front wall via ablative products release into the boundary layer. Additionally, such velocity and temperature magnitudes during reentry conditions introduce significant radiative heat loads, filling the shock layer with radiators that react with the ablative species injected by the capsule wall.

Therefore, accurate numerical modeling techniques are required, so that the thermophysical, thermochemical environment of a reentry capsule can be successfully reproduced and predicted. The present work aims to numerically rebuild certain significant trajectory points, containing the peak heating points of the Apollo 4 terrestrial re-entry. This requires the coupling of the resolved flow-field with radiative and ablative effects in order to accurately predict the convective and radiative heat flux for each trajectory point. The results will be compared to previous calculations and existing flight data.

The numerical simulations are performed in 2D thermal non-equilibrium with a compressible explicit Navier-Stokes solver, coupled to a radiation database and a thermal material response code to implement the ablative effects. The calculations are performed also in 3D, using a commercial implicit Navier-Stokes solver. The results will be used to reproduce the capsules trajectory and verify the accuracy of the associated Modeling Tools.

Contents

List of Figures

List of Tables

Chapter 1

Introduction

1.1 The Arc Project

The present work describes the contribution of IAG (Interdisciplinary Aerodynamics Group) at EPFL to the European project called ARC: "Ablation-Radiation coupling". This study is led by a consortium composed of the Interdisciplinary Aerodynamics Group of the Ecole Polytechnique Federale de Lausanne, the European Aerospace Research Establishment CIRA, the IRS Institute of the University of Stuttgart, an experienced Aerospace SME, FGE, together with subcontractors: the University of Queensland (Australia), a well known expert on ablation modelling, Dr. G. Duffa as a consultant, and ASTRIUM-St.

This project addresses the ablation-radiation coupling for high speed reentry and the physical phenomena that are induced by hypersonic flight conditions: ablation and radiation over a thermal protection system (TPS). Therefore, both testing projects in major European plasma wind tunnels and coupling simulations are led simultaneously, based on and compared with data obtained from past Earth return missions. This particular contribution of IAG deals with the radiation-ablation-flow-field numerical coupled simulation of the reentry of the Apollo Command Module.

1.2 Reentry flight missions

The exploration of space and the major aerospace industry advancements have been achieved through numerous projects of un-manned flights, with the use of command modules, aeroshell capsules. These capsules, as the Apollo Command Module, are basically test-probes for the actual manned aircrafts, such as the case of the Apollo program, or they are merely used for flight-testing of newly designed equipment and technologies and

real-time experiments. In any case, the actual data obtained from the flight measurements are invaluable and unique. Therefore, it is crucial that the measurements are smoothly expedited and the data obtained are non-affected by the flow conditions and securely transferred for post-processing.

The most dangerous phase of an Earth return mission is the atmospheric reentry stage, in which immense velocities along with extensive interaction with the gaseous atmosphere create an environment that changes the flow state around the probe. The atmospheric reentry is associated with velocities up to 12 km/s, thus, the recorded flight Mach numbers can be as high as 30 and more. The vehicle design that is most suited to such high velocity atmospheric entry trajectories is a simple blunt- body. That kind of front-body design provides a large frontal area, assisting the dissipation of the flows kinetic energy via interaction with the gaseous atmosphere. Apart from the blunt-shaped nose, the most recent reentry vehicles are equipped with ablative Thermal Protection Systems (TPS) to avoid possible damage of the capsule and insulate the vehicles content. The design of hypersonic aircrafts requires the implications of the TPS configuration on the surface roughness and on the state of the boundary layer to be accounted for, including the prediction of skin friction and heat-transfer rates [5]

1.3 Applied Tools

The tools used during this study are validated for aerothermodynamic numerical simulations. For the 2D simulations, a fluid solver developed by University of Queensland called *Eilmer3* was used. It contains radiative transfer models and an implemented ablating boundary condition. As for the 3D cases, the geometry of the capsule is designed with the use of *Solidworks*, a commercial 3D CAD software, while the meshing is done using the *ICEM CFD* software provided by ANSYS. The 3D simulations are performed using two 3D solvers: The first is a commercial solver, *CFD++*, which is developed in order to cope with hypersonic and reentry cases and includes boundary conditions for ablative walls (reacting walls). The second one is *NSMB*, which is an open-source 3D solver of the compressible Navier-Stokes equations, which is developed with the help of the EPFL IAG staff.

1.4 Scope and Overview of the present dissertation

The thesis presented is basically an implementation of recently developed numerical tools of compressible aero-thermodynamics in a specific reentry mission, the Apollo Command Module mission. The tools are applied in order to numerically rebuild some trajectory points of the Apollo 4 mission. Apart from a Two-Dimensional code, which is applied as part of the ARC project, two Three-Dimensional commercial solvers are used for the same

vehicle, in order comparison between the two codes to be made.

The main purpose of the present dissertation is the radiation analysis and trajectory rebuild of the Apollo 4 reentry flight mission. This includes the flow-field simulation and the flow-field and radiation coupling, as well as the flow-field and ablation coupling, in order to better estimate the thermodynamic state of the flow around the reentering vehicle. The heat flux calculation is done for certain trajectory points, which are of specific interest, as for example the peak radiation and the peak total heating trajectory points. The first part of the thesis includes these calculations in 2D, with the use of an academically developed solver.

The second part of this work is the 3D simulation of the specific trajectory flight of Apollo 4, using the actual dimensions of the capsule, both for only the front body and the whole body of the vehicle. The results obtained are to be compared with the existing flight data of the Apollo 4 mission and with results obtained from previous numerical solutions and semi-empirical formulas calculating convective and radiative heat fluxes during super-orbital reentries.

The present document is divided into 3 parts: The first part consists of Chapters 1, 2 and 3 and discusses some basic introductory information about hypersonic flights and the most elaborate Theoretical Background on the aero-thermodynamics of flights in such velocities and. Moreover, the governing equations and the Methodology applied are presented in this part. The second part includes Chapters 4 and 5 and it is the part where the results of the 2D and 3D simulations respectively are presented and further discussed. The last part includes Chapter 6, which refers to the Conclusions of the previously presented dissertation and the proposals for further analysis and work on the presented subject respectively. More specifically:

Chapter 1 is the Introduction chapter, presenting the subject of the thesis and some general information on Hypersonics and Aerothermodynamics. The scope and the

Chapter 2 is the chapter presenting all the theoretical background on Hypersonic flowfields, the investigation of such flows, the thermochemical models, the radiation transport modelling tools and the numerical and discretization methods applied.

Chapter 3 includes the overview of the codes and the solution procedure that has to be followed for both the 2D and 3D simulation cases.

Chapter 4 presents the results of the 2D simulation cases of Apollo 4 and the comparison of them with the existing flight data and previously calculated results.

Chapter 5 presents the results obtained for the 3D flow-field calculation of Apollo 4 and compares the different equation sets (inviscid or viscous flow, perfect gas or real gas thermochemical model etc.), as well as the actual three-dimensional codes and distinguish differences that make each applicable to compressible hypersonic applications or not.

Part I

Theory

Chapter 2

Theoretical Background

This chapter starts with the literature review for Hypersonic Flights in general, refers to some testing facilities for hypersonic flows and explains thoroughly the physical phenomena occurring during an atmospheric re-entry. It with the important information for the Apollo 4 test-flight.

2.1 Hypersonic Flow-fields

A flow-field where the Mach number is far greater than 1 (conventionally the threshold is considered to be $M \geq 5$):

$$M_\infty = \frac{U_\infty}{\alpha_\infty} \tag{2.1}$$

is defined as a Hypersonic Flow-field and is characterized by certain physical phenomena occurring in the shock and boundary layer of the flow in front of the reentering bodies. High speed reentry velocities lead to a strong shock wave upstream of the vehicle which strongly modifies the state of the fluid behind it. The internal thermodynamic energy of the free-stream fluid particles is small when compared with the kinetic energy of the free stream [4]. As the Mach number is increased, the flow density increases progressively, so the shock layer created by the strong bow shock over the blunt nose becomes thinner; the detachment distance between the wall boundary and the shock wave is really small.

2.1.1 Stagnation flow-field properties

In the stagnation region in front of the capsule's nose the free stream passes through the normal portion of the bow shock wave and decelerates isentropically to the point near the surface of the body, which constitutes the edge condition for the thermal boundary layer at the stagnation point. the pressure and the heating rate at the stagnation point are useful reference values for characterizing hypersonic flows.

2.1.2 The shock-standoff distance

The distance Δ of the shock and the body wall depends highly on the geometry of the body and the free-stream Mach number. A commonly used approximation describing the shock wave in the nose region of hypersonic vehicles is Billigs's equation ([6]), which for a sphere- cone model, the ratio $\frac{\Delta}{R}$, where Δ is the shock-standoff distance and R is the nose radius, is given:

$$\frac{\Delta}{R} = 0.143exp\left(\frac{3.24}{M^2}\right) \tag{2.2}$$

2.2 Aerothermodynamics of hypersonic flights

In hypersonic flights, the directional velocity of the fluid particles is much larger than the fluctuation velocities of the molecules of the flow. Thus, the flow kinetic energy before the bow shock is much larger than the internal thermodynamic energy of fluid particles. In atmospheric reentry conditions, i.e. high altitudes and hypersonic speeds three physical phenomena affect the aerothermodynamic state of the flow in the shock layer [2]:

- Viscous interactions:
  The viscous interactions between the viscous boundary layer and the inviscid unaffected flow-field are caused by the large amount of kinetic energy in the boundary layer. These viscous interactions affect the thickness of boundary layer, δ:

  $$\delta \approx \frac{{M_\infty}^2}{\sqrt{Re}} \tag{2.3}$$

  , which in hypersonic speeds, where M_∞ is extremely high, can be so thick that it practically merges with the shock wave, forming a merged shock layer, and, thus affecting the non-viscous part of the flow (outside of the boundary layer).

- Low density flow:
  At the atmospheric reentry altitudes the flows density is so low that the distance between particles is too big to approximate the gas as a continuum. Thus, implementation of the kinetic theory is required to describe the fluid state.

- High- temperature flow:
  Kinetic energy of the high speed flow is dissipated by the influence of friction within the boundary layer. The loss of kinetic energy through the shock is transformed into internal thermodynamic energy and creates a peak of temperature behind the shock. This viscous dissipation results in temperatures high enough to excite the vibrational energy of the atmospheric molecules and cause dissociation, and even ionization within the gas, both in the boundary and the shock layer. Thus, the shock and boundary layers of hypersonic flows are chemically reacting. If we consider the atmospheric air a mixture with a composition of N_2, O_2, NO, O *and* N ,

at certain levels of temperature the following changes in the state of the mixture can appear: These so-called High-temperature effects (or real-gas effects) induce

$T < 2000K$	$N_2 \approx 80\%$
	$O_2 \approx 20\%$
$T > 2000K$	Dissociation of O_2
	$O_2 \rightarrow 2O$
$T > 4000K$	$N_2 \rightarrow 2N$
	$N_2 + O_2 \rightarrow 2NO$
	$N + O \rightarrow NO^+ + e^-$
$T > 9000K$	$O \rightarrow O^+ + e^-$
	$N \rightarrow N^+ + e^-$

high heat-transfer rates to the surface as Aerodynamic Heating. The aerodynamic heating includes the heat transfer from the hot boundary layer to the cooler surface, convective heating, denoted by q_C and the thermal radiation emitted by the gas itself inverted into a radiative flux towards the surface, if the shock-layer temperature is high enough, radiative heating, denoted by q_R.

2.2.1 Stagnation region flow-field and thermodynamic state

The overall thermal environment during an atmospheric reentry highly depends on physical phenomena in the shock and boundary layer of the flow. The influence of ablation-product injection from the ablative heat shield into the flow-field (coupled ablation) and radiative energy exchange in the shock-layer (coupled radiation) are important to predict the heat fluxes in the flow-field and the material response of the heat shield. This is a crucial step for the design of a thermal protection system or for the development of new advanced ablative materials for heat shields. In the following section a small introduction on the ablation and radiation processes and the effects of those in the flow-field is taking place.

During reentry, atmospheric chemical species that are present in the shock layer zone have to undergo high heating rates so that thermal non-equilibrium processes occur like dissociation, recombination and ionization. Therefore, hot plasma is formed in front of the probe and can lead to extensive radiative heating. Thus, the probe is exposed to a very severe heating environment, including convective and radiative heating rates of similar magnitudes. That is why a successfully installed TPS is required to ensure the probes resistance to damage caused by friction and heating.

The recently applied ablators [9] of the TPS are made of phenolic impregnated carbon and are used to withstand the thermal conditions. The extensive use of carbon phenolic ablative materials strongly depends on the need of optimization and minimization of the mass of the TPS and the whole vehicle, which is a crucial parameter in space missions. As these shields release disintegrated materials and reactive species into the boundary layer, many chemical reactions can occur and lead to the formation of radiators and radiative

absorbers, so that the coupling between ablation and radiation cannot be ignored [18]. For a better understanding, *Figure 2.1* describes the overall processes occurring during reentry and *Figure 2.2* describes the chemical kinetic processes occurring in the shock and boundary layer of an reentering vehicle. TPS design is mainly based on numerical tools. A coupled approach between the solid domain and the fluid one has to be lead as they have both a strong thermal, physical, and chemical impact on each other.

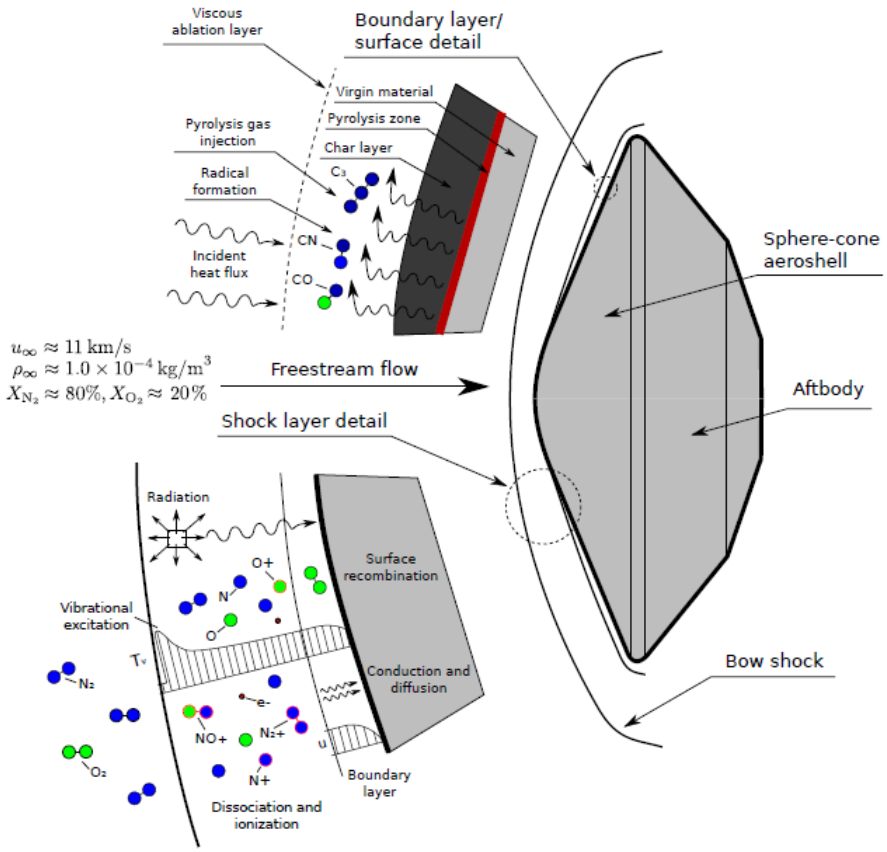

Figure 2.1: Illustration of the aerothermodynamic processes occurring in the shock layer and on the surface of a re-entry capsule at peak heating conditions, taken from [34]

Convective heating consists of the effects of conduction and diffusion in the shock layer. It is considered to be the sum of the conductive heat flux inwards and outwards of the surface wall, which is purely the result of temperature difference in the flow-field and diffusive heating, which results from the enthalpy injected in the flow-field by the pyrolysis and char ablative products.

On the other hand, radiative heating is highly dependent on the composition of the atmospheric gas. It mainly consists of the radiative heat flux created from the ionization and vibrational excitation of the atmospheric molecules, which is transferred towards the

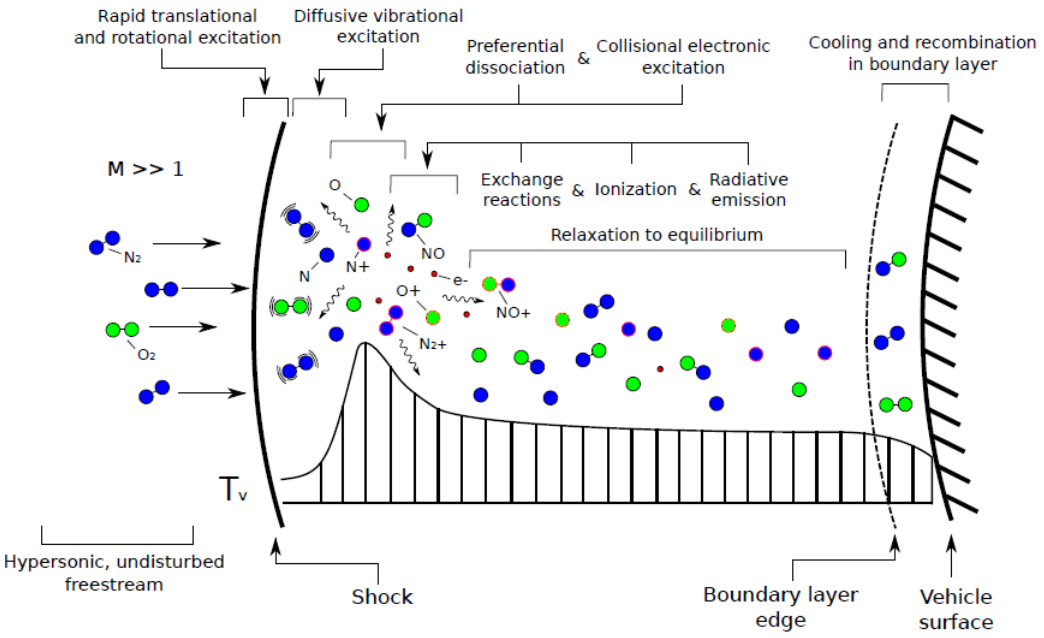

Figure 2.2: Illustration of the chemical kinetic processes along the stagnation streamline of an atmospheric reentry vehicle, taken from [34]

surface wall, and the re-radiation, the radiative emission exerted from the reentry body. Sutton [39] noted that radiative heat-transfer technology is important to ASTVs and to Martian return vehicles, because they enter the Earths atmosphere at relatively high velocities and have a large frontal area in order generate the desired large drag forces. As reported by Lee and Goodrich [20] measurements from the stagnation region during the re-entry of Apollo Spacecraft indicated a peak radiative heating rate of $115 W/cm^2$; this is roughly one-fourth of the maximum heating rate. The developed predictive techniques for estimating radiative heating, requires models for non-equilibrium thermochemistry, for radiative energy transfer mechanisms, and for absorption and retransmission of radiative energy within the shock layer.

The total heating at the wall at reentry environmental conditions is, therefore, the result of the summation of the convective (conductive and diffusive) and the radiative heat fluxes. It is described with the following equation:

$$q_w = q_{gas,cond} + q_{gas,diff} + q_{gas,rad} - q_{w,rad}$$

,where:

- $q_{gas,cond}$ is the conductive heat flux: $q_{gas,cond} = -\kappa \left(\frac{\partial T}{\partial y}\right)_w$
- $q_{gas,diff}$ is the diffusive heat flux and is formed by the contribution of each species i

- $q_{gas,rad}$ is the radiative heating induced by the vibrational excitation of the molecules in the shock layer: $q_{gas,rad} = \frac{E_{rad}}{2R\frac{\rho_\infty}{\rho_{BS}}}$, where E_{rad} is the radiative energy, R is the nose radius and ρ_{BS} is the density at the bow shock

- $q_{w,rad}$ is the radiation of the body surface: $q_{w,rad} = \epsilon\sigma T_w^4$, where ϵ is the emissivity and σ is the Stefan-Boltzmann constant: $\sigma = 5.67 \cdot 10^{-8}\frac{W}{m^2K^4}$.

2.3 Investigation of Reentry Shock Layers

The first reentry flights aerodynamic and thermodynamic environments were estimated with the use of semi-empirical analytical relations. However, the results from these formulas were not considered trustworthy enough to be applied for the calculation of the thermal protection systems for the reentry capsules of the period.

The next step to investigate the physical phenomena and accurately predict the aerothermodynamic environment around a reentering body was the flight experiments. The *Fire II* flight experiment [37], a scaled-down Apollo-like aeroshell, was executed in 1965. The total incident heat flux was measured with the use of calorimeters, while three total and one spectral radiometer (with spectral wavelength ranges of $200 \leq \ell \leq 4000$ nm and $200 \leq \ell \leq 600$ nm respectively) measured the integrated radiance and the radiative intensity and heat flux on the front and back body of the capsule. The difference of the measurements of the calorimeters and radiometers gave the vacuum ultraviolet radiation (spectral range lower than 200 nm). The full-scaled *Apollo Command Module* flight experiment was executed in 1967 [15]. Spectral measurements were performed with one radiometer embedded at the stagnation point of the capsule. In contrast with the Fire II capsule, the Apollo 4 Module had an *ablative heat shield*.

In recent years the analysis of the hypersonic reentries is performed with the combination of numerical modelling and the development of physical models and measuring experiments to validate the models.The measuring techniques nowadays include not only flight-experiments (e.g. [24]), which involve measurements of the shock layer and vehicle surface during an actual atmospheric entry maneuver but also, and most commonly applied, ground-based testing. In ground-based experiments measurements of shock layers, high-temperature gases or sub-scaled models are performed in a laboratory environment. Both of these approaches have benefits and disadvantages. Flight experiments allow the conditions encountered in flight to be almost exactly replicated,however detailed measurements of the shock layer plasma are difficult to perform. In contrast, ground-based experiments allow detailed measurements to be made by virtue of the laboratory environment, although the conditions encountered in flight cannot be replicated in full.

Shock tubes are the primary facilities for investigating the high enthalpy radiating shock

layers during reentry. The operation of a shock tube includes a shock being driven directly through the test gas at pressures and velocities encountered in super-orbital flight. Spectral measurements can be made of the radiation emitted in the shock layer; from the shock frame-of-reference, the post-shock relaxation phenomena encountered in flight along the stagnation streamline are exactly replicated [26].

The computational modelling of radiating shock layers requires the numerical solution of an appropriate set of governing equations. Hypersonic flow-fields in the continuum regime are well described by the compressible Navier-Stokes equations, whereas in the flow regimes that the mean free path of the molecules becomes comparable to the characteristic scale of the flow, statistical methods such as the Monte-Carlo method should be applied. In order the numerical simulations to be accurate enough, a lot of work has put on thermochemical non-equilibrium modelling, with the latest advances in this area to propose the use of a combination of Boltzmann distributions and kinetic modelling. On the other hand, the radiation modelling is affected by: (1) the internal state populations of chemical species, (2) the spectral distribution of the electromagnetic energy and (3) the transport of the electromagnetic energy through the plasma. More details about the numerical modelling tools applied are discussed in chapter 3. *Numerical rebuild* and *simulation* of weakly ionized gases over reentry vehicles has been successfully performed for numerous missions, including *FIRE* [37], [22], *Apollo Command Module* [29], [28], *Galileo* [30], *Stardust* [23] and *Mars Science Laboratory* [10].

2.4 The Apollo Command Module Mission

Apollo 4 was an instrumented prototype command module that was flown in 1967 [33]. This flight was a test of the Saturn V launch vehicle and the re-entry operations. The vehicle geometry is a 57 deg sphere-segment with a re-entry velocity of 11.14 km/s. The geometry of the Apollo 4 capsule is presented in *Figure 2.3*. It was designed as an axisymmetric vehicle with an offset center of gravity to provide lift during reentry. The vehicle followed a lifting trajectory with a nominal angle of attack of 25.5 deg during reentry. This trajectory induced an asymmetric shape to the flow-field around the capsule. The asymmetric flowfield and the induced aerothermodynamic phenomena around the reentry body are described in *Figure 2.4*: The blunt entry face contains a stagnation region with a high-heating are near the windward corner and subsonic and supersonic flow regions, while the conical section appears to be divided into two separate portions: the windward one, with an attached-flow regime, and the leeward one, with a separated-flow regime and low heating.

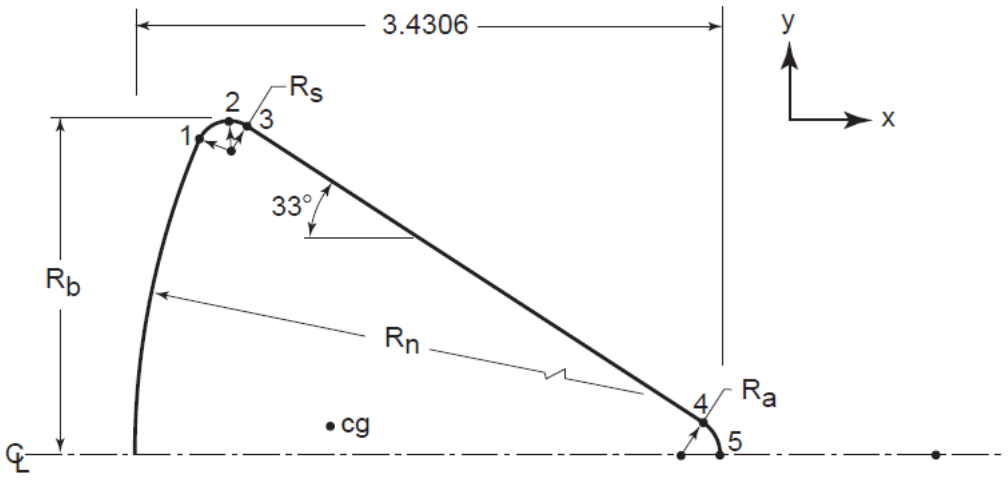

Location	x	y	s
1	0.3743	1.8368	1.8872
2	0.5543	1.9558	2.1158
3	0.6608	1.9242	2.2284
4	3.3254	0.1938	5.4056
5	3.3406	0.0000	5.6355
cg	1.1455	0.1600	-

D_b = 3.9116
R_b = 1.9558
R_n = 4.6939
R_s = 0.1956
R_a = 0.2311

Dimensions in m

Figure 2.3: The Apollo Command Module geometry, caption taken from [28]

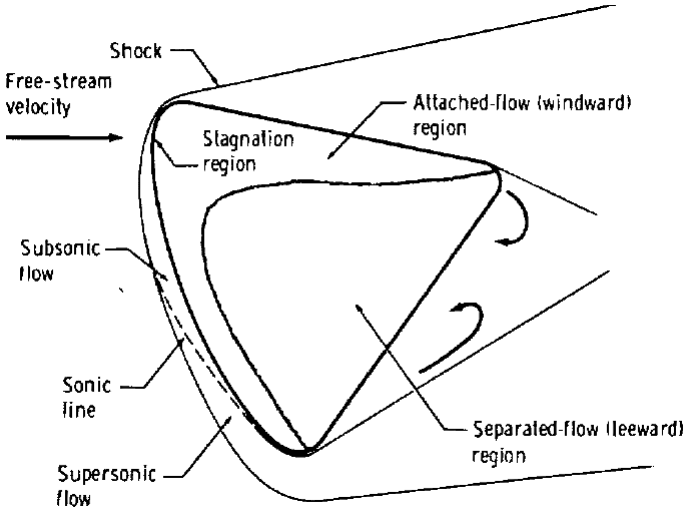

Figure 2.4: The distinguished flow regions observed in front of the reentry blunt face of Apollo 4, taken from [33]

Aerothermodynamic measurements were obtained on the Apollo 4 spacecraft during atmospheric entry at super-orbital velocities [21],[20] to prove and confirm the predicted heating environment that was used for the design of the ablative Thermal Protection System of the capsule [3], [9]. The Apollo program provided the first full-scale measurements at super-

orbital speed for a test case with an ablative heat shield. The obtained measurements, including pressure distribution and convective and radiative heating were conducted with the use of pressure transducers, radiometers and surface-mounted calorimeters located at the pitch lane and at various rays around the command module, as it is depicted in *Figure 2.5*.

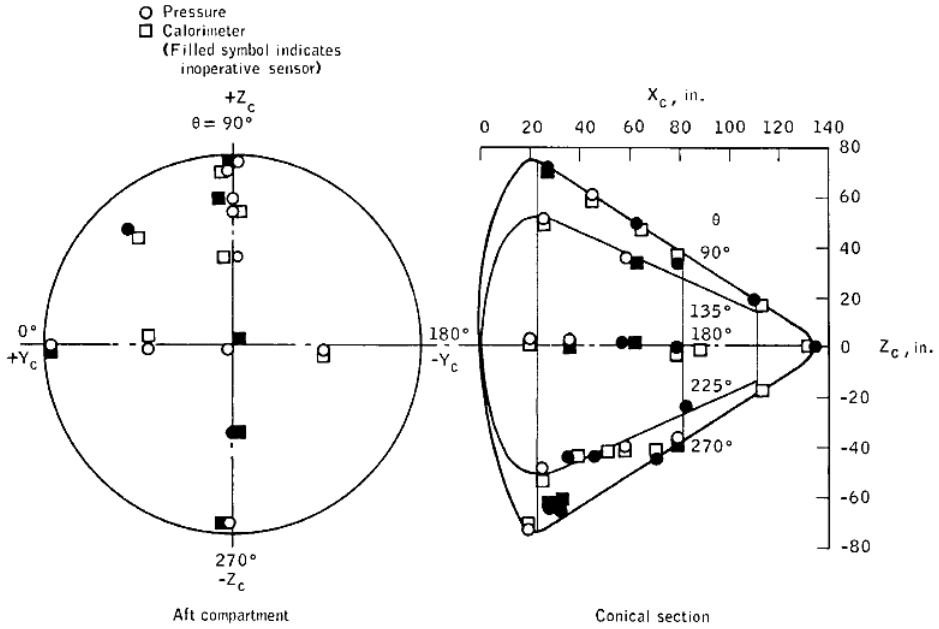

Figure 2.5: The distinguished flow regions observed in front of the reentry blunt face of Apollo 4, taken from [21]

The radiometer used for the measurements was embedded within the ablating TPS, and the interaction of the ablation products with the optics was a concern. However, post flight inspection revealed an absence of carbon deposits on the radiometer window. Therefore, it is unlikely that there was a strong concentration of carbon bearing species in the radiometer cavity. The gas within the radiometer cavity was most likely dominated by molecular hydrogen. The absorption properties of molecular hydrogen over the wavelength range transmitted by the quartz window are low. As such, absorption in the radiometer cavity is neglected for the purposed of this rebuild. The radiometer was mounted on the forebody, at a distance of 1.397 m from the axis of symmetry. At the angle of attack attained at peak heating (25.5 deg), the radiometer is over the stagnation point.

As the radiative heat flux at the stagnation point of a blunt body is governed primarily by the shock standoff, it becomes possible to define a 2D equivalent sphere. From Schlieren studies carried out by Ried et al. [36], Park [29] chose a sphere of 2.85 m radius, which gave the same shock standoff as seen on the Apollo 4 geometry at 25.5 deg angle of attack.

This equivalent sphere is also used for the 2D calculations of the present project, in order for the comparison of the results with the results achieved by Park and other correlations to be made successfully.

The radiative flux was obtained from flight data and was numerically rebuilt at three altitudes of the trajectory in previous works [36] and [29]. The trajectory points implemented for the sake of the present study are presented in 2.1 below. It is noticed that the second of the presented trajectory points was the peak radiative heating point of the reentry flight trajectory.

Trajectory point	1_{st}	2_{nd}	3_{rd}
Mission time (s)	30024	30032	30040
Altitude (km)	64.556	59.223	56.057
Density (kg/m^3)	$1.73 \cdot 10^{-4}$	$3.41 \cdot 10^{-4}$	$5.01 \cdot 10^{-4}$
Velocity (km/s)	10.511	10.252	9.798
Temperature (K)	234.51	249.16	257.86
Ablation rate $(kgm^{-2}s^{-1})$	0.0272	0.0300	0.0286
Wall Temperature (K)	2300	2500	2550
Flight Recorded Radiative Intensity $(0.2 - 4\mu m)$ $(Wcm^{-2}sr^{-1})$	10.5	25.0	16.0

Table 2.1: The Apollo Command Module trajectory points to be numerically rebuilt

Chapter 3

Equations and Methods

This chapter refers to the governing equations of the flow-field numerical modelling for Hypersonic fields and real gases and the numerical methods applied for the discretization and solution of the set of equations. Finally, the chemical models and heating transport models applied in the present work are shortly discussed. Emphasis is given on the models implemented in order to set up a case in the flow-field solver used for the 2D calculations, `Eilmer3` *and for the 3D calculations, using the 2 commercial does,* `CFD++` *and* `NSMB`*. The general procedure to run a simulation on* `Eilmer3` *is analyzed in Chapter 4, whereas the procedure for the 3D cases is discussed in Chapter 5.*

3.1 Compressible Navier-Stokes equations

During atmospheric reentry, the fluid flow is compressible, as the fluid density varies due to compressible phenomena induced in the flow-field by the strong bow shock wave in front of the capsule's face. The evolution of a compressible hypersonic flow is described with the compressible Navier-Stokes equations. This set of partial differential equations is derived by applying the continuity equation to conserved quantities of mass, momentum and energy of the mixture. According to the thermodynamic model implemented, there can be more than one energy and mass continuity equations. The generic differential form of the continuity equation is expressed as:

$$\frac{\partial \phi}{\partial t} + \nabla \cdot \vec{F} = \Omega \tag{3.1}$$

, where ϕ is the conserved quantity, $\vec{F}$ is a vector describing the flux of ϕ and Ω is a source term describing the creation and destruction of ϕ.

The conserved quantities to be applied to Equation 3.1 when deriving the compressible Navier Stokes equations are dependent on the degree of thermochemical non-equilibrium to be considered. For a gas in thermochemical equilibrium, the conserved quantities are

simply the total mass in terms of the total density ρ, momentum $\rho\vec{u}$ and energy E of the mixture. For atmospheric reentry conditions, an accurate description of the flowfield requires the inclusion of both thermal and chemical non-equilibrium. For chemical non-equilibrium, the continuity equation of each species' mass ρ_s must also be considered. The total mass continuity equation is no longer required, as the total density of the mixture can be retrieved from the sum of the species densities:

$$\rho = \sum_{s}^{N_{species}} \rho_s \tag{3.2}$$

For thermal non-equilibrium, the continuity of each independent thermal mode energy e_m must also be applied. For N_{modes} thermal modes, however, only $(N_{modes} - 1)$ additional equations are required, as the total internal energy e can be derived from the definition of the total energy:

$$E = e + \frac{1}{2}\vec{u}\cdot\vec{u} = \sum_{m}^{N_{modes}} e_m + \frac{1}{2}\vec{u}\cdot\vec{u} \tag{3.3}$$

Just for a better understanding, the continuity equations of mass, momentum and energy are presented as follows, in their form for incompressible flow:

Mass:

$$\frac{\partial\rho}{\partial t} + \overrightarrow{\nabla}.(\rho\overrightarrow{v} + \overrightarrow{J}) = \dot{\omega} \tag{3.4}$$

,where $\overrightarrow{v}$ is the velocity vector, $\overrightarrow{J}$ the diffusion vector and $\dot{\omega}$ is the mass production source term.

Momentum:

$$\frac{\partial\rho\overrightarrow{v}}{\partial t} + \overrightarrow{\nabla}.(\rho\overrightarrow{v}\wedge\overrightarrow{v}) + \overrightarrow{\nabla}.(p\underline{\underline{I}} - \underline{\underline{\tau}}) = \rho\overrightarrow{f} \tag{3.5}$$

,where E is the total energy, H is the total enthalpy, $\overrightarrow{f}$ is the external force vector and $\underline{\underline{\tau}}$ is the viscous stress tensor defined as follows:

$$\underline{\underline{\tau}} = \mu(\overrightarrow{\nabla}.(\rho\overrightarrow{v}\wedge\overrightarrow{v}) + \overrightarrow{\nabla}.(\rho\overrightarrow{v}\wedge\overrightarrow{v})) + \eta(\overrightarrow{\nabla}.\overrightarrow{v})\underline{\underline{I}} \tag{3.6}$$

Here, μ is the dynamic viscosity and η is the bulk viscosity.

Energy:

$$\frac{\partial\rho E}{\partial t} + \overrightarrow{\nabla}.(\overrightarrow{v}\rho H - \underline{\underline{\tau}}.\overrightarrow{v}) - = \rho\overrightarrow{f}.\overrightarrow{v} \tag{3.7}$$

3.2 Implemented equations

For an axisymmetric flowfield case, the Navier-Stokes equations can be summarized in a compact form as follows:

$$\frac{\partial \overrightarrow{U}}{\partial t} + \overrightarrow{\nabla}.(\overrightarrow{F_i} - \overrightarrow{F_v}) = \overrightarrow{Q} \tag{3.8}$$

Where:

- $\overrightarrow{U} = \begin{pmatrix} \rho \\ \rho \overrightarrow{v} \\ \rho E \end{pmatrix}$: the conservative variables
- $\overrightarrow{F_i} = \begin{pmatrix} \rho \overrightarrow{v} \\ \rho \overrightarrow{v} \wedge \overrightarrow{v} + p\underline{\underline{I}} \\ \rho \overrightarrow{v} H \end{pmatrix}$: the non-viscous flux vector
- $\overrightarrow{F_v} = \begin{pmatrix} -\overrightarrow{J} \\ \underline{\underline{\tau}} \\ \underline{\underline{\tau}}.\overrightarrow{v} \end{pmatrix}$: the viscous flux vector
- $\overrightarrow{Q} = \begin{pmatrix} \dot{\omega} \\ \rho \overrightarrow{f} \\ \rho \overrightarrow{f}.\overrightarrow{v} \end{pmatrix}$: the source term

,where the symbols used are summarized in 3.1

$\vec{v}$	Velocity vector $\vec{v} = (u, v, w)$
p	Pressure
ρ	Density
$\vec{f}$	External force vector
$\underline{\underline{\tau}}$	Viscous stress tensor: $\underline{\underline{\tau}} = \mu \left[\vec{\nabla} \cdot (\rho \vec{v} \otimes \vec{v}) + \vec{\nabla} \cdot (\rho \vec{v} \otimes \vec{v})^T \right] + \eta \left(\vec{\nabla} \cdot \vec{v} \right) \underline{\underline{I}}$
μ	Dynamic Viscosity
ν	Kinematic viscosity
H	Total enthalpy
E	Total energy

Table 3.1: Symbols explanation of Navier-Stokes equations

The symbol $\otimes$ defines a tensor product, i.e. $(\vec{u} \otimes \vec{v})_{ij} = \vec{u}_i \vec{v}_j$

3.2.1 Axisymmetric 2D flows- Two temperature thermodynamic model

The following section refers to the formulation of the code for Axisymmetric Two-Dimensional flows using finite-rate chemistry and multi-species gas, in the way that the equations are formed for the Eilmer3 code.

The Eilmer3 code is formulated around the integral form of the Navier-Stokes equations [17], which is expressed as:

$$\frac{\partial}{\partial t}\int_V U dV = -\int_S \left(\overline{F}_i - \overline{F}_v\right)\cdot \hat{n}\ dA + \int_V Q dV \tag{3.9}$$

,where S is the bounding surface and $\hat{n}$ is the outward-facing unit normal of the control surface. For axisymmetric flow, V is the volume and A the area of the cell boundary per unit radian in the circumferential direction.

The vector of conserved quantities U for the thermal non-equilibrium model is:

$$U = \begin{bmatrix} \rho \\ \rho u_x \\ \rho u_y \\ \rho E \\ \rho e_{ve} \\ \rho Y_s \end{bmatrix} \tag{3.10}$$

where, ρ is density, u is velocity, E is total energy, e_{ve} is the vibration-electron-electronic energy and Y_s is the species s mass-fraction. Therefore, the conserved quantities considered are respectively the density, x- and y-momentum per volume, total energy per volume, vibrational-electron-electronic energy and mass density of species s.

The flux vector is divided into an inviscid contribution $\overline{F}_i$ and a viscous one $\overline{F}_v$. The inviscid contribution $\overline{F}_i$ for a two-temperature model is a follows:

$$\overline{F}_i = \begin{bmatrix} \rho u_x \\ \rho u_x^2 + p \\ \rho u_y u_x \\ \rho E u_x + p u_x \\ \rho e_{ve} u_x + p_e u_x \\ \rho Y_s u_x \end{bmatrix} \hat{i} + \begin{bmatrix} \rho u_y \\ \rho u_x u_y \\ \rho u_y^2 + p \\ \rho E u_y + p u_y \\ \rho e_{ve} u_y + p_e u_y \\ \rho Y_s u_y \end{bmatrix} \hat{j} \tag{3.11}$$

,where p_e is the electron pressure.

The viscous contribution $\overline{F}_v$ for a two-temperature model is as follows:

$$\overline{F}_v = \begin{bmatrix} 0 \\ \tau_{xx} \\ \tau_{yx} \\ \tau_{xx}u_x + \tau_{yx}u_y + q_x \\ q_{x,ve} \\ J_{x,s} \end{bmatrix} \hat{i} + \begin{bmatrix} 0 \\ \tau_{xy} \\ \tau_{yy} \\ \tau_{xy}u_x + \tau_{yy}u_y + q_y \\ q_{y,ve} \\ J_{y,s} \end{bmatrix} \hat{j} \tag{3.12}$$

Here, τ refers to the axisymmetric viscous stresses components, q denotes the heat-flux and J is the diffusion flux. In order to apply the operator-splitting integration approach, which is used in the Eilmer3 code, the vector of source terms is separated into geometric, chemical kinetic, thermal energy exchange and radiation contributions:

$$Q = Q_{geom.} + Q_{chem.} + Q_{therm.} + Q_{rad.} \tag{3.13}$$

$Q_{geom.}$ is the source term for axisymmetric geometries:

$$Q_{geom.} = \begin{bmatrix} 0 \\ 0 \\ (p - \tau_{\theta\theta})A_{xy}/V \\ 0 \\ 0 \\ 0 \end{bmatrix} \tag{3.14}$$

Here, A_{xy} is the projected area of the cell in the (x,y) plane.

$Q_{chem.}$ is the chemistry source term:

$$Q_{chem.} = \begin{bmatrix} 0 \\ 0 \\ 0 \\ 0 \\ \sum_{i}^{N_{mol}} \Omega_i^{VC} + \sum_{j}^{M_{ion}} \Omega_j^{EC} \\ M_s\dot{\omega}_s \end{bmatrix} \tag{3.15}$$

Here, Ω^{VC} is the vibration-chemistry energy exchange source term, Ω^{EC} is the electron-chemistry energy exchange source term, M_s is the molecular weight and $\dot{\omega}_s$ is the mass production source term. $Q_{therm.}$ is the thermal energy exchange source term:

$$Q_{therm.} = \begin{bmatrix} 0 \\ 0 \\ 0 \\ 0 \\ \sum_{i}^{N_{mol}} \Omega_i^{VT} + \sum_{j}^{M_{species}} \Omega_j^{ET} \\ 0 \end{bmatrix} \tag{3.16}$$

Here, Ω^{VT} is the vibration-translation energy exchange source term, Ω^{ET} is the electron-translation energy exchange source term. $Q_{rad.}$ is the radiation source term:

$$Q_{rad.} = \begin{bmatrix} 0 \\ 0 \\ 0 \\ -\nabla.q_{rad} \\ -\nabla.q_{rad} \\ 0 \end{bmatrix} \tag{3.17}$$

3.2.2 Three-Dimensional Flows

In three dimensional Cartesian coordinates, the z-momentum equation is included and the Compressible Navier-Stokes equations are expressed in the same conservative form. The vector of the conservative quantities becomes:

$$U = \begin{bmatrix} \rho \\ \rho u_x \\ \rho u_y \\ \rho w_z \\ \rho E \\ \rho e_{ve} \\ \rho Y_s \end{bmatrix} \tag{3.18}$$

The inviscid component of the fluxes, $\overline{F}_i$, becomes:

$$\overline{F}_i = \begin{bmatrix} \rho u_x \\ \rho u_x^2 + p \\ \rho u_y u_x \\ \rho u_z u_x \\ \rho E u_x + p u_x \\ \rho e_{ve} u_x + p_e u_x \\ \rho Y_s u_x \end{bmatrix} \hat{i} + \begin{bmatrix} \rho u_y \\ \rho u_x u_y \\ \rho u_y^2 + p \\ \rho u_z u_y \\ \rho E u_y + p u_y \\ \rho e_{ve} u_y + p_e u_y \\ \rho Y_s u_y \end{bmatrix} \hat{j} + \begin{bmatrix} \rho u_z \\ \rho u_x u_z \\ \rho u_y u_z \\ \rho u_z^2 + p \\ \rho E u_z + p u_z \\ \rho e_{ve} u_z + p_e u_z \\ \rho Y_s u_z \end{bmatrix} \hat{k} \tag{3.19}$$

The viscous component of the fluxes, $\overline{F}_v$, is transformed into:

$$\overline{F}_v = \begin{bmatrix} 0 \\ \tau_{xx} \\ \tau_{yx} \\ \tau_{zx} \\ \tau_{xx} u_x + \tau_{yx} u_y + \tau_{zx} u_z + q_x \\ q_{x,ve} \\ J_{x,s} \end{bmatrix} \hat{i} + \begin{bmatrix} 0 \\ \tau_{xy} \\ \tau_{yy} \\ \tau_{zy} \\ \tau_{xy} u_x + \tau_{yy} u_y + \tau_{zy} u_z + q_y \\ q_{y,ve} \\ J_{y,s} \end{bmatrix} \hat{j} \tag{3.20}$$

$$+ \begin{bmatrix} 0 \\ \tau_{xz} \\ \tau_{yz} \\ \tau_{zz} \\ \tau_{xz} u_z + \tau_{yz} u_z + \tau_{zz} u_z + q_z \\ q_{z,ve} \\ J_{z,s} \end{bmatrix} \hat{k} \tag{3.21}$$

3.3 Numerical methods

3.3.1 Finite volume Method

The finite volume method is based on a discretization of the integral forms of partial differential equations, like the conservation equations, as stated in 3.9. This kind of space discretization is suitable for flow problems, because it ensures that the discretization is conservative locally and globally and it does not require a coordinate transformation to be applied to unstructured and irregular meshes.

The method is based on integral formulation of the conservative equations. In 2D, the conservation equations are applied to straight-edged quadrilateral cells. The boundaries of the control volumes are labeled North (N), East (E), South (S), West (W) and the computational node lies at the center of the cell. The basic structure of a two-dimensional

control volume scheme for a structured grid is presented in figure 3.1. In 3D, finite-volume cells are hexahedral with 6 quadrilateral surfaces interfacing the neighboring cells, called North (N), East (E), South (S), West (W), Top (T) and Bottom (B). Flux values are estimated at midpoints of the cell. The advantage of the fact that the computational nodes are assigned to the Control Volume center is that the nodal values represent the mean over the control volume at higher accuracy, since it is a second order discretization scheme (O^2).

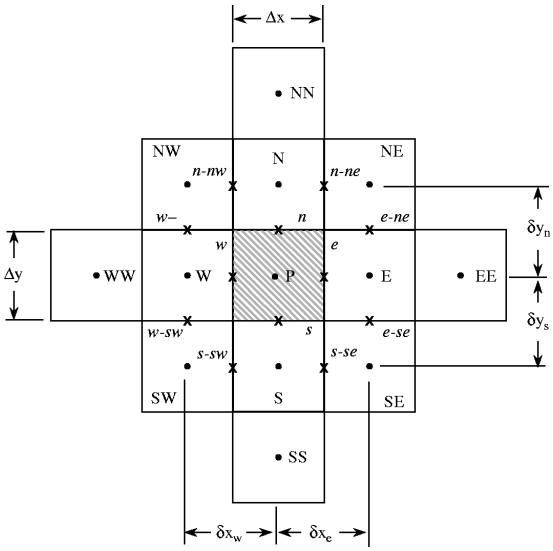

Figure 3.1: The control volume method scheme. For the present case it is assumed that $\delta_{y_n} = \delta_{y_s} = \Delta y/2$ and $\delta_{x_e} = \delta_{x_w} = \Delta x/2$

The net flux through the control volume is calculated as the sum of the integrals over the control volume surfaces (in 2D the surfaces are 4: N, S, W, E) and the integral conservation equation is approximated with the following algebraic expression:

$$\frac{dU}{dt} = -\frac{1}{V} \sum_{NESW} (\overline{F}_i - \overline{F}_v).\hat{n}dA + Q \tag{3.22}$$

, where U and Q represent cell-averages values.

3.3.2 Time stepping procedure

An operator-splitting approach (as described by Oran and Boris [7]) is used to perform the time-integration of this ordinary differential equation (3.22). The physical phenomena are handled in a decoupled manner, creating different time differentiations for the inviscid, viscous, chemical and thermal phenomena and the boundary conditions are imposed on the edges of the control volumes. Therefore, the time differentiation variable $\frac{dU}{dt}$ is decomposed into:

$$\left(\frac{dU}{dt}\right)_{inv.} = -\frac{1}{V}\sum_{NESW}(\overline{F}_i).\hat{n}dA + Q_{geom.} + Q_{rad.} \tag{3.23}$$

$$\left(\frac{dU}{dt}\right)_{visc.} = -\frac{1}{V}\sum_{NESW}(-\overline{F}_v).\hat{n}dA \tag{3.24}$$

$$\left(\frac{dU}{dt}\right)_{chem.} = Q_{chem.} \tag{3.25}$$

$$\left(\frac{dU}{dt}\right)_{therm.} = Q_{therm.} \tag{3.26}$$

3.3.3 Time discretization method

3.3.3.1 Explicit Method

As aforementioned, in the 2D solver, Eilmer3, the set of Ordinary Differential Equations (ODE) is obtained by an operator-splitting approach. Thus, each physical process can be handled by a more efficient integration scheme, which is useful for large chemical kinetic models (see [31] for the chemical model).

For a better understanding, $\overrightarrow{U}$ is the vector containing all the conserved quantities previously described. It is obvious that $\overrightarrow{U}$ is time and space-dependent and can be written as $\overrightarrow{U}(\overrightarrow{x}, t)$ for a one-dimensional problem. Once discretized in space and time, we end up with:
$U_i^n = U(x = x_i, t = t_n)$.
The next value of $\overrightarrow{U}$, can be computed via the second order upwind scheme as:
$U_i^{n+1} = f(U_i^n, U_{i-1}^n, U_{i-2}^n)$.
Therefore, the value of the considered conservative variable in a cell at the next time step (t_{n+1}) can only be computed if the past values (t_n) in the current and the two previous cells are known.

3.3.3.2 Implicit Methods

The method used for implicit time integration for the steady state problems encountered in this thesis, with the use of the 3D software, is the Lower-Upper Symmetric Gauss-Seidel (LU-SGS) method. The scheme is based on a lower-upper factorization and a symmetric Gauss-Seidel relaxation. The governing equations are discretized separately in space and in time. This ensures that the steady state solution will be independent of the time discretization procedure and therefore independent of the time step. The conservation equations are transformed into a diagonally dominant form, in order to meet the stability requirements of the relaxation method.

For the viscous flow cases, the contribution of the viscous terms is taken into account

incrementally in order to ensure the stability of the method. Two types of implicit operator are implemented for the treatment of the viscous terms: the scalar approach and the full-matrix approach. In the scalar approach, in order to maintain the diagonal form of the LU-SGS method and to save computation time, the viscous Jacobian is approximated by a scalar. In the full-matrix approach, the viscous terms are linearized assuming that the transport coefficients are locally constant. For more details the reader can refer to [17]

3.4 Initial Conditions

The numerical solution of any Conservation equation, such as the Navier-Stokes requires an initial solution in the flow-field, such that the algorithm is able to start iterating in time. The final solution is not dependent on the initial solution theoretically, because the numerical simulation should be able to converge with whichever initial solution. However, more appropriate initial conditions, which better replicate the final state of the flow-field, can accelerate the convergence of the algorithm. Keeping this in mind, the simulation sequence performed using *Eilmer3* is as follows:

- **Inviscid calculations**: For the inviscid calculations the inflow parameters are applied to the entire flow-field, i.e. the values of the conservation parameters of the inflow (pressure, temperature, density, velocity, species mass fractions) are filled in each cell of the domain.
- **Viscous calculations**: Since the inviscid calculation has already run and converged, it is highly recommended that the initial solution for the viscous calculations is taken from the final solution of the inviscid flow-field.
- **Viscous Radiation and Ablation coupled calculations**: In the same logic as the above case, for quicker convergence the initial solution for the ablation and radiation coupled simulations is taken equal to the final solution of the viscous simulations.

3.5 Boundary Conditions

The numerical solution of the Conservation equations (Navier-Stokes) requires the definition of some specific conditions on the boundaries of the domain, in order the algorithm to be able to start iterating through space. Depending on the gas dynamic model implemented each time, the boundary conditions are:

1. **Inflow**: The incoming flow is for every case filled with the free-stream values of the conservative variables, i.e. the far-field density, pressure and temperature for each trajectory point atmospheric height and the respective velocity of the vehicle and denoted as a supersonic inflow. It is noted that the Apollo 4 had an incident

angle of 25.5 deg, so there is not only a x-velocity component, but also a y-velocity component in the incoming flow.

2. **Outflow**: The outflow is defined in every case as an extrapolation of the flow parameters, i.e. a supersonic outflow where the ghost-cell flow properties are extrapolations of the adjacent interior cell properties.

3. **Symmetry**: In every case, the symmetry plane is recognized as an inviscid tangency (Slip Wall), where the normal velocity in the ghost cells is a reflection of the velocity in the interior cell.

4. **Solid Wall**: It is the boundary condition that is changed according to the flow modelling, as it governs the thermodynamics and chemistry of the simulation. The choice of the appropriate boundary condition lies on the following considerations:

   - Viscosity: If the flow-field is considered inviscid, the wall boundary is considered an inviscid tangency, i.e. an inviscid slip wall. If the flow-field is considered viscous, the wall cannot be considered a slip wall any more, as the fluid will have zero velocity relative to the boundary. Therefore, the boundary condition for this case focuses on the conservation of energy. Four types of boundary conditions are designated in the following section:
     Adiabatic wall: A no-slip wall where the wall temperature is the same as the cell-center temperature.
     Fixed temperature: A no-slip wall where the wall temperature is specified by the user as T_{wall} in degrees K.
     Energy balance: A variable temperature boundary condition that implies a dynamic evolution of the wall temperature governed by a surface energy balance at the wall interface. Along the normal direction to the wall interface, this energy balance is expressed as follows:

$$q_{in} + q_{out} = 0 \tag{3.27}$$

     The incident heat flux consists of a convection and a diffusion component, while the re-radiated heat-flux is calculated via a radiative equilibrium.

$$q_{in} = q_{conv} + q_{diff} + q_{rad} \tag{3.28}$$

$$q_{out} = \epsilon\sigma T_w^4 \tag{3.29}$$

     ,where σ is the Boltzmann constant and ϵ is the emissivity. Thus, equation 3.27 concludes in:

$$T_w = \left(\frac{-q_{conv} - q_{diff} - q_{rad}}{\epsilon\sigma} \right)^{1/4} \tag{3.30}$$

Besides, as the heat flux depends on the wall temperature, the radiative equilibrium wall temperature is evaluated via an iterative procedure.
Ablating boundary condition: A boundary condition that models the behavior of the ablative heat shield material via inducing a pyrolysis gas mass flow at the wall. It also introduces in the flow-field the 9 carbon-hydrogen species, apart from the 11 atmospheric ones, completing the 20 species chemical model by Park, discussed in 3.6.1. For further details on the specific boundary condition the reader is referred to [19] and [24].

- Wall catalycity:
  Non-catalytic wall: An extreme condition, making the wall completely insensitive to kinetics. This boundary condition only applies the chemical composition in the cell closer to the wall. Thus, there is no production or depletion on the wall interface.
  Super-catalytic wall: Another extreme condition, which considers the wall to be an infinitely efficient catalyst as it applies the free-stream chemical composition to the wall interface.
  The ideal catalycity boundary condition should be modeled in between those limits: it should consider the reaction kinetics due to the solid surface.

3.6 Thermochemistry

The gas dynamic equations of the previous sections are completed by a set of relations between the various thermodynamic properties of the gas mixture. To close the equation set the pressure must be related to the state vector. This relation depends on the model used to describe the thermodynamic properties of the gas. In high-temperature hypersonic flows with strong shocks, the the variation of the specific heats with temperature and/or the effect of the dissociation of air have a large influence on the flow parameters and the heat flux to the wall. In such conditions the flow cannot be modeled as an ideal gas mix, as perfectly elastic collisions and caloric perfect behavior cannot be applied. There are three main types of gas models that better estimate the gas state in hypersonic conditions and used for the present calculations [43]:

- Equilibrium gas: This chemical state models the gas mixture as a fixed-composition gas mix, which is assumed to be both in thermal and chemical equilibrium at local thermodynamic conditions. It can be assumed that the gas is in equilibrium, when the characteristic time for readjustment by the collisions between particles is much smaller than the characteristic time of the fluid flow. This means that the energy of the collisions is not high enough to lead to dissociation, ionization or even to storage of energy in the internal degrees of freedom of the particles. Because both the translational and rotational and the vibrational energy modes characteristic times

are smaller than that of chemistry, a flow in chemical equilibrium is always assumed to be in translational-rotational and vibrational equilibrium.

For flows in chemical equilibrium, the governing equations are similar to those for a caloric perfect gas except for the equation of state, $p = p(\rho, T)$.

- Non-Equilibrium gas: As aforementioned, collisions between particles in which the collision energy is so high that a particle dissociates or ionizes lead to dissociation or ionization of the gas respectively. If the characteristic time for the readjustment by collisions is of the same order of magnitude as the characteristic time of the flow, the flow is in non-equilibrium. The thermally perfect gas (or just chemical non-equilibrium) is the gas state, in which the gas components have all a perfect (collisional) behavior but each component has all internal energy modes excited to an equilibrium described by a single temperature.

  For flows in chemical non-equilibrium, the governing equations are supplemented with equations describing the mass conservation of the chemical species in the reacting mixture. As a result, the continuity equation has to be solved for each chemical species.

- Thermal Non-Equilibrium gas:

  As aforementioned, the collisions between free stream particles and molecules of the dense shock layer excite the rotational, vibrational and electronic modes of the molecules, and give rise to a non-equilibrium between the temperatures and energies corresponding to these modes [14]. Generally, translational and rotational energy modes require a few collisions to equilibrate, so they are usually considered in equilibrium even for Hypersonic flow conditions, for the sake of time-saving. On the other hand, chemical dissociation and vibrational excitation require more collisions to reach their equilibrium state and non-equilibrium effects may be important for hypersonic flow conditions, especially at high altitudes. With the assumption of thermal non-equilibrium, a multi-temperature model is applied, in which every temperature dictates a different energy mode [32]. This way, the total internal energy of any species i is formed by the contributions of translational, rotational, vibrational and electronic energies. The same applies to the thermodynamic and transport properties of the gas mixture [13].

  $e = e_t + e_r + e_v + e_e$

  Molecules are presented with all energy modes, while only translational and electronic modes are associated with atoms and free electrons.

  Modern non-equilibrium models ideally associate a modal energy e_{ms} depending on temperature T_{ms} for mode m for each species s. The internal energy of the gas mixture of species is hence given by:

$$e = \sum_s y_s \sum_m e_{ms}(T_{ms}) \tag{3.31}$$

,where y_s is the mass fraction of each species s in the gas mixture.

The model used in the present work is a commonly-used thermal non-equilibrium, two-temperature model, developed by Park [31]. In the specific model, the system is described by two temperatures: T_{tr}, which stands for the translation-rotation energy mode of the heavy particles and T_{ve}, which represents the distribution of vibrational, electronic excitation and electron translation energies.

In the two-temperature model the total energy can be split into kinetic energy, translation-rotation energy and vibration-electron-electronic energy:

$E = e_{tr} + e_{ve} + \frac{1}{2}\vec{u}\vec{u}$

The internal energy e for N_{modes} thermal modes is given by the sum of the specific energy of each mode:

$e = \sum_m^{N_{modes}} e_m$

For the two-temperature model, the above equation is transformed into: $e = e_{tr}+e_{ve}$. This means that every energy and heat-flux is defined as the sum of the two thermal modes. For example, the conduction heat-flux term is defined as:

$$\vec{q_{cond}} = \vec{q_{cond,tr}} + \vec{q_{cond,ve}} = -k_{tr}\nabla T_{tr} - k_{ve}\nabla T_{ve} \tag{3.32}$$

3.6.1 Chemical modelling

Park's chemical model developed in 2000 [31], used among simpler models in the present work (e.g. 7 species model of atmospheric air gas mixture for the 3D cases), is an atmospheric chemical model, including ablative materials emerging from PICA-like materials. As can be seen in Table ??, it considers 20 species divided into three categories:

1. *Air species*: species that are present in the Earth's atmosphere.

2. *Ablative species*: species that are emerging from the ablative wall as ablative gases.

3. *Boundary layer species*: species that are formed as the ablative species are broken down as they pass through the boundary layer and the post-shock layer.

Table 3.2: Chemical reactions considered in Park's 2001 model

Reactions	M	A	$T_a[K]$	n	Reactions	M	A	$T_a[K]$	n
Dissociation reactions									
$N_2 + M \rightleftharpoons N + N + M$	All	7.0^{21}	113200	−1.6	$O_2 + M \rightleftharpoons O + O + M$	All	2.0^{21}	59360	−1.5
	C	3.0^{22}	113200	−1.6		C	1.0^{22}	59360	−1.5
	O	3.0^{22}	113200	−1.6		O	1.0^{22}	59360	−1.5
	N	3.0^{22}	113200	−1.6		N	1.0^{22}	59360	−1.5
	H	3.0^{22}	113200	−1.6		H	1.0^{22}	59360	−1.5
	e^-	3.0^{24}	113200	−1.6	$H_2 + M \rightleftharpoons H + H + M$	All	2.2^{14}	48300	0.0
$C_2 + M \rightleftharpoons C + C + M$	All	3.7^{14}	69900	0.0		H_2	5.5^{14}	48300	0.0
$CN + M \rightleftharpoons C + N + M$	All	2.5^{14}	87740	0.0					
Neutral exchange reactions									
$N_2 + O \rightleftharpoons NO + N$	–	5.7^{12}	42938	0.42	$CN + O \rightleftharpoons NO + C$	–	1.6^{13}	14600	0.10
$NO + O \rightleftharpoons O_2 + N$	–	8.4^{12}	19400	0.0	$CN + C \rightleftharpoons C_2 + N$	–	5.0^{13}	13000	0.0
$CO + C \rightleftharpoons C_2 + O$	–	2.0^{17}	58000	−1.0	$CO + C_2 \rightleftharpoons C_3 + O$	–	1.0^{12}	41200	0.0
$CO + O \rightleftharpoons O_2 + C$	–	3.9^{13}	69200	−0.18	$C_3 + N \rightleftharpoons CN + C_2$	–	1.0^{12}	34200	0.0
$CO + N \rightleftharpoons CN + O$	–	1.0^{14}	38600	0.0	$C_3 + C \rightleftharpoons C_2 + C_2$	–	1.0^{12}	16400	0.0
$N_2 + C \rightleftharpoons CN + N$	–	1.1^{14}	23200	−0.11	$C_2H + H \rightleftharpoons C_2 + H_2$	–	1.0^{12}	16770	0.0
Electron impact ionization reactions									
$O + e^- \rightleftharpoons O^+ + e^- + e^-$	–	3.9^{33}	158500	−3.78	$C + e^- \rightleftharpoons C^+ + e^- + e^-$	–	3.7^{31}	130720	−3.00
$N + e^- \rightleftharpoons N^+ + e^- + e^-$	–	2.5^{34}	168200	−3.82	$H + e^- \rightleftharpoons H^+ + e^- + e^-$	–	2.2^{30}	157800	−2.80
Associative ionization reactions									
$N + O \rightleftharpoons NO^+ + e^-$	–	5.3^{12}	31900	0.0	$N + N \rightleftharpoons {N_2}^+ + e^-$	–	4.4^{7}	67500	1.5

,where A is the frequency factor in $\left[m^3/mole\right]^{N-1} s^{-1}$, T_a is the temperature that corresponds to the activation energy E_a in K and n is the temperature exponent of the Arrhenius equation, that describes the temperature dependency of the reaction rates of each reaction:

$$k = Aexp\left[-\left(\frac{E_a}{RT}\right)^n\right] \tag{3.33}$$

It should be noted that some species as HCN, CNO, NH and O_2^+ are missing from the model, even though their effects are particularly important in reentry conditions. Their concentrations are small, while O_2^+ presents no significant impact on chemical reactions and radiation.

3.6.2 Chemical Kinetics

For an accurate characterization of the shock layer in atmospheric reentry, a good knowledge of the species mass fractions consumed and produced by chemical reactions in the shock layer is required. Therefore, apart from the species identified, the reactions and the kinetics of the species should also be investigated. The 20 species identified in Park's model form a 24-reaction scheme (5 dissociation reactions, 12 exchange reactions, 4 electron impact ionization reactions, and 2 associative ionization reactions). All those reactions are governed by the chemical kinetics theory which deals with the reaction rates corresponding

to the speed of reaction. These reaction rates must be computed in order the evolution of the gases mixture composition and thus the chemical behavior of the flow field to be described accurately.

An usual set of n chemical reactions involving Ns species needs to take into account a parameter r to distinguish the different reaction. It can be described by:

$$\sum_{i=1}^{N_s} \nu_{i,r}[x_i] \rightleftharpoons \sum_{i=1}^{N_s} \nu''_{i,r}[x_i] \tag{3.34}$$

Where x_i is the species mole fraction and $\nu_{i,r}$ and $\nu''_{i,r}$ are the stoechiometric coefficient. Equation 3.34 can be split into two individual relations: one for the reaction going from left to right and the other for that going from right to left. Let us denote by $k_{f,r}$ the forward reaction rate coefficient and $k_{b,r}$ the backward one. Taking into account this transformation and summing over all reactions we end up with the Law of Mass action expressed in terms of mass production for a particular species α:

$$\dot{\omega_s} = M_\alpha \sum_{r=1}^{n} (\nu_{\alpha,r} - \nu''_{\alpha,r}).\{k_{f,r} \prod_{i=1}^{N_s} [x_i]^{\nu_{i,r}} - k_{b,r} \prod_{i=1}^{N_s} [x_i]^{\nu''_{i,r}}\} \tag{3.35}$$

In equation 3.35 the forward and backward reaction rate coefficients can be expressed using the equilibrium reaction rate constant k_c:

$$k_{c,r} = \frac{k_{f,r}}{k_{b,r}} = A.T^{\eta} \exp\left(\frac{-E_A}{RT}\right) \tag{3.36}$$

k_c follows the extended Arrhenius law where E_A is the activation energy , η is the temperature exponent and R is the gas constant. In Park's model, the Arrhenius law was defined as:

$$k(T) = C\ T^n\ exp(-\frac{T_a}{T}), \tag{3.37}$$

, where C, n and T_a (activation temperature) are presented in **??** for the Park 20 species chemical model.

3.6.3 Transport properties

The choice of the chemistry model influences the transport properties required to solve the Navier-Stokes equations, such as the gas mixture's viscosity and thermal conductivity. For the purposes of this section, the modelling of the fluid viscosity is further discussed. In a given gas mixture, the collisions between the different particles (atoms, molecules, ions, electrons) create an induced momentum transfer. The amount of momentum transfer depends on the electromagnetic forces and, thus, on the shape and size of the particles involved. The kinetic gas theory proposes the particles to be modeled as hard-spheres and that is how Maxwell defined the following proportionality relation for the viscosity [40]:

$$\eta_i \propto \frac{(M_i T)^{1/2}}{\sigma_i^2} \tag{3.38}$$

where M, T and σ denote respectively the molecular mass, absolute temperature in K and hard-sphere diameter in $\mathring{A}$.
When the collisions between particles are taken into account, the model of hard-spheres is no longer suitable; so a correction factor is required in equation 3.38. This factor denoted by Ω_V is called collision integral [40]:

$$\eta_i = 26.69 \frac{(M_i T)^{1/2}}{\sigma_i^2 \Omega_V}. \tag{3.39}$$

In a similar way, thermal conductivity and mass diffusion can be expressed as below [41]:
Conductivity:

$$\lambda_i = \frac{15}{4}\left(\frac{\eta_i * R_0}{M_i}\right)\left(\frac{4}{15}\frac{C_{pi} M_i}{R_0} + \frac{1}{3}\right) \tag{3.40}$$

Mass diffusivity:

$$D_{ij} = \frac{0.0188 T^{3/4}\sqrt{(M_i + M_j)/M_i M_j}}{p\sigma_{ij}^2 \Omega_{D_{ij}}} \tag{3.41}$$

Conclusively, microscopic interactions between particles govern the transport properties of the fluid, which are defined as linear combinations of the collision integrals.

Therefore, collision integrals are fundamental inputs for modern computational tools, such as `Eilmer3`. Moreover, as there is a collision integral for each pair of chemical species, a N_s-species model requires $1/2 \cdot N_s * (N_s - 1)$ computations. So the present work needs 190 collision integrals as it is based on Park's 20-species chemistry model.In `Eilmer3`, collision integrals are entered as 4 coefficients of a 3-order polynomial interpolation in $\log T$ as:

$$\log(\pi\Omega) = A \log^3 T + B \log^2 T + C \log T + D. \tag{3.42}$$

3.7 Heat transfer modelling

3.7.1 Convection Modelling

The heat flux created on the surface of the solid because of the surrounding heating environment is transferred inwards the capsule body with means of conduction. Convective heat transfer is modeled with the heat diffusion equation as follows:

$$\vec{q}_{conv} = \vec{q}_{cond} + \vec{q}_{dif} = -\kappa \nabla T + \sum_s h_s \vec{J}_s + \int_v \vec{I}_v dv \tag{3.43}$$

In the fluid domain heat is generated by the isentropic compression created by the shock,the friction of the fluid on the solid surface, dissociation of the chemical species and by heat radiation of the heated fluid due to the intensity of the flow velocity of an atmospheric

entry. In presence of a moving fluid heat is transported mainly by convective heating. It is usually described by Newton's law of cooling:

$$\dot{q_{conv}} = hA(T_\infty - T_s) \tag{3.44}$$

,where T_s is the temperature on the body surface, T_∞ is the free-stream temperature and h is the heat transfer coefficient, which is dependent on the type of transfer media, gas or liquid, the flow properties, such as velocity and viscosity and other flow and temperature dependent properties.
Convection is usually used to describe the combined effects of heat conduction within the fluid with diffusion mechanisms. Therefore, it is crucial to model diffusion in such a way, so that the results obtained are accurate.

Molecular Diffusion

For the case of an ablating boundary surface, the mass balance equation must be taken into consideration for the flux of chemical species entering or leaving the ablating surface. With the assumption that no solid material is removed in a condensed phase, the mass balance of species i at the surface is written as:

$$\rho D_{ij} \left.\frac{\partial Y_i}{\partial n}\right|_w + \dot{m}_{c,i} + \dot{m}_{g,i} = (\rho_i v_n)_w + \sum_{r}^{N_r eactions} \dot{\omega}_{i,r} \tag{3.45}$$

, where D_{ij} is the binary diffusion coefficient, for two interacting components, Y_i the mass fraction of species i, ρ the density, v the velocity and $\dot{m}$ the mass blowing for either gas or char for the g and c subscripts respectively. The term $\dot{\omega}_{i,r}$ is the creation or destruction of chemical species i during surface reaction r.

The diffusive species mass flux at the wall:

$$J_{i_w} = \rho D_{ij} \left.\frac{\partial Y_i}{\partial n}\right|_w \tag{3.46}$$

expresses the relative motion of chemical species with respect to the motion of their moving center of mass. D_i is the effective binary diffusion coefficient of each species i into the gas mixture, i.e. the mass diffusivity. The higher the diffusivity of one substance relative to another, the faster they diffuse into each other.

Thermal diffusion

Thermal diffusion affects the diffusion mass flux if there is a temperature gradient in the flow-field. The diffusion mass flux exerted from thermal diffusion is equal to: $J_T = nD_T \frac{1}{T} \nabla T$, where D_T is the thermal diffusion coefficient and n is the total number of

molecules per unit volume. The induced diffusive heat flux is calculated:

$$q_{gas,diff} = -\rho \sum_i D_T h_i \left(\frac{\partial c_i}{\partial y} \right)_w \tag{3.47}$$

All the calculations presented in this work have been solved for two diffusion models:

- Constant Lewis Number: The Lewis number in reacting flows, i.e. flows where there is simultaneous heat and mass transfer by convection, is a dimensionless number defined as the ratio of thermal diffusivity to mass diffusivity: $Le = \frac{\alpha}{D}$, where α is the thermal diffusivity and D the mass diffusivity. The thermal diffusivity is defined as: $\alpha = \frac{\kappa}{\rho C_p}$, where κ is the thermal conductivity, ρ is the density and C_p is the specific heat capacity and it relates the ability of a material to conduct thermal energy to its ability to store thermal energy.

  A simplified way to obtain effective individual species diffusion coefficients consists in deriving them from an assumed constant Lewis number. This simplification is based on the concept of individual species Lewis number changing little through the reactive area of the hypersonic flow-field. However, such a simplification can hardly be considered accurate, as the Lewis number is highly dependent on the temperature of the mixture, which radically changes during reentry conditions.

- Ambipolar Diffusion in Two-Temperature Multicomponent Plasmas (Ramshaw-Chang Model)

  This approach [35] calculates the diffusional mass fluxes of the individual components of species relative to the mass-averaged velocity of the fluid are calculated after extracting the diffusion coefficients (binary molecular and thermal) from relations containing collision integrals, such as the following:

  $$D_{ij} = \frac{3k_B^2 T_i T_j}{16 p \mu_{ij} \Omega_{ij}^{(1)}(1, T_{ij})}$$

  ,where k_B is Boltzmann's constant, $\mu_{ij} = m_i m_j/(m_i + m_j)$ is the reduced mass for the pair (i,j), m_i is the mass of a single particle of species i, $\Omega_{ij}^{(1)}(1, T_{ij})$ is a standard collisional integral and $T_{ij} = \frac{m_i T_j + m_j T_i}{m_i + m_j}$.

3.7.2 Radiation Transport Modelling

Processes such as dissociation and ionization make the gas particles radiate electromagnetic energy in the flow (radiative heating) and also transfer energy to the surface when they collide with it (convective heating). The radiating gas can be either absorptive and gain energy or transparent and emit energy in the flow-field.

Radiation is a non-local phenomenon, i.e. electromagnetic energy emitted at one location in a plasma field may be absorbed at any location within a line-of-sight of the origin. A first order approximation of radiation transport is to assume an optically thin or thick medium, representing the cases where 100% and 0% local re-absorption occurs. For atmospheric entry shock layers, however, the actual local re-absorption is generally somewhere between these two limiting cases. The tangent-slab model makes various simplifications to the integro-differential equations governing radiative transport such that they can be more easily solved.

However, the tangent-slab model has been shown to not accurately predict radiative heat-flux due to shock layer curvature [8]. The accurate solution of the radiation transport equations requires the discretization of the computational domain via ray-tracing. Such an approach has been implemented by considering the radiation field as a discrete quantity in Monte-Carlo models [16].

3.7.2.1 Radiation Source Term

The radiation source term in the Navier-Stokes equations is the negative divergence of the local radiative heat flux vector $-\nabla.\overrightarrow{q_{rad}}$. It can be related to the radiative intensity which is defined by Anderson [1] as: *radiative energy (dE) transferred in the r direction crossing the unit area (dA) orthogonal to r, per unit frequency (dν), per unit time (dt), per unit solid angle (dω)* as can be seen in 3.48. For better understanding, the definition of radiative intensity is schematically presented in 3.3.

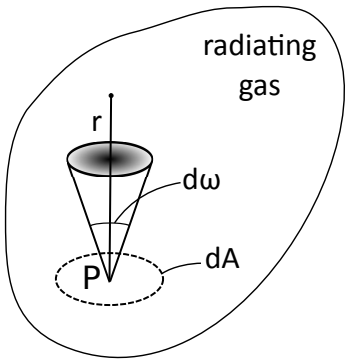

Figure 3.2: The schematic representation of the definition of Radiative intensity

$$I_\nu = \lim_{dAd\omega d\nu dt \to 0} \left[\frac{dE_\mu}{dAd\omega d\nu dt} \right] \tag{3.48}$$

Thus the radiation source term is written:

$$-\nabla.\overrightarrow{q_{rad}} = -\nabla. \int_0^\infty \overrightarrow{I_\nu} d\nu \tag{3.49}$$

For applications to computational grids it is convenient to express equation 3.50 as the

difference between local emission and absorption:

$$-\nabla.\overrightarrow{q_{rad}} = \int_0^\infty \int_{4\pi} \kappa_\nu I_\nu d\omega d\nu - 4\pi \int_0^\infty j_\nu d\nu \tag{3.50}$$

Where κ_ν is the spectral absorption coefficient and j_ν is the spectral emission coefficient.

3.7.3 Flow-field Radiation coupling

A useful parameter for estimating the degree of radiation flow-field coupling is the Goulard number:

$$\Gamma = \frac{2\dot{q}_{rad}}{\frac{1}{2}\rho_\infty u_\infty^3} \tag{3.51}$$

, where $\dot{q}_{rad}$ is the radiative heat flux incident at the stagnation point, ρ_∞ the free-stream density and u_∞ the free-stream velocity. The Goulard number is a measure of the conversion of energy flux in the free-stream to radiative energy flux incident on the vehicle. When the Goulard number becomes large ($\Gamma > 0.01$) radiation flow-field coupling should be taken into consideration due to significant levels of radiative flux through the shock layer.

3.7.3.1 Transport models

A variety of models are implemented in the Flow-field Solver for the radiative source term to be calculated:

1. **Optically-thin model**

   The optically-thin model neglects re-absorption, transforming 3.50 into:

   $-\nabla.\overrightarrow{q_{rad}} = -4\pi \int_0^\infty j_v dv.$

   For the radiating shock layers of hypersonic reentry cases, the majority of the radiative emission is located in the vacuum-ultraviolet spectral region where re-absorption is significant. The optically-thin model will therefore substantially overestimate the radiative divergence, and is not an appropriate model for this work.

2. **Tangent-slab model**

   The tangent-slab model allows the effect of re-absorption to be modeled while avoiding a complete directional integration of the local intensity field. A one-dimensional variation of properties is considered along each line-of-sight normal to the vehicle surface. Computationally, a line of cells is used to represent the normal line-of-sight as demonstrated in figure 3.3. This is a good approximation to the body normal direction for the shock-aligned grids (such as the ones built for blunt reentry bodies). If a single column of blocks is used to define the computational domain between the

inflow and vehicle surface boundaries, the tangent-slab model is realisable, as all the information required for the calculation is contained in the local block.

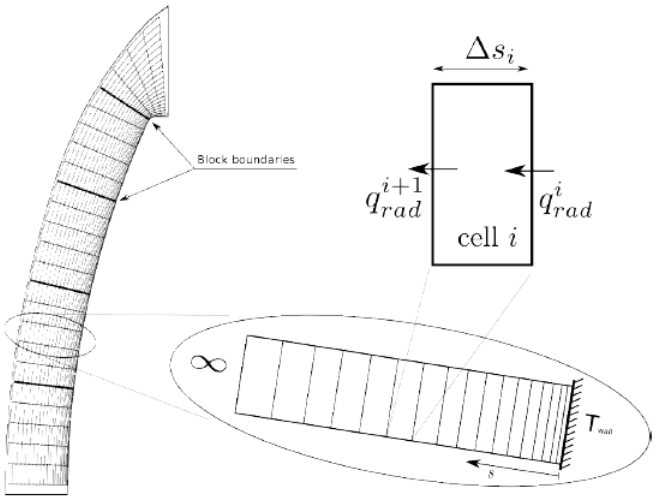

Figure 3.3: Schematic of tangent-slab calculation domain along lines of cells on a multi-block grid

Given that the infinite-slab arrangement will result in zero net radiative flux in the transverse directions, the definition of the radiative divergence for slab i reduces to:

$$-(\nabla \vec{q}_{rad})_i = -\left(\frac{\partial q_{rad}}{\partial s}\right)_i = \frac{-(q_rad^{(i+1)} - q_rad^{(i)})}{\Delta s_i}$$

,where $q_{rad}^{(i)}$ is the radiative flux at the i_{th} cell interface (i.e. preceding the cell from right-to-left) and Δs_i is the width of the cell in the (approximately) body normal direction. The solution for the radiative flux in a gaseous medium between two parallel, infinite-slabs is a function of the spectral optical thickness τ_v. If the computational domain is a collection of N_{slabs} isothermal slabs with the spectral range discretized into N_v frequency intervals, the radiative flux at interface i can be expressed as:

$$q_{rad}^{(i)} = \sum_{k=1}^{N_v} 2\pi I_{v_k,wall} E_3\left(\tau_{v_k}^{(i)}\right) + 2\pi \sum_{j=1}^{N_{slabs}} S_{v_k}^{(j)} \left[E_3\left(\left|\tau_{v_k}^{(i)} - \tau_{v_k}^{(j)}\right|\right) - E_3\left(\left|\tau_{v_k}^{(i)} - \tau_{v_k}^{(j-1)}\right|\right)\right] \Delta v_k$$

,where $S_{v_k}^{(j)}$ is the source function for the $i_t h$ isothermal cell at v_k frequency, $I_{v_{k,wall}}$ is the intensity emitted by the wall and the optical thickness $\tau_{v_k}^{(i)}$ is calculated as:

$$\tau_{v_k}^{(i)} = \sum_{l=1}^{i} \kappa_{v_k}^{(l)} \Delta s_l$$

The E_n term is the $n_t h$ order exponential integral with form:

$E_n(x) = \int_1^\infty \omega^{-n} exp(-\omega x) d\omega$

The E3 curve fit that is implemented in the tangent-slab model is a semi-empirical formula:

$E_3 = 0.0929e^{-4.08x} + 0.4071e^{-1.33x}$

The intensity emitted by the wall with emissivity ϵ_{wall} is calculated:

$I_{v,wall} = 2\pi\epsilon_{wall}\sigma T_{wall}^4$

,where T_{wall} is the black-body wall temperature.

3. **Ray-Tracing Models**

The basic principle of ray-tracing based models is the direct numerical integration of the radiant energy field over direction and space via the generation of a radiation sub-grid mapped over the CFD grid. The radiation sub-grid consists of rays distributed iso-directionally from each point of interest in the flow-field, with the flow state and radiation spectra defined at distributed points along each ray. An example of a radiation sub-grid on a simple axisymmetric CFD grid is illustrated in figure 3.4.

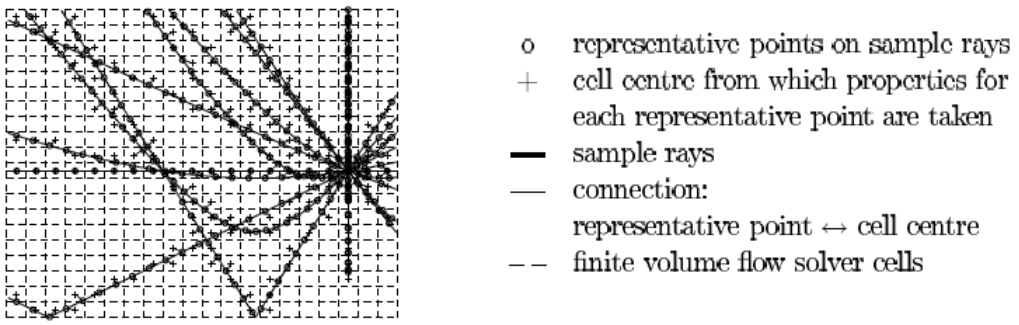

Figure 3.4: Example of a radiation sub-grid on a simple 2D axisymmetric grid

The ray-tracing model developed and implemented in the flow-field solver Eilmer3 uses the radiative sub-grid to transport packets of radiant energy through the computational domain. This is similar to a photon Monte-Carlo method in that radiation is treated as a discrete quantity rather than a continuous field. However the ray-distribution is kept uniform and energy attenuation is modeled in a statistical fashion.

Mathematical formulation

The total radiative divergence for a finite-volume cell is calculated as the difference between the total emissive power $E_{ems.}$ and absorptive power $E_{abs.}$ divided by the cell volume V:

$$-\nabla.\overrightarrow{q_{rad}} = \frac{-\left(E_{ems.} - E_{abs.}\right)}{V} \tag{3.52}$$

,where:

$$E_{ems.} = \int_V \int_0^{4\pi} \int_{v_{min}}^{v_{max}} j_v dv d\omega dV = \sum_r^{N_{ems.rays}} \sum_n^{N_v} E_{r,n} \tag{3.53}$$

$$E_{abs.} = \sum_r^{N_{abs.rays}} \sum_n^{N_v} (-\Delta E_{r,n}) \tag{3.54}$$

,where $N_{abs.rays}$ is the total number of ray segments traversing the current cell, $N_{ems.rays}$ is the total number of rays emitted by this cell and the frequency domain has been divided into N_n intervals between n_{min} and n_{max}. $E_{r,n}$ is the power carried by a photon packet n with frequency interval Δ_{vn} from ray r with solid angle Δ_r:

$$E_{r,n} = j_v \Delta v_n \Delta_r V \tag{3.55}$$

The radiative power lost by a photon packet n while traversing from point s_i to s_f along a ray is calculated from:

$$-\Delta E_{r,n} = -\left(1 - e^{-\kappa_{v_n}(s)\Delta s}\right) E_{r,n}(s_i) \tag{3.56}$$

, where $\Delta s = s_f - s_i$. Similarly, the radiative heat flux incident on any wall element q_rad is calculated as the sum of the remaining energy from all incident rays $N_{inc.rays}$ divided by the wall element area A:

$$q_{rad} = \frac{E_{abs.}}{A} = \frac{\sum_r^{N_{inc.rays}} \sum_n^{N_v} E_{r,n}}{A} \tag{3.57}$$

Ray-tracing and radiation sub-grid

The ray-tracing method for planar and axisymmetric grids of quadrilateral cells is based on the creation of a radiation sub-grid and the connection of this to the main flow-field grid. The radiation sub-grid coordinates of a point at distance L along a ray with elevation and azimuth angles ϕ and $theta$, originating from position x_0, y_0 are defined as:

$$\acute{x}{=}x_0 + Lcos(\phi)cos(\theta) \tag{3.58}$$
$$\acute{y}{=}y_0 + Lsin(\phi) \tag{3.59}$$
$$\acute{z}{=}Lcos(\phi)sin(\theta) \tag{3.60}$$
$$\tag{3.61}$$

The corresponding CFD grid coordinates are then calculated from the following transformation (in 2D application):

$$x{=}\acute{x} \tag{3.62}$$
$$y{=}\sqrt{\acute{y}^2 + \acute{z}^2} \tag{3.63}$$

This transformation has the effect of reflecting rays intersecting the symmetry axis at $y = 0$, as required. For planar geometries the radiation sub-grid is formed in the xy plane as the CFD domain is symmetrical along the z axis.

The core of the ray-tracing method is a cell searching algorithm that allows the radiation sub-grid to be mapped onto the CFD grid, such as the one shown in Figure 3.5

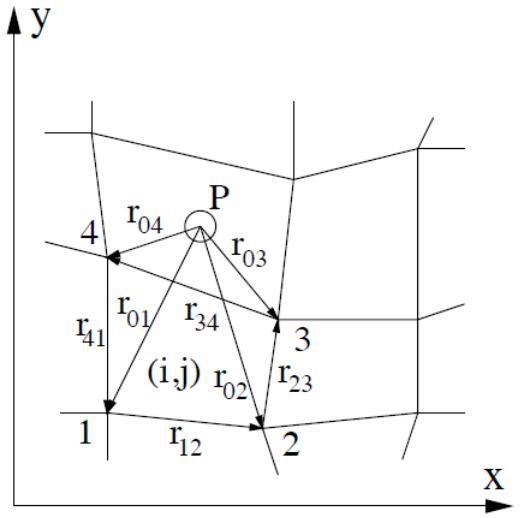

Figure 3.5: Example of mapping of the radiation sub-grid onto the CFD grid

Part II

Numerical Simulations in 2D

Chapter 4

Simulations in 2D

This chapter presents the overall procedure to set up and run a simulation on `Eilmer3`*, the two-dimensional solver, developed by the University of Queensland, Australia, and the main results of the present calculations.*

4.1 Eilmer3: The code

For the two-dimensional simulations of the Coupled Radiative Flow-field around the Apollo Command Module the code *Eilmer3* was used for pre-processing and running, as well as post-processing the cases, along with a visualization software, *Paraview*. *Eilmer3* is a transient compressible flow simulation code, developed by the Center for Hypersonics of the University of Queensland, Australia and is based on the finite volumes discretization method. The code is written in C++ and Python.

The code can solve transient compressible flow problems in two or three dimensions on a generated block-structured grid, which defines the flow domain. Various features of hypersonic flows, such as ablation models, thermal radiation and chemical models, are still being developed and updated, making the code particularly useful for atmospheric entries.

The flow solver implemented in Eilmer3 is one of explicit type, which means that the values of conservative variables at the next time step $(n+1)$ can be computed directly via the discretization scheme, using the already known solution at the current time step n. This is usually what triggers stability issues, that need to be controlled by the Courant number in the CFL number (C in $CFL = C \times \frac{Dt}{Dx}$. For this reason, Eilmer3 and generally explicit solvers generally require specific and small time steps for finer grids.

4.1.1 Simulation procedure

Eilmer3 is practically an integrated collection of programs that prepare, run and post-process the simulation. Running a simulation in *Eilmer3* is essentially done in three steps:

1. Pre-processing:
   The program *e3prep.py* is responsible for creating the grid and the initial solution for the simulation, using as an input file a python script, which contains all the information needed: gas model and flow states, the blocking and grid construction, boundary and initial conditions for the simulation, and some general and control parameters. After this step, a .svg sketch of the blocking, the initial solution files and other files required for the simulation, such as the time integration files, will be created.

2. Simulation:
   The execution of the simulation is performed by either the program *e3shared.exe* or the program *e3mpi.exe*, depending on whether the simulation is done on one or multiple processors (in parallel). The files created by the simulation are the flow data and the heat flux files at subsequent times.
   Moreover, the program *e3rad.py* can be used to calculate the radiative heat fluxes around the body, by solving the heat transport equations, using an existent converged solution.

3. Post-Processing:
   The final step is done with the program *e3post.py*, whose purpose is to make the results of the simulation human-readable, by reformatting the flow solution data or the heat flux files to produce files suitable for a data viewing program, such as Paraview or GNU-Plot. Moreover, it is used to run the tangent slab calculations for radiations, as the tangent slab model doesn't solve the heat transport equations. Finally, .dat files are created during post-processing containing information on flow properties or heat-fluxes along certain streamlines of the flow (such as the stagnation line or a line on the body surface).

4.2 Results Discussion

During the present work simulations were run in order to validate the computational efficiency and the accuracy of results of the Eilmer3 solver. The simulations were performed for three specific trajectory points (see Table 2.1 of the actual flight path of the Apollo capsule. The results will be compared with empirical correlations and actual flight data.

The Apollo 4 geometry was modified in order to reduce the computational expense. Indeed, the capsule was modeled in two dimensions and the computational domain was reduced to the fore-body, whereas the wake region was ignored. As the radiative heat flux at the

stagnation point of a blunt body is governed primarily by the shock standoff, it becomes possible to define a 2D equivalent sphere. From Schlieren studies carried out by Ried et al (ref.Ried et al.), Park (ref.Parkstagnation) chose a sphere of 2.85m radius, which gave the same shock standoff as seen on the Apollo 4 geometry at 25.5 deg angle of attack. In this study, the same equivalent sphere radius is used in order to be able to verify the results from Eilmer3 with Park's results. Indeed, the final geometry implemented in the 2D simulations is the one depicted in figure 4.1; it consists of the equivalent sphere of Apollo 4, while the case is built as axisymmetric. The boundary conditions are the same for each case for the inflow, outflow and symmetry boundaries, whereas it changes on the wall surface, according to the case simulated each time. More specifically, the east boundary of the domain changes from a slip-wall for an inviscid calculation to an energy-balance surface for a viscous calculation and to an ablative boundary condition for an ablation calculation.

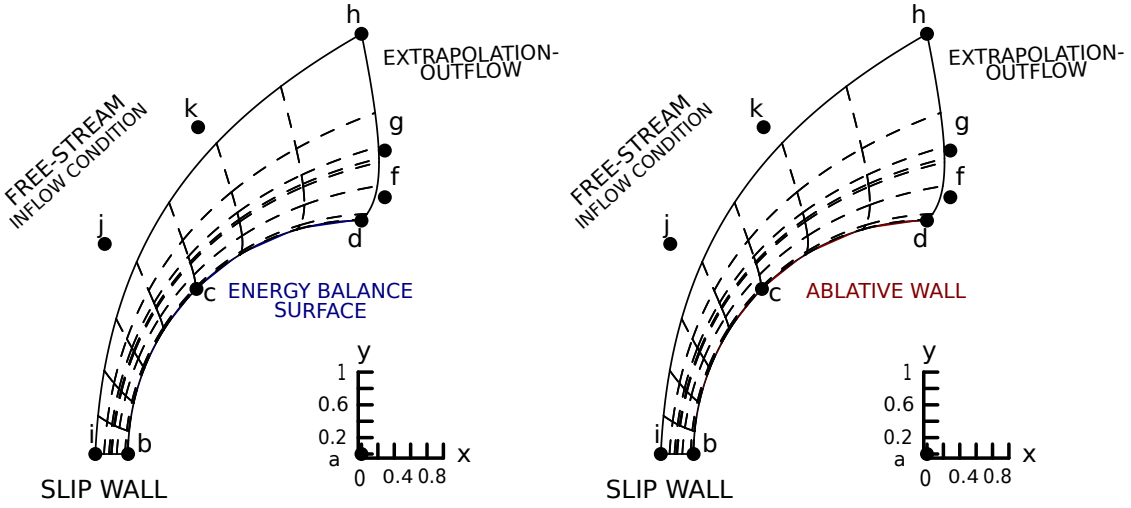

(a) Viscous Flow **(b)** Viscous flow, ablation included

Figure 4.1: Blocking of the domain of the Apollo 4 fore-body for a viscous case, with and without ablation

4.2.1 Pre-processing

The viscous simulations are initialized with the converged inviscid case, which is set up with a coarser mesh, preventing the solution to diverge when inserting the viscous effects. Once the flow is well established from the inviscid solution, the viscous effect is added incrementally. The transport properties (e.g. viscosity) are incremented at each time step for stability reasons as stated in the relation: $\mu_i^{n+1} = \mu_i^n \times F_{inc}$, where F_{inc} is the incremental factor, which for the present calculations was set to $1 \cdot 10^{-5}$.

The generated mesh for the inviscid and viscous cases for the 2^{nd} trajectory point, which is also the peak radiative heating point, is presented in figure 4.2. It is worth mentioning that for the viscous cases the mesh was not only refined at the boundary layer region,

but also on the edge of the shock layer, in order to capture the generated shock wave (see figure 4.2c). The mesh used for the inviscid case was selected to be an 8×8-multi-block mesh of 100×100 cells, after investigating the solution's independence of the mesh. On the other hand, the viscous mesh was an 8×8-multi-block mesh of 160×160 cells. The mesh is divided into 64-blocks for computational efficiency. This extreme values of divided blocks are implemented due to the size of the domain. Both the selected meshes showed good convergence results, as the energy and mass residuals dropped to the order of 10^{-5}.

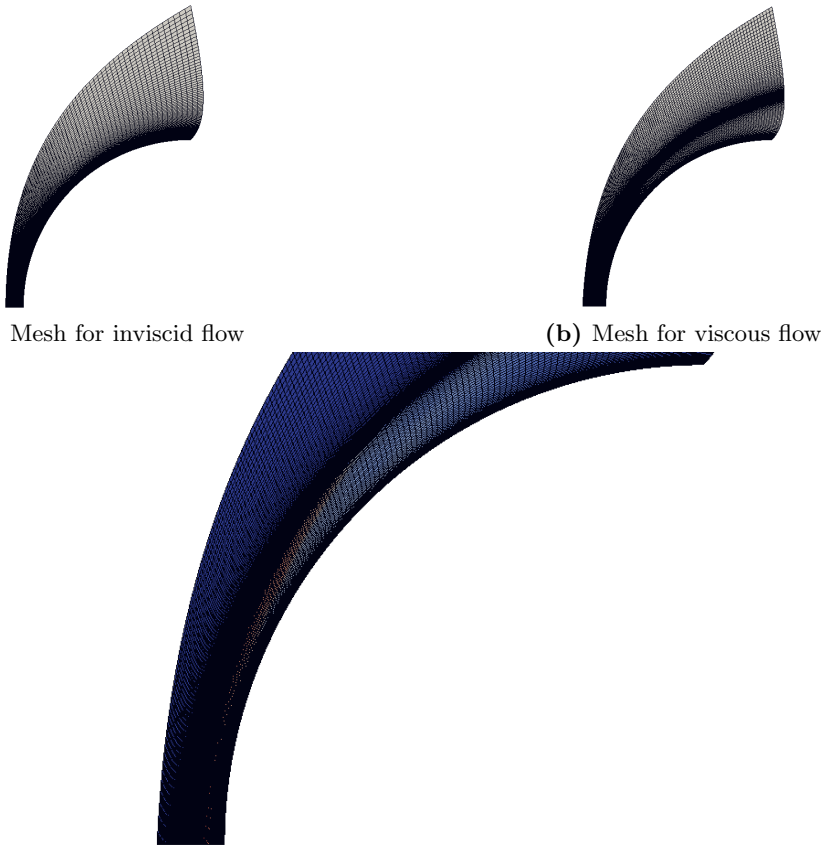

(a) Mesh for inviscid flow

(b) Mesh for viscous flow

(c) Detail of the mesh for a viscous flow: Pressure field illustrated, capture of the shock

Figure 4.2: Meshing of the domain for an inviscid and a viscous flow calculation

4.2.2 Comparative results for one trajectory point

The following section discusses the results for the peak radiative heating point of the Apollo 4 trajectory, 2nd of the three presented points, named T2, in table 2.1. Comparisons are made for inviscid versus viscous flow models, with or without an ablative boundary condition implemented. Furthermore, a comparison of two diffusion models, the Constant Lewis Number and the Ramshaw-Chang ones, is performed.

4.2.2.1 Flow-field results

Figures 4.3 and 4.4 show the velocity and the temperature profiles respectivelly along the stagnation line for the inviscid and viscous cases, with and without ablation and with the two diffusion models. The results are considered valid. At approximately a distance of 15 cm from the stagnation point, the u-velocity values suddenly reduce to values close to zero, while the temperature values (both translational-rotational and vibrational-electronic ones) suddenly increase and then drop again. This indicates the existence of a strong shock wave across the fluid flow. For both the inviscid and viscous flow models the shock standoff distance is calculated equal to 14.9 cm from the wall surface, whereas for the ablation cases the shock stand-off distance is shifted further away from the wall surface, at 16.1 cm. Moreover, for the ablation cases with the Constant Lewis Number diffusion model the shack standoff distance is larger than the one calculated with the Ramshaw-Chang diffusion model, whereas, the translational-rotational peak temperature for the same cases is also higher, shown in figure 4.4. Finally, from the v-velocity graphs, the change of the flow direction in the shock layer is also evident.

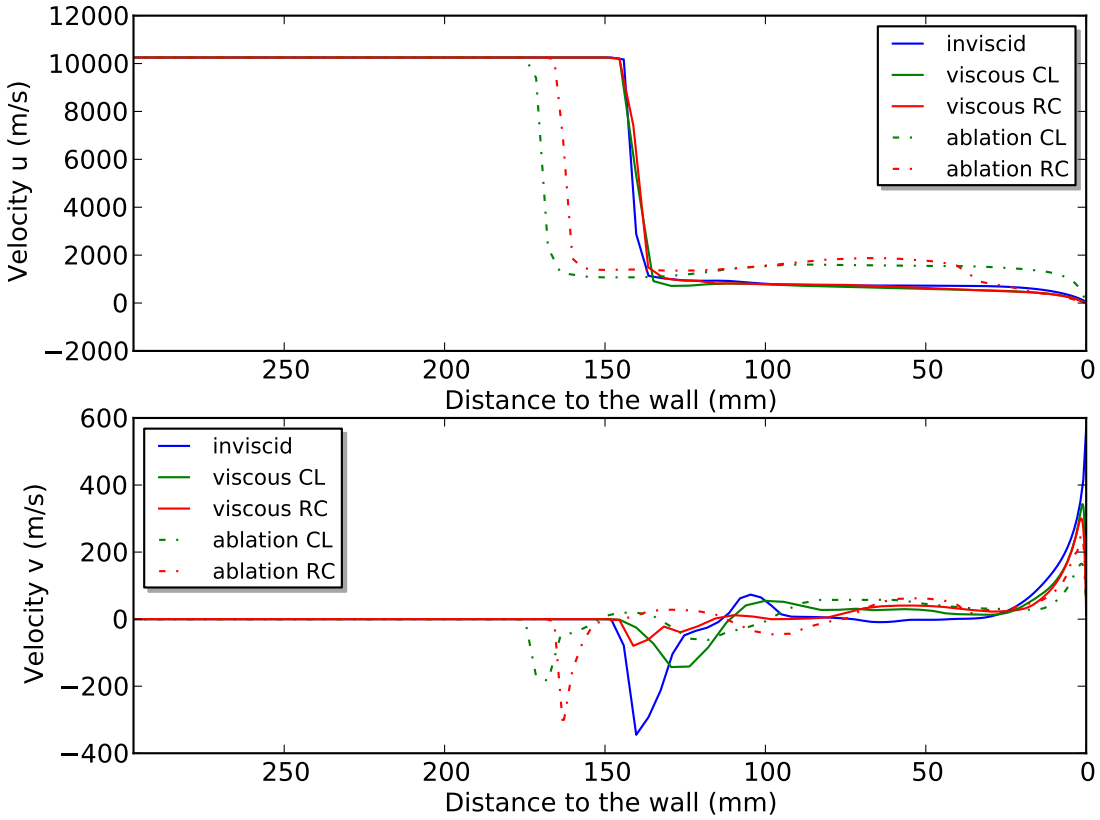

Figure 4.3: Velocity profile along the stagnation line, T2, investigation of ablation effects and diffusion model

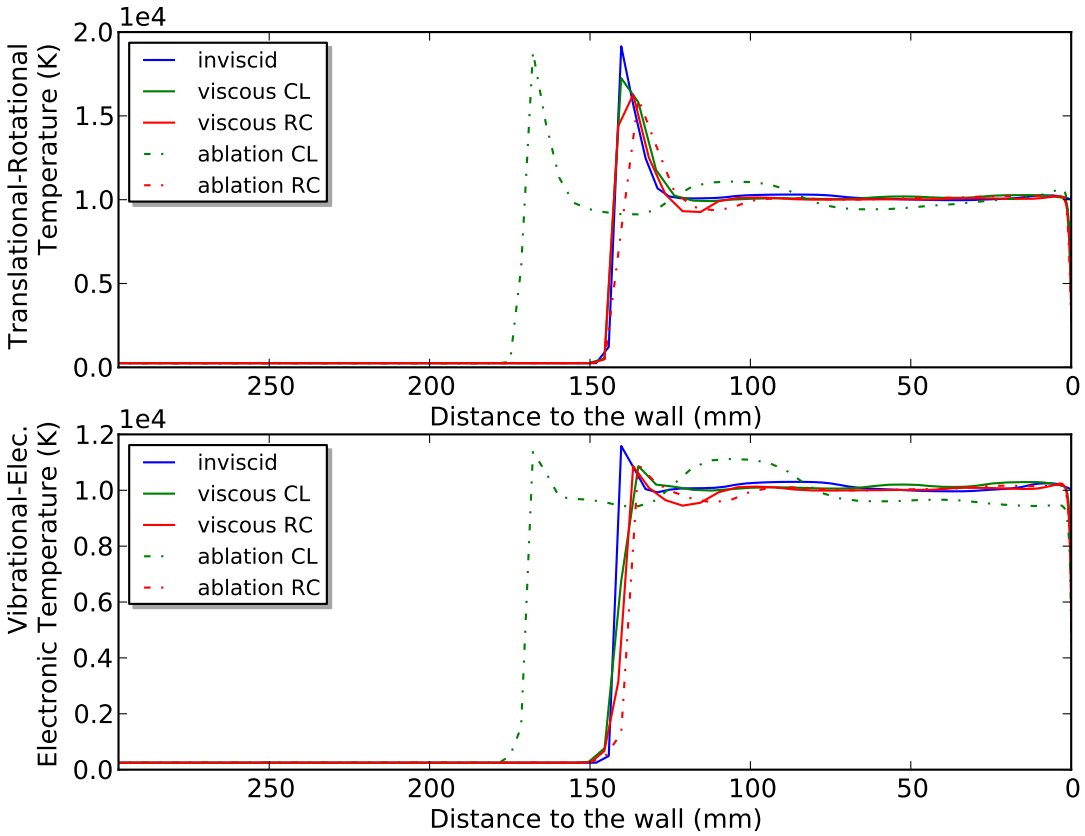

Figure 4.4: Temperature profile along the stagnation line, T2, investigation of ablation effects and diffusion model

The species mass fractions' profiles in the shock layer are presented in figure 4.5 for the ablation case. The graphs are illustrated in a logarithmic scale. The calculation was performed with the 22-species gas model, presented in section 3.6.1. As ablative species have been injected in the gas mixture the composition of the gas mixture of air and ablative species has been highly modified. In the region close to the wall the main ablative species is carbon and its mass fraction on the wall is more than ten times higher than the following highest mass fractions. The ablative mass fractions never become significant compared to the air species mass fractions. It should also be noticed that the ablative species are present in an extremely small region close to the wall surface ($\leq 14mm$), compared with the shock-standoff distance ($\approx 15cm$).

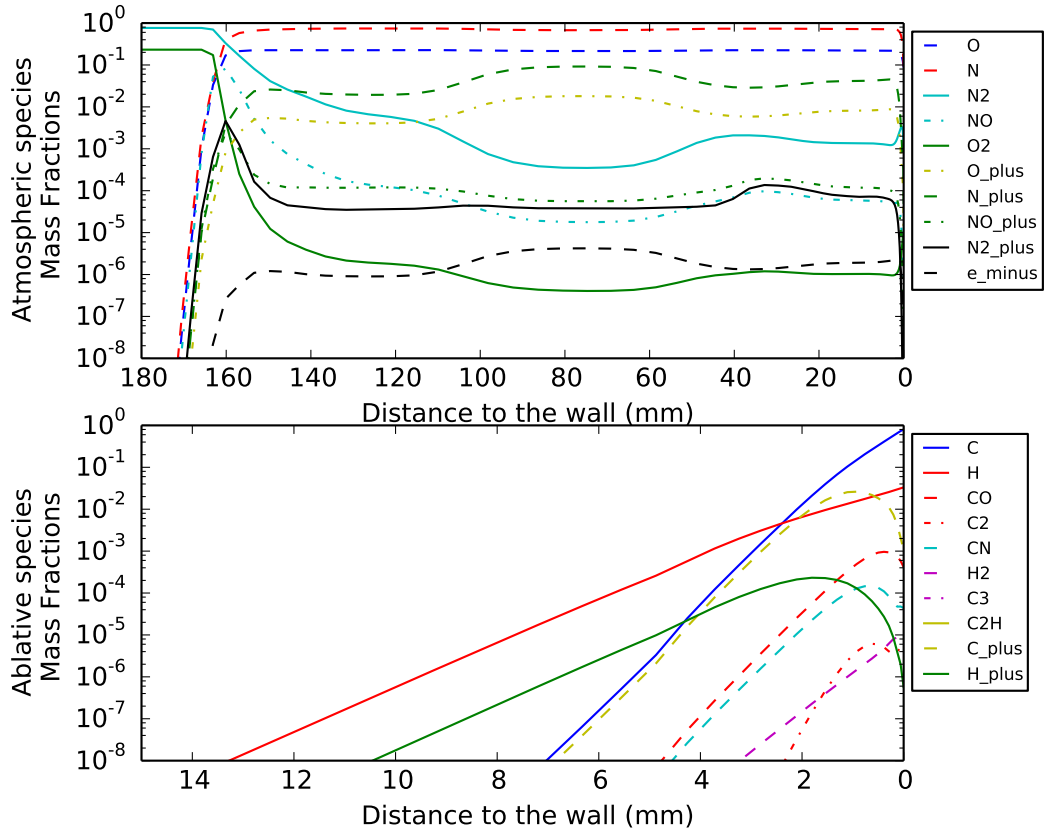

Figure 4.5: Species mass fractions along the stagnation streamline, T2, ablative viscous flow

4.2.2.2 Heat flux calculations

For each case, viscous with or without the ablative boundary condition taken into consideration, the heat fluxes were calculated during the simulations. In the following section the calculated heat fluxes (conductive and convective) are compared between the cases with or without ablation. Two diffusion models were used and the results they gave are also compared in this section.

Figure 4.6 illustrates the conductive and diffusive heat flux participation in the heat flux field along the capsule's wall for a viscous case without ablation. As it is easily extracted, the diffusive heat flux can be considered insignificant in this case.

Figure 4.7 illustrates the convective heat flux on the wall of the Apollo 4 capsule, as calculated with the use of the Ramshaw-Chang and the Constant Lewis Number Diffusion Models. It is observed that the Constant Lewis Number diffusion model calculates a conductive heat flux almost twice the value of the the one calculated with the Ramshaw-Chang model. As it will be shown in section 4.2.4.1, the values of convective heating for

large nose radii are particularly small. Thus, the Ramshaw-Chang Model is considered more appropriate for this simulation case.

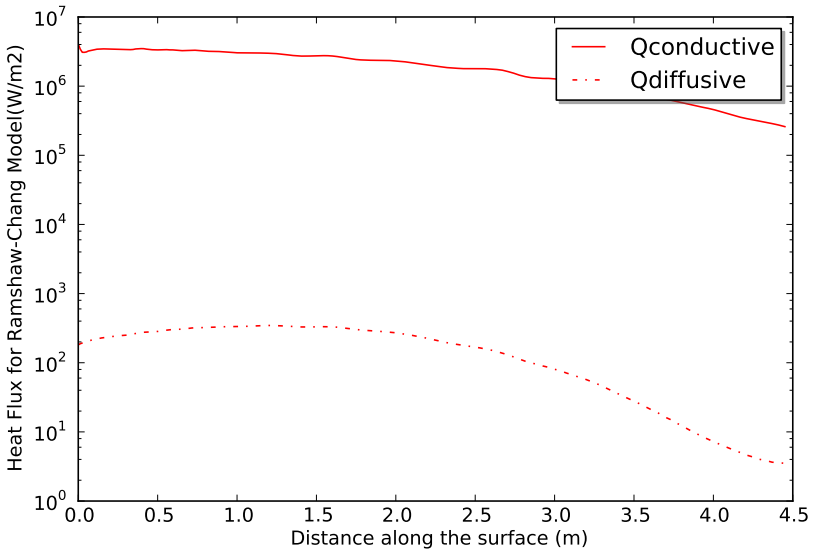

Figure 4.6: Conductive and Diffusive heat flux for the viscous non-ablation case, second trajectory point

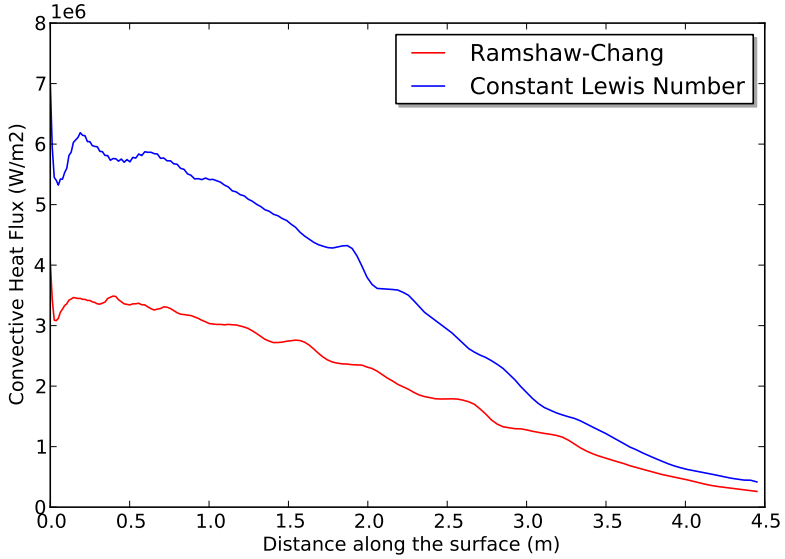

Figure 4.7: Convective heat flux for the viscous non-ablation case, second trajectory point. Comparison of diffusion models

4.2.2.3 Radiation Calculations

The viscous converged simulation is used as a starting point for the Radiation calculations. Radiation calculations are also performed for the ablation cases, considering the 10 more ablative species. Calculations were run assuming the QSS (=Quasi Steady State) non-equilibrium electronic level population model, whereas two different radiation transport models were investigated: the tangent slab and the Monte-Carlo ray-tracing method (with 16 rays). It is worth noticing that the e3rad.exe executable file that is used for the Ray-Tracing Approach is not calculating the spectra in the case, just the radiative heat flux in the flow-field. In order for spectral data to be calculated for these cases, the solution should be post-processed with the tangent slab approximation. The radiation library used for the radiation calculations is the photaura library implemented in Eilmer3.

The spectral wavelength range was considered between $60 \leq \lambda \leq 4000nm$, as most of the existent data used the spectral range of (0.06-4 μm). The radiators considered are the following:

$$C,\ O,\ N,\ H,\ CO,\ C_2,\ N_2,\ CN,\ NO,\ O_2,\ H_2,\ O^+,\ H^+,\ N^+,\ NO^+,\ {N_2}^+,\ e^-$$

The radiators considered in the QSS non-equilibrium electronic level population model are the following:

$$C,\ O,\ H,\ CO,\ C_2,\ O_2$$

It is noticed that the species containing N were proved to be unstable for the QSS population model and therefore were not taken into consideration.

Figure 4.8 illustrates the spectral flux and the integrated flux calculated with the tangent slab radiation transport method for the second trajectory point, which is also the peak radiative point. It is noticed that above 50% of the total integrated flux is reached in the wavelength range between (0.06-0.2 μm), which is designated as the VUV (=Vacuum-Ultra-Violet) range. However, the spectral lines above 700 nm have a valid contribution in the total spectra of the case. Figure 4.9 is illustrating the calculated spectra with the tangent slab model, divided into specific wavelength regions, in order the spectral lines that mostly contribute to the total spectra of the case to be identified. Figure 4.11 illustrates the results obtained by the cases with ablation. It is obvious that in the VUV region the spectra is not much differentiated. However, as illustrated in figure 4.11, the effect of the ablative species is more evident in the visible region of the wavelength range, as the whole spectra graph in this region appears to be more energetic. It should be noted that the lines expected from the ablative species are most commonly expected in the visible region of the spectra.

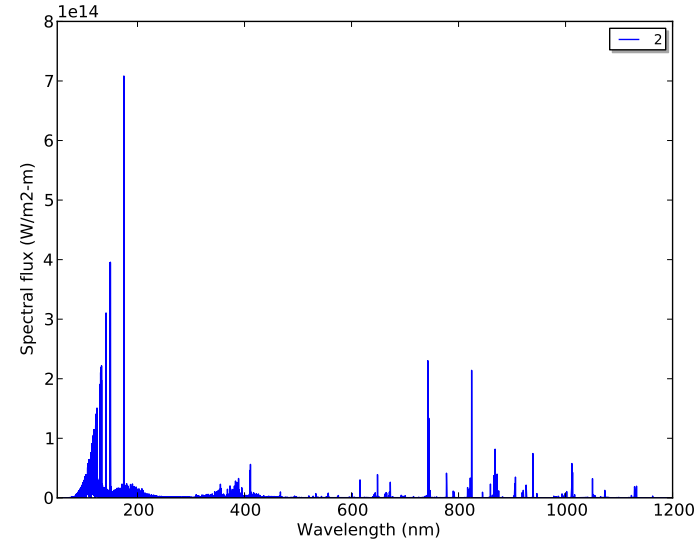

(a) Spectra in wavelength range 50-4000 nm

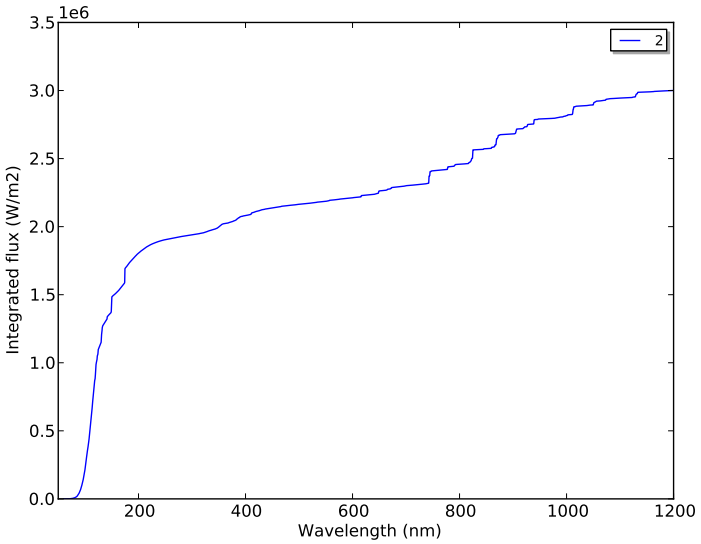

(b) Integrated flux in wavelength range 50-4000 nm

Figure 4.8: Spectral and integrated heat flux, peak radiative heating point, tangent slab radiation transport model

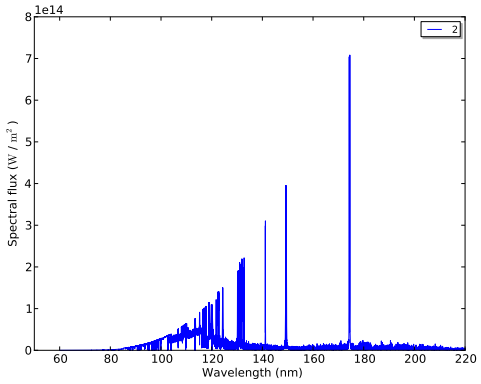

(a) Spectra in wavelength range 50-220 nm

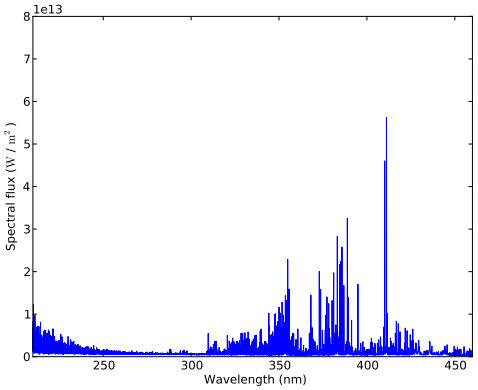

(b) Spectra in wavelength range 210-460 nm

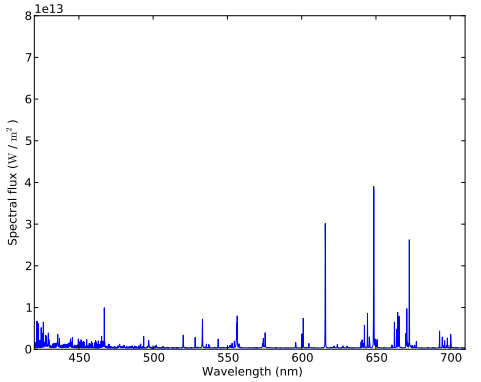

(c) Spectra in wavelength range 420-710 nm

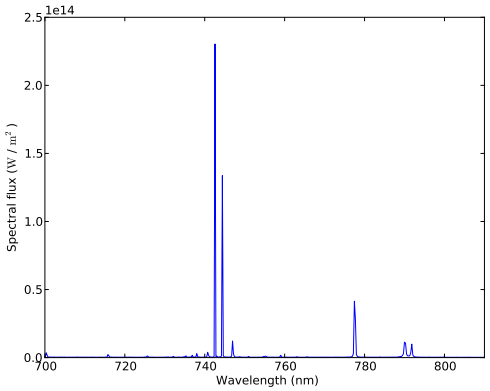

(d) Spectra in wavelength range 700-810 nm

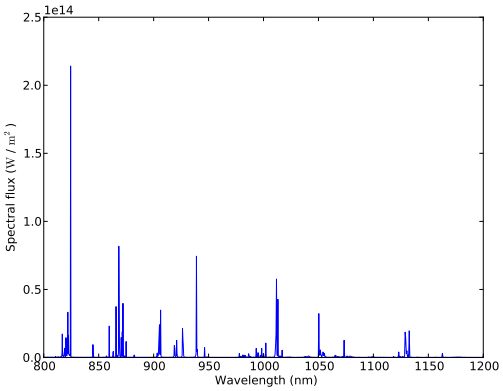

(e) Spectra in wavelength range 800-1200 nm

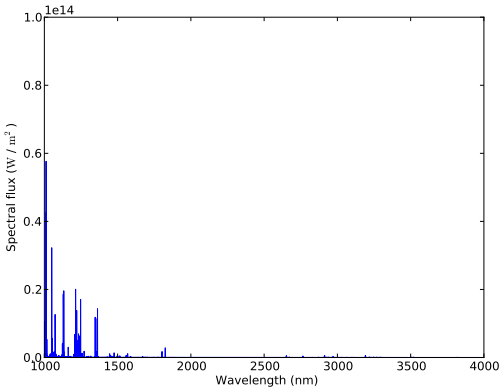

(f) Spectra in wavelength range 1000-4000 nm

Figure 4.9: Spectral heat flux, peak radiative heating point, tangent slab radiation transport model. Divided spectra into specific important regions of the wavelength range

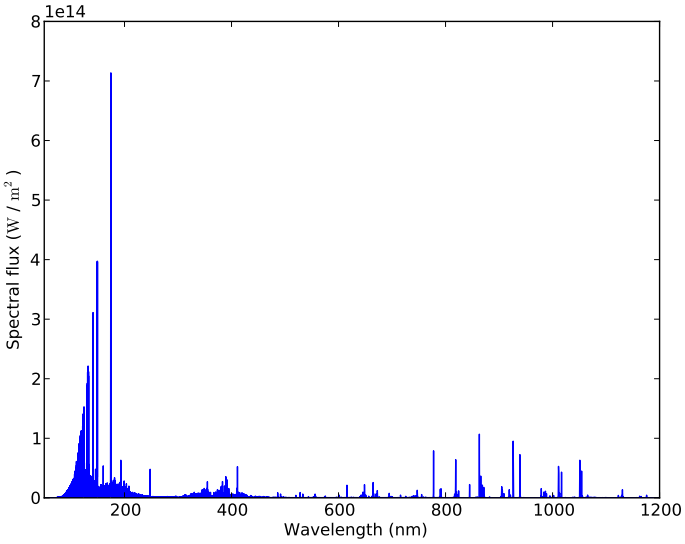

(a) Spectra in wavelength range 50-1200 nm

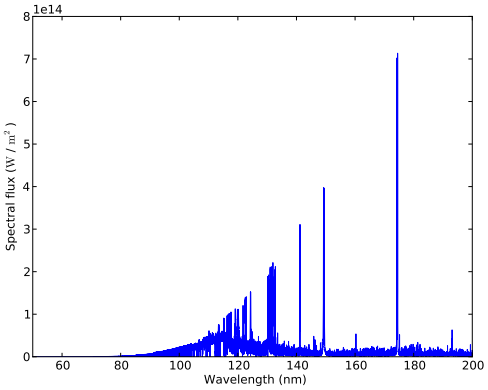

(b) Spectra in wavelength range 50-200 nm

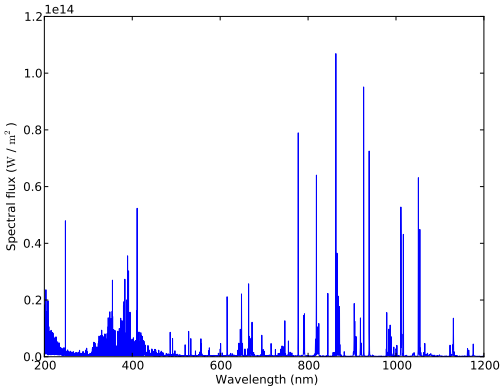

(c) Spectra in wavelength range 200-1200 nm

Figure 4.10: Spectral heat flux, peak radiative heating point, tangent slab radiation transport model, ablation included

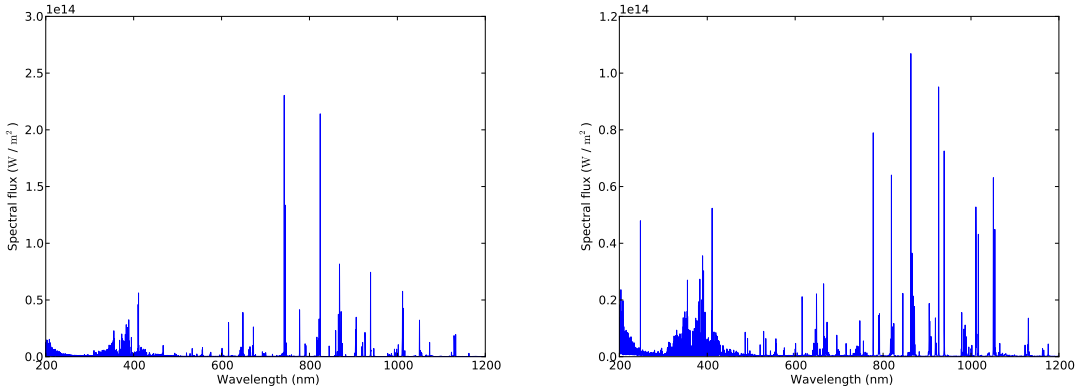

(a) Viscous case, no ablation **(b)** Viscous case with ablation

Figure 4.11: Spectral heat flux in wavelength range 200-1200 nm, peak radiative heating point, comparison of ablation and no-ablation cases

Figure 4.12 illustrates the radiative divergence, $\nabla.q_{rad}$, along the stagnation streamline. As shown, the radiative divergence is highly perturbed across the shock-wave line, at 14.5 cm. It drops to $-3 \cdot 10^8\ W/m^3$ for the wavelength range (0.2-4 mm) and to $-0.6 \cdot 10^8\ W/m^3$ for the wavelength range (0.06-4 μm), which means re-absorption in the shock layer is stronger if the VUV-range is excluded from the calculations.

Figure 4.13 presents the radiative heat flux profile along the wall surface of the capsule for the viscous no-ablation case, calculated with the Constant Lewis Number Diffusion Model and for the wavelength range between 0.05-1.2 μm. In comparison with the also illustrated conductive heat flux on the surface, the radiative heat flux is approximately $60 - 80\%$ of the overall heating for the case of the Apollo 4 vehicle. Both the calculations with the Discrete Transfer and Tangent Slab radiation transport models agree on the results of the heat flux on the surface. It is also noticed that the radiative heat flux calculated with the Monte-Carlo method is unstable for the case of this wavelength range. As it will be shown in the next section, the results for the Monte Carlo calculations for the wavelength range between 200-1200 nm are more stable and acceptable.

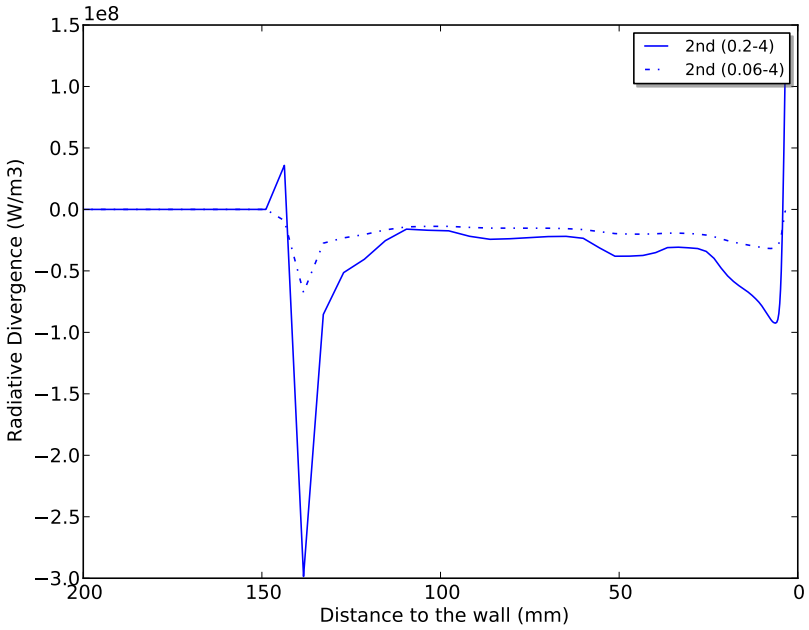

Figure 4.12: Radiative divergence along stagnation streamline, Peak radiative heating point, Tangent slab radiation transport model

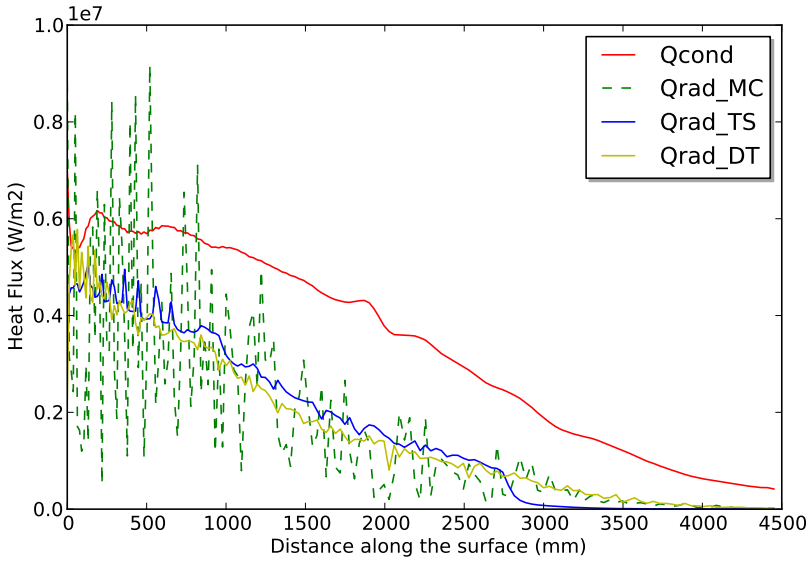

Figure 4.13: Conductive and Radiative heat fluxes for wavelength range (0.05-1.2 μm) along wall surface, Peak radiative heating point

4.2.3 Trajectory points comparison

The following section discusses the comparative results for three points of the Apollo 4 trajectory in table 2.1. Comparisons are made for viscous cases with and without ablation.

Figure 4.14 illustrates the velocity profiles for the two first trajectory points for the case of viscous flow, with and without ablation effects. The results show that the 1st trajectory point is less affected by the ablation condition. From the temperature profiles along the stagnation streamline (figure 4.15, it is observed that the translational-rotational temperature value for the ablation cases is slightly higher than the one for the viscous-no-ablation cases.

The convective heat flux along the wall surface of the capsule for the three trajectory points is compared in figure 4.17, using the Constant Lewis Number Diffusion model and not taking into consideration the ablation effects. For this diffusion model, the second point is the peak heating point of the trajectory. Figure 4.16 shows the calculated conductive heat fluxes along the wall surface of the capsule, utilizing the Ramshaw-Chang diffusion model. The conductive heat flux is smaller in the case of an ablative wall boundary than it is for a non-ablative wall for each trajectory point. Therefore, the reduction of the conductive heat flux on the wall validates the use of the ablative boundary condition, as the ablative species injected from the TPS shift the shock wave further away from the capsule's solid wall. Moreover, with the use of the Ramshaw-Chang diffusion model, the 3rd trajectory point is considered the peak heating point.

The radiative heat flux along the surface is calculated with the use of both the Monte-Carlo radiation photon transport model (a ray-tracing method) and the tangent slab model for the three trajectory points. The results presented in figure 4.18 are the ones obtained from the radiation calculations in the wavelength range between 200-1200 nm with bot the radiation transport models. For both cases the conductive heat flux presented is the one calculated with the Ramshaw-Chang diffusion model for the second trajectory point. It is observed that the radiative heat fluxes calculated with the Monte-Carlo method are greater than the ones calculated with the tangent slab model, therefore, the tangent slab model underestimates a little the heat flux calculations. Furthermore, the radiative heat flux along the wall surface that is calculated with the Monte-Carlo photon method is not so smoothly distributed. That is pointed out as a code-issue, and is currently investigated in order to be resolved. in any case, the calculated

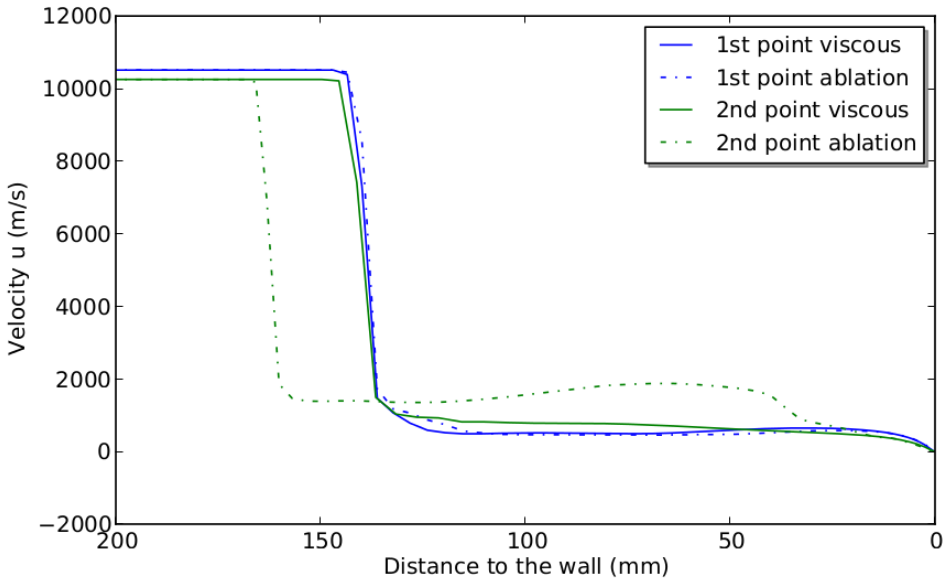

Figure 4.14: Velocity profiles for the two trajectory points, viscous flow with and without ablation

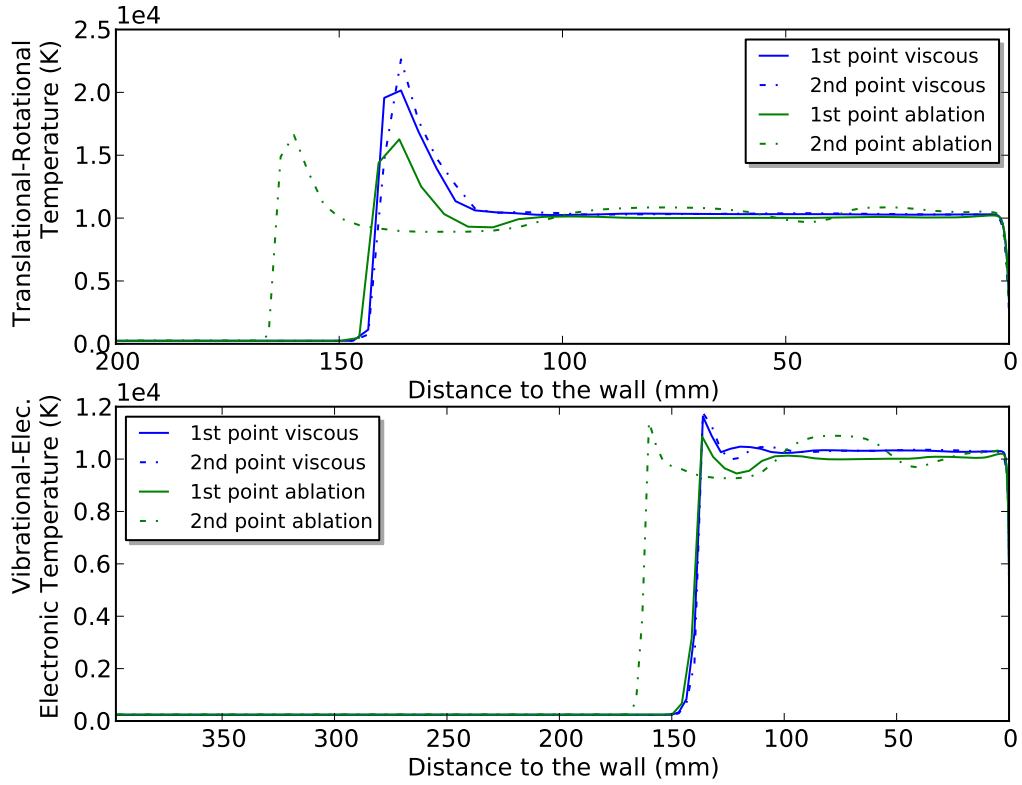

Figure 4.15: Temperature profiles for the two trajectory points, viscous flow with and without ablation

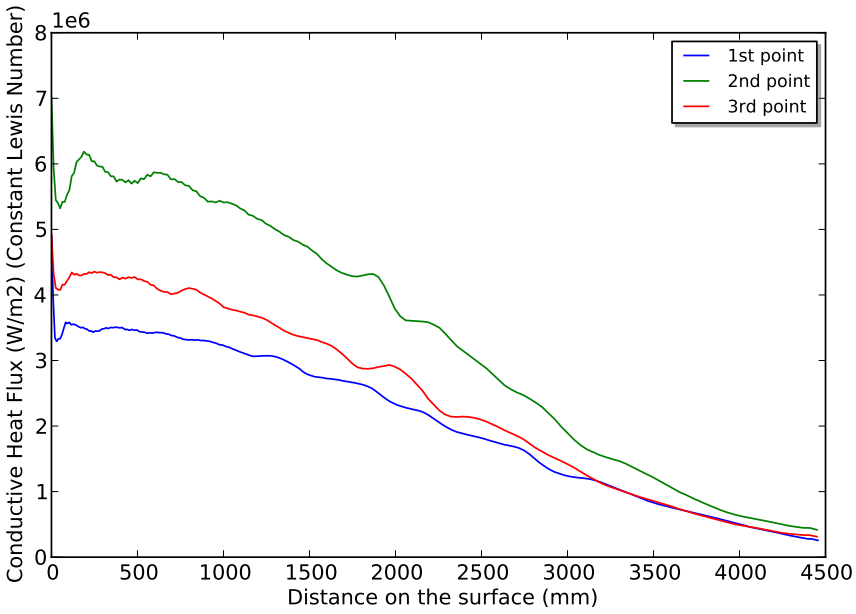

Figure 4.16: Convective Heat flux along wall surface, Constant Lewis Number diffusion model, viscous flow without ablation

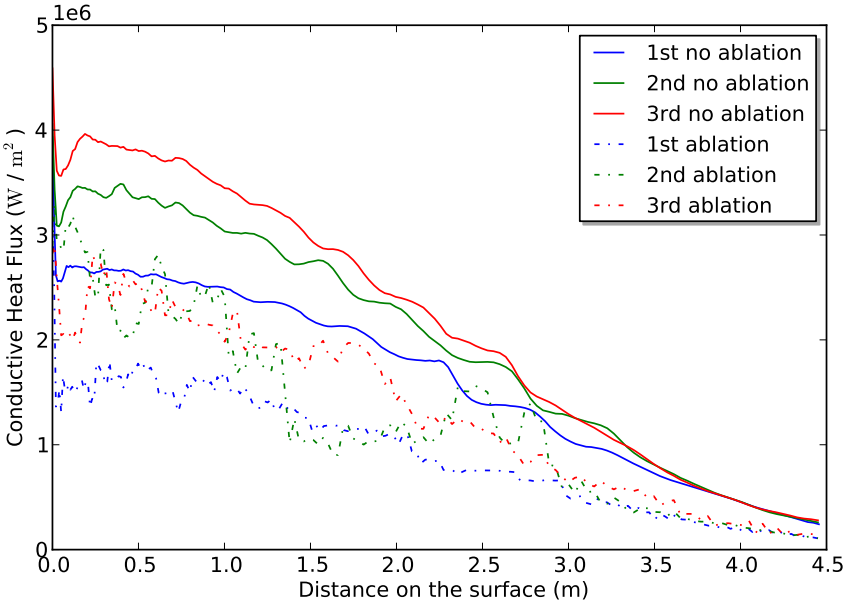

Figure 4.17: Conductive Heat flux along wall surface, Ramshaw-Chang diffusion model, viscous flow: Investigation of trajectory points heating and ablation effects

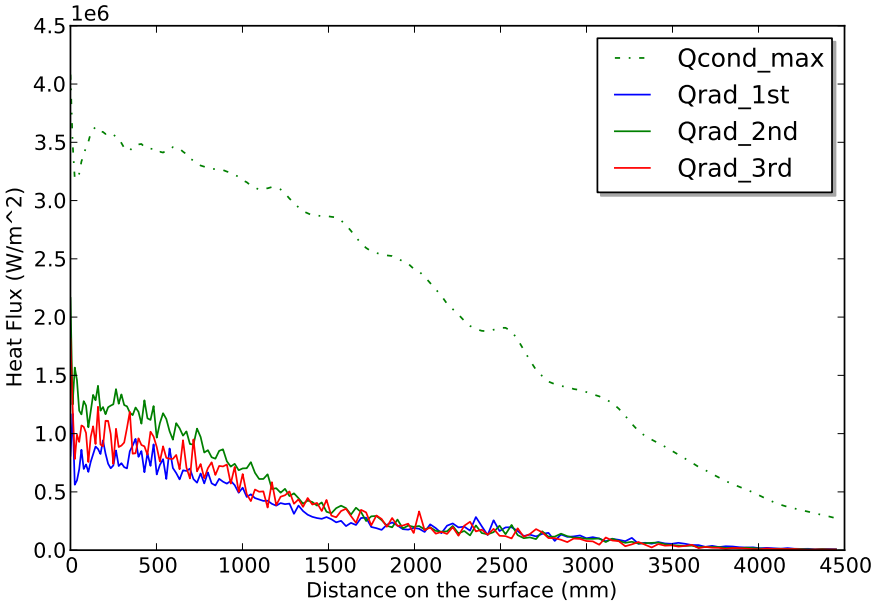

Figure 4.18: Maximum Conductive and radiative heat fluxes (for wavelength range [0.2-1.2 μm]) for the three trajectory points, Ramshaw-Chang model, viscous flow without ablation

4.2.4 Validation of the results

The following section discusses the comparison of the results obtained in the present work with results occurring from widely-used correlations for the computation of convective and radiative heat fluxes and results previously obtained by Park [29].

4.2.4.1 Semi-empirical correlations

Certain studies have been conducted in the aim of formulating an empirical solution of the convective ([4], [11]) and radiative([39], [25]) heat transfer. The present work uses the Fay-Riddel correlations for convective heating and the Tauber-Sutton correlation for radiative heating. The present results will also be compared to the results obtained by Park [29] and the ones obtained by Ried et al. [36]. The implemented correlations are based on the equation 4.1, where the characteristic length is assumed to be the blunt body radius, R_N. The semi-empirical correlations predict the convective heating to be proportionally increased with increase of the flight velocity, but inversely proportional to the square root of the nose radius of the capsule.

$$Q_{conv} \propto \sqrt{\frac{\rho}{L}} U_{\infty}^{3} \tag{4.1}$$

4.2.4.2 Bertin

As shown in Bertin [4], an approximate value for the stagnation-point heat-transfer rate can be calculated using the nose radius, the free-stream density, and the free-stream velocity:

$$q_t = C\rho_\infty^{0.5}\ U_\infty^3/R_N^{0.5}$$

,where C is a constant with a value that depends on the units chosen to describe the other parameters, ρ_∞ and U_∞ are the free-stream values of density and velocity respectively and R_N is the nose radius of the reentering vehicle. It is therefore stated that, as the stagnation-point convective heat-transfer rate depends on the stagnation-region velocity gradient at the edge of the boundary layer, the nose radius of the body clearly affects the thermodynamic state in the region: the smaller the nose radius, the higher the stagnation-point convective heat-transfer rate.

4.2.4.3 Fay-Riddel

In 1958, Fay and Riddel developed what is now the most commonly used empirical correlation for the prediction of stagnation point convective heat transfer to a blunt body [11]. The conditions considered included either fully catalytic or non-catalytic walls and either frozen or equilibrium boundary layers. The correlations for each case are presented below: For an equilibrium boundary layer:

$$(Q_{conv})_0 = 0.76Pr^{-0.6}(\rho_e\mu_e)^{0.4}(\rho_w\mu_w)^{0.1}\sqrt{\left(\frac{dU_e}{ds}\right)_0}(h_0 - h_w)\left[1 + (Le^{0.52} - 1)\left(\frac{h_D}{h_0}\right)\right] \tag{4.2}$$

For a frozen boundary layer with a fully catalytic wall,

$$(Q_{conv})_0 = 0.76Pr^{-0.6}(\rho_e\mu_e)^{0.4}(\rho_w\mu_w)^{0.1}\sqrt{\left(\frac{dU_e}{ds}\right)_0}(h_0 - h_w)\left[1 + (Le^{0.63} - 1)\left(\frac{h_D}{h_0}\right)\right] \tag{4.3}$$

For a frozen boundary layer with a non-catalytic wall,

$$(Q_{conv})_0 = 0.76Pr^{-0.6}(\rho_e\mu_e)^{0.4}(\rho_w\mu_w)^{0.1}\sqrt{\left(\frac{dU_e}{ds}\right)_0}(h_0 - h_w)\left(\frac{h_D}{h_0}\right) \tag{4.4}$$

In the above equations, Pr is the Prandtl number, ρ and μ are the density and viscosity, h is the enthalpy and Le is the Lewis number, $Le = \dfrac{\rho D_{12} c_p}{k}$, which is assumed constant. The subscripts e and w refer to conditions at the boundary layer edge and the wall respectively while the subscript 0 refers to the stagnation values. The term h_D is the dissociation

enthalpy and is calculated as follows:

$$h_D = \sum_i Y_i (\Delta h_f)_i^0 \tag{4.5}$$

,where Y_i is the mass fraction of species i and $(h_f)_i^0$ is the enthalpy of formation of species i.

The velocity gradient, $\left(\frac{dU_e}{ds}\right)$ has a significant effect on the solution to the above equations. Therefore the method used to calculate it is extremely important. This term was calculated by Fay and Riddel via applying the one-dimensional momentum equation for a near stagnation point streamline and Newtonian theory, resulting in:

$$\left(\frac{dU_e}{ds}\right)_0 = \frac{1}{R_N}\sqrt{\frac{2(p_0 - p_\infty)}{\rho_0}} \tag{4.6}$$

where R_N is the nose radius, p_0 and ρ_0 are stagnation pressure and density respectively and p_∞ is the flow pressure.

4.2.4.4 Martin

The analysis developed by Martin [25] indicates that the gas-to-surface radiation for a reentry vehicle may be estimated as:

$$q_{r,t} = C\ R_N \left(\frac{\rho}{\rho_{SL}}\right)^{1.6} \left(\frac{U_\infty}{10000}\right)^{8.5}$$

where C is a constant with a value that depends on the units of the other parameters. As it is observed from the above relation, the radiative heating rate is proportional to the nose radius; thus, the bigger the nose radius, the higher the stagnation point radiative heat-transfer rate.

4.2.4.5 Tauber-Sutton

Tauber and Sutton [39] formulated an analytical expression, equation 4.7 to calculate the stagnation-point radiative heating for re-entry into Terrestrial and Martian atmospheres. In this project, only Earth re-entry has been studied and hence only parameters associated with this case are given below.

$$(Q_{rad})_0 = C R_N^a \rho_\infty^b f\left(U_\infty\right) \tag{4.7}$$

where radiative heating is in W/m^2, nose radius (R_N) in m and density (ρ_∞) in kg/m^3. For Terrestrial cases, the values of C, a and b are given:

$$
\begin{aligned}
C &= 4.736 \times 10^4 \\
a &= 1.072 \times 10^6 U_\infty^{-1.88} \rho_\infty^{-0.325} \\
b &= 1.22
\end{aligned}
\tag{4.8}
$$

and the velocity function $f(U_\infty)$ is found from table 1 in [39]. Equation 4.7 is valid for earth entries for flight speeds between 10-16km/s, altitudes of 72 to 54km and nose radii varying between $0.3 - 3.0m$.

4.2.4.6 Results Discussion

The comparative results between correlations, previously obtained results and the results obtained in the present study are summarized in Table 4.1. The values of all the calculated values of correlations are taken from [29]. The radiative heat flux values are the ones calculated with the use of the Monte-Carlo radiation transport model. It is also noticed that, although in the beginning the radiation calculations were performed in the wavelength range between 0.06-4 mm, the spectra analysis (see figure 4.8) revealed that the wavelength range from 1.2 to 4 mm could be ignored, as its participation in the total spectra is minimum.

	Value at mission time		
Quantity	30,024 s	30,032 s	30,040 s
Free-stream velocity (m/s)	$10,511$	$10,252$	$9,798$
Free-stream density (kg/m^3)	$1.73 \cdot 10^{-4}$	$3.41 \cdot 10^{-4}$	$5.01 \cdot 10^{-4}$
Flight $I_{r,w}(0.24)$ $(W/(cm^2 sr))$	10.5	25	16
Flight $q_{r,w}(0.064)$ $(W/(cm^2))$	111	264	170
Ried et al. $q_{r,w}(0.064)$ $(W/(cm^2))$	137	300	179
Tauber-Sutton $q_{r,e}(0.064)$ $(W/(cm^2))$	169	237	149
Fay-Riddel q_c $(W/(cm^2))$	176	230	176
Park shock standoff distance (cm)	14.1	15.1	15.1
Park $q_{r,w}(0.064)$ $(W/(cm^2))$	97.9	168	117
Park q_c,radiation uncoupled $(W/(cm^2))$	94.6	118	153
Present study			
Shock standoff distance (cm)	14.5	15.8	14.8
$q_{r,w,MC}(0.064)$ $(W/(cm^2))$	139.1	242.7	164.7
$q_{r,w,MC}(0.24)$ $(W/(cm^2))$	65.8	109	104
$q_{c,viscous}$ $(W/(cm^2))$	393	405.8	492.7
$q_{c,ablation}$ $(W/(cm^2))$	136	289.5	382

Table 4.1: Comparison results for the convective and radiative heat fluxes for the Apollo 4 front body

From the above table, it is observed that the results obtained in this study are qualitative valid. They are consistent with all the correlations and previous studies. The calculated convective heating values are a little higher than the Fay-Riddel correlations and Park's

results, but still consistent. The extreme difference in the calculated convective heat flux for the third trajectory point could be addressed to the fact the Park used different equations for the first two trajectory points and the third one, in order to calculate the convective heatflux with the Fay-Riddel correlation. For this work, a calculation of the same values was performed, using only the form of the Fay-Riddel correlations for a frozen boundary layer with a fully catalytic wall and the values calculated were:

Fay-Riddel q_c $(W/(cm^2))$	135	288	537
$q_{c,ablation}$ $(W/(cm^2))$	136	289.5	382

It seems that the third point should not be addressed as a case of a frozen boundary layer with a fully catalytic wall, as the value calculated is 1.5 times higher than the one calculated with the simulations, whereas the values for the other two points correlate at a great level. Nevertheless, it should be noticed that in order for the Fay-Riddel correlations to be calculated a Lewis number should be given. However, with the Ramshaw-Chang diffusion model used the Lewis number does not remain constant throughout the simulations.

Regarding the radiative heat fluxes calculated, on the other hand, the correlations' values and the flight data are extremely similar to the ones calculated in the simulations performed with Eilmer3.

Part III

Numerical Simulations in 3D

Chapter 5

Simulations in 3D

This chapter thoroughly discusses the procedure someone has to follow to obtain results for the 3D simulation cases, using two 3D solvers, CFD++ [27] and NSMB [42], from the geometry and the mesh generation to running a simulation with each solver. Finally, the main results of the 3D calculations are presented and the two solvers are compared to each other, according to the results they produce and their ease of use.

5.1 General Procedure

The three-dimensional simulations were performed with the use of different software, in order to create the geometry of the capsule and the flow domain, generate the mesh and prepare and run the simulations.

Geometry configuration

The geometry of the capsule and the flow domain around was created with the use of *SolidWorks*, a simple 3D CAD program. The geometry, after being created in Solidworks, was exported in a *Parasolid* format, which is compatible with the mesh generation software.

Mesh Generation

ICEM CFD is a mesh-generation software which provides advanced geometry acquisition, mesh generation, and mesh optimization tools. The input required is just the geometry of the model, which can be imported in a Parasolid format, as was done in the present work. The generated mesh can be one of or a combination of different elements: tetrahedral, hexahedral, prisms, pyramids, etc.

The generic working process involves the following:

1. Open/Create a project.
2. Create/Manipulate the geometry.
3. Create the mesh.
4. Check/Edit the mesh.
5. Generate the input for the solver.

For the 3D simulation case of a space capsule in atmospheric entry ([12] [38]) , the imported geometry is manipulated and topologically fixed, in order to obtain a geometry separated in different parts, indicating the boundary surfaces of the domain. Afterward, the blocking is formatted, utilizing the O-grid splitting tool of ICEM, and from the structured blocks the mesh is generated. Finally, the input files for each solver are extracted.

Solvers and Post-Processing

The simulations took place with the use of the flow solvers *CFD++* and *NSMB*, in which the simulation parameters, chemistry model, initial and boundary conditions and numerical information were set.

Concerning the simulations performed, because of the computational power required, the EPFL Bellatrix cluster was used, in order to minimize the computational time. Therefore, out of the different jobs that were ran on the Bellatrix cluster, the Eilmer3 codes jobs were split into 64 blocks and utilized 4 nodes of 16 processors each. On the other hand, the CFD++ simulations were performed using one node with 16 processors.

5.1.1 Protocol

As part of the present project, two 3D test cases were performed; the first was the simulation of the flow-field, considering only the front body of the Apollo Command Module, so that the parameters and the steps of the simulation are better understood. This test case focuses on the radiation and ablation in the shock and boundary layer respectively, so that the results can be compared to the actual flight data of the Apollo CM.

The second case is set up, considering the whole body of the Apollo Command Module (fore- and after-body), seeking to simulate the flow-field around the whole capsule and possibly calculate some after-body radiation.

The protocol for both the simulation cases is the following: The first step is the creation of the 3D geometry file of the capsule and the flow domain around it, with the use of 3D CAD software. The second step is the generation of the mesh suitable for the fluid

domain. Important aspects of the mesh generation are the refinement of the grid and the distributions, according to the application. The third step is the actual numerical simulation procedure and the solution acquirement. The final step is the post processing of the solution files, and the visualization of the results.

Both the above mentioned cases are performed with the following flow models:

1. Perfect gas model- Inviscid flow
2. Real equilibrium gas model Inviscid flow
3. Real non-equilibrium gas model Laminar flow

5.2 Pre-processing

5.2.1 Geometry Configuration

The Apollo 4 geometry was a 57 deg sphere-segment of radius $4.69m$ with a sphere-cone after-body as presented in Figure 1a and b. The coordinates of the nodes are given below in figure 5.1. The lengths are given in meters.

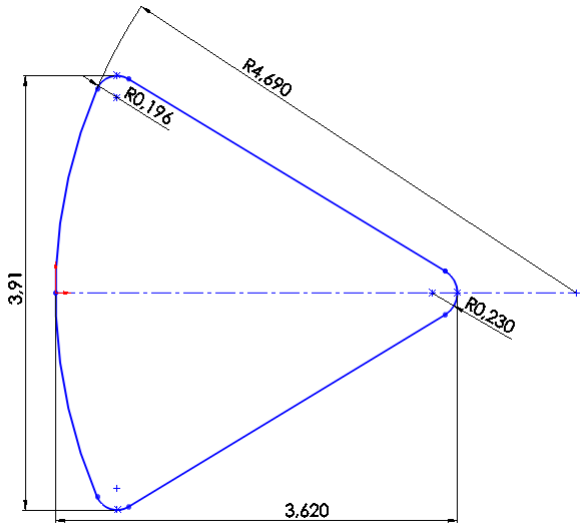

Figure 5.1: The geometry profile of the Apollo Command Module

.

With the use of the 3D CAD Software *SolidWorks*, the geometry of the fore-body of the Apollo Command Module and the flow domain around it is formed as illustrated in figure 5.2, whereas the whole body of Apollo 4 is illustrated in figure 5.3. It is noticeable that the domain around the capsule is not symmetrical, so that the symmetry axis of the capsule and the outer domain form an angle of 25.5 deg between them, indicating the angle of

attack during the capsules atmospheric entry. This also assists the evolution of the non-symmetrical shock in front of the reentering body. The distance between the edge of the domain and the wall boundary is 1 m.

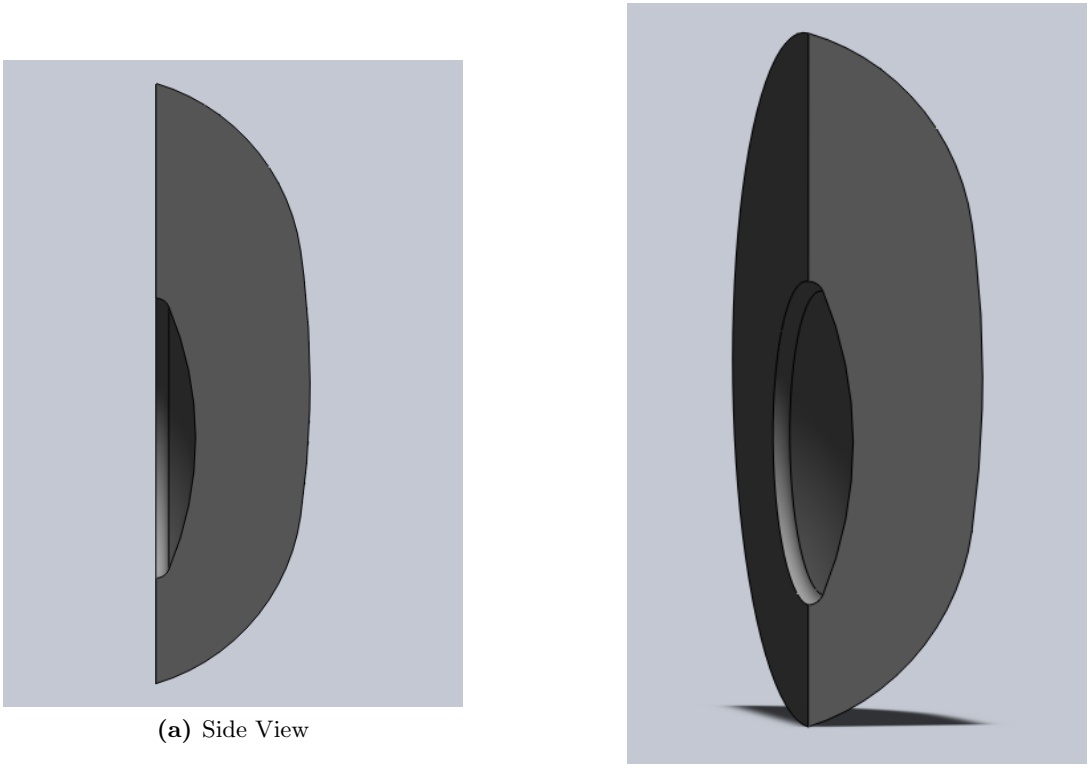

(a) Side View

(b) Isometric View

Figure 5.2: The geometry of the Apollo 4 front-body and the flow domain around it

5.2.2 Mesh Generation

The following section describes in detail the entire procedure to generate the mesh required for the front-body and the whole-body 3D simulations of the Apollo 4 capsule.

5.2.2.1 Fore-Body

The mesh generation of the fore-body case of Apollo 4 is completed in the following steps. An explanatory picture compliments each step for better understanding:

1. Once the geometry is exported from the 3D CAD program in *parasolid* format, the geometry is imported in the Mesh Generation Software, *ICEM CFD*, and the different parts are distinguished, so that the geometry is split in 4 different parts, each containing one boundary surface. Moreover, two bodies are created, one indicating the Fluid and one indicating the Solid domain. This configuration is illustrated in figure 5.4.At that stage, the topology tolerance should be changed from the default of 0.005 to at least 0.000001, if the sizes are set to be measured in meters, as in this

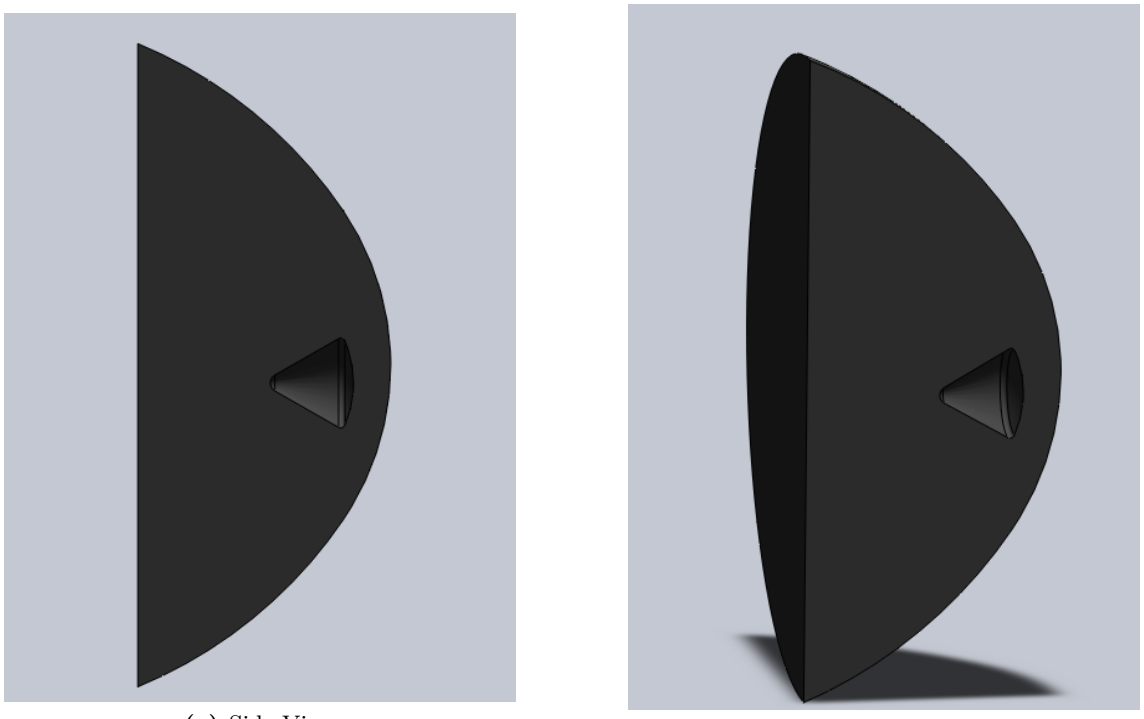

(a) Side View

(b) Isometric View

Figure 5.3: The geometry of the Apollo 4 entire body and the flow domain around it

project. This assists the the topology rebuilt of the geometry and the association accuracy of the blocking with the geometry.

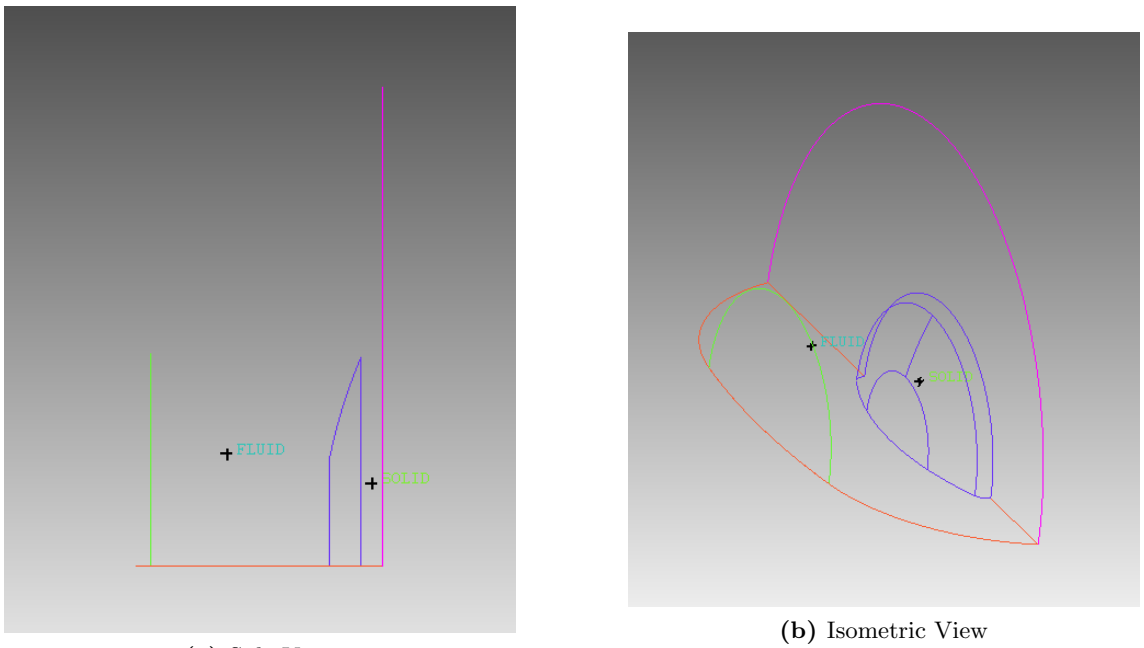

(a) Side View

(b) Isometric View

Figure 5.4: The geometry of the Apollo 4 flow domain and the individual parts as divided in according to the boundary surfaces

2. The initial block is generated and is split in the y direction one time, while the associated vertices are being snapped on to the domains boundary surfaces. Notice that the vertices in the hollow Apollo 4 body should be disassociated from any surface, so that they are not falsely projected on the Apollo 4 front wall.

3. Making several consecutive O-grid splits by selecting as starting surfaces for the O-grid the surfaces on the wall boundary, the solid body of the Apollo Command Module is gradually formed.

4. After that, the blocks inside the Apollo body are grouped together and added to the Solid part. Once this is done a final O-grid split is done around the blocks of the solid part at an absolute distance of 60 cm. This final O-grid is formed in order the user to be able to refine the mesh around the solid wall in the boundary layer and to capture the shock wave. The final blocking topology is illustrated in figure 5.5. After creating the final blocking the Solid Part, containing the negative volumes inside the capsule body should be de-activated from the parts scroll-down menu.

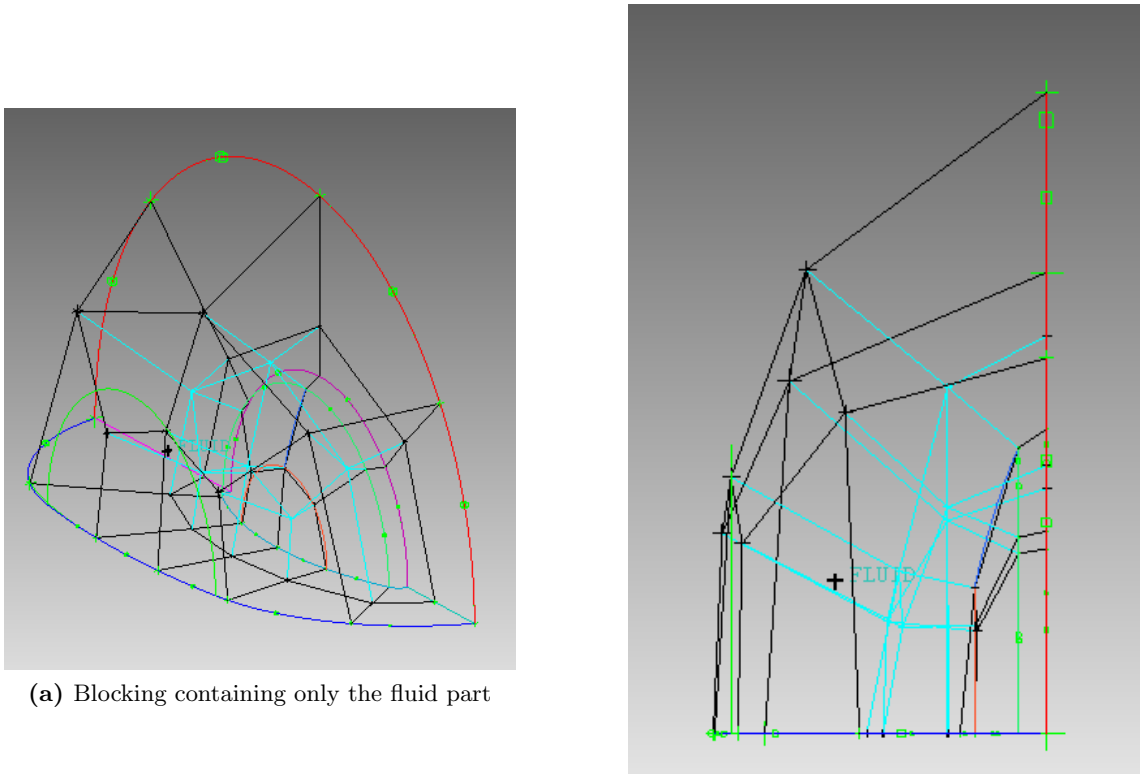

(a) Blocking containing only the fluid part

(b) Side view

Figure 5.5: The blocking of the Apollo 4 fluid domain

5. Afterwards, the actual mesh generation begins, as the max size, height and height ratio are set universally for the different parts of the project.

6. The final step of the procedure is the refinement and the change of the distributions along certain edges of the blocks in the shock- and boundary layer regions, in order to capture the extreme gradients of the conservative variables of the flow. , Typical values of the cell sizes near the wall boundary are below 0.01 mm,especially if viscous flow models are used. Notice that, in order the quality of the mesh to be good, the topology tolerances should be smaller than the size of the smallest cell (and that should be changed every time in the ICEM Settings Menu). The mesh generated for the fore-body case is depicted in figure 5.6. The final mesh for this case consists of ≈ 3.5 million cells.

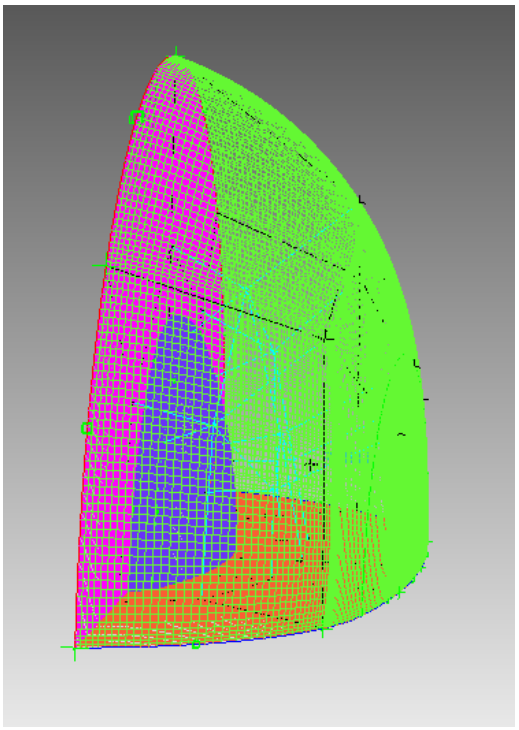

(a) Overview of the mesh

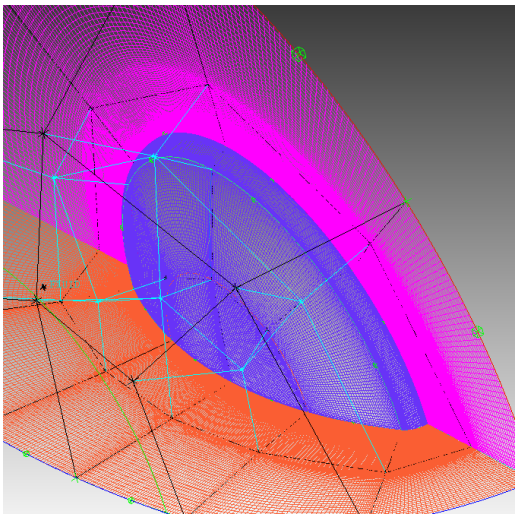

(b) Detail of the refinement in the shock layer region

Figure 5.6: The mesh generation of the Apollo 4 fluid domain

7. The above mentioned procedure is an iterative process, as every time a change is made, it should be checked if the blocking and the mesh qualify for some quality criteria. For the fore-body case the quality control with the Determinant 3x3x3 criterion proved that the blocking was excellent, as it is noticed in table 5.1 and in 5.7. As can be seen from the quality control panel, all the cells have a determinant 3x3 more than 0.924. Moreover, the vertices should be located in a way that the mesh is orthogonal to the boundaries and not skewed.

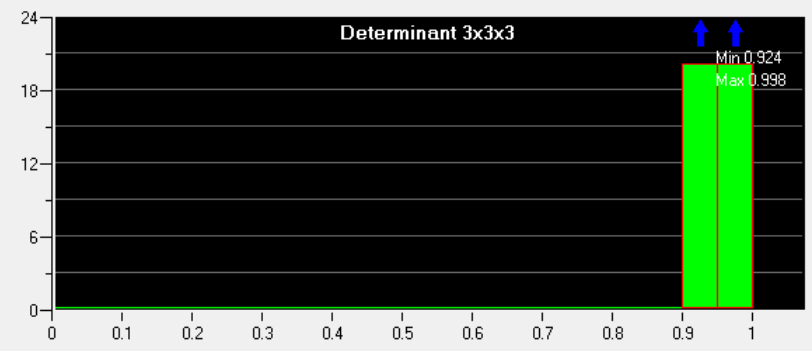

Figure 5.7: The 3x3x3 determinant quality check results for the above blocking
.

Determinant margin	Percentage of cells	Number of cells
$0 \rightarrow 0.9$	0.0%	0
$0.9 \rightarrow 0.95$	5.728%	174305
$0.95 \rightarrow 1.0$	94.272%	2868595

Table 5.1: The results for the quality check concerning the 3x3x3 determinant

It should be noticed that the mesh generated for import in CFD++ ought to be different from the one imported in NSMB. The NSMB solver can deal better with larger aspect ratios and the cells on the wall surface do not need to be extremely small and square-shaped. Moreover, the solver itself doesn't deal well enough with refinements on directions other than the the one parallel to the stagnation streamline. This leads to a good-quality mesh (determinant quality criterion values above 0.9) with a number of cells equal to 1.6 millions, as the one illustrated in figure 5.8.

On the other hand, the mesh imported in NSMB should not only be of a good quality, according to the determinant criterion, but also according to aspect ratios. The solver is also very sensitive to refinement, which should be gradually configured in the whole domain. Because of the sophisticated heat-flux calculation techniques implemented in CFD++, the mesh on the surface of the capsule should also be of a very good quality and the cell sizes small enough (normally less than 5 mm). This results to a mesh with more than double the number of cells of the mesh prepared for NSMB, as the one illustrated in figure 5.9 for the Apollo front-body. Moreover, it is important to examine the simulation solution independence of the mesh. For the front body simulation case, it is evident from figure 5.10 that the residuals for a mesh of 3.6 million cells are not reducing more than 2 orders of magnitude and the solution does not converge, whereas the same case with a mesh of 7.5 million cells converges not only faster, but the global residuals of the simulation reduce 4 orders of magnitude for the same simulation time.

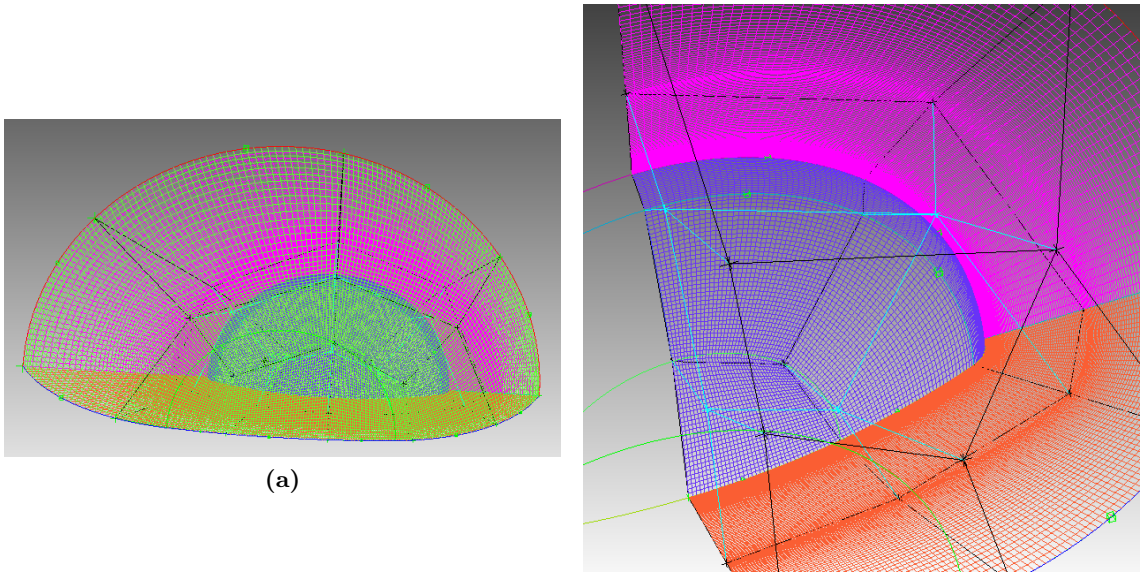

(a) (b)

Figure 5.8: The mesh of the front-body as used for the NSMB solver

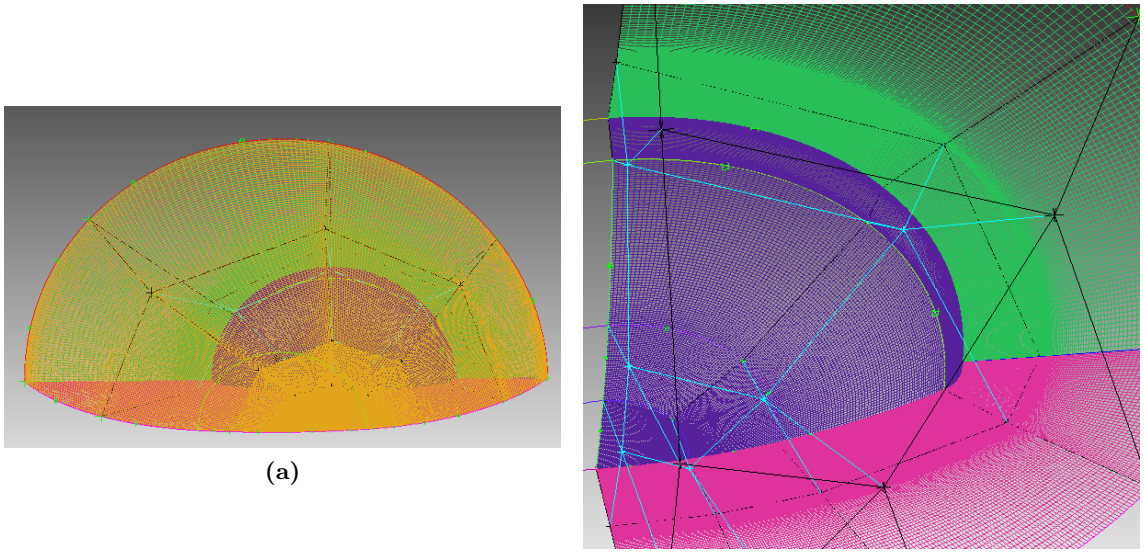

(a) (b)

Figure 5.9: The mesh of the front-body as used for the CFD++ solver

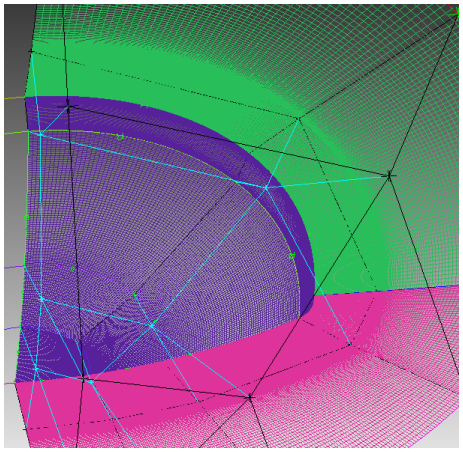

(a) Mesh of 7.1 mil. cells

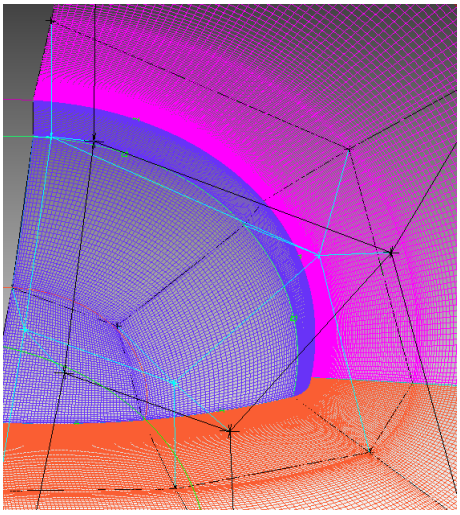

(b) Mesh of 3.6 mil. cells

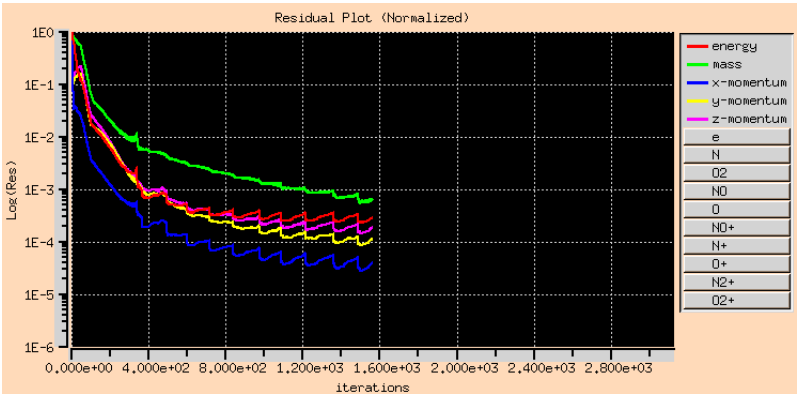

(c) Residuals for simulation with the mesh of 7.1 mil. cells

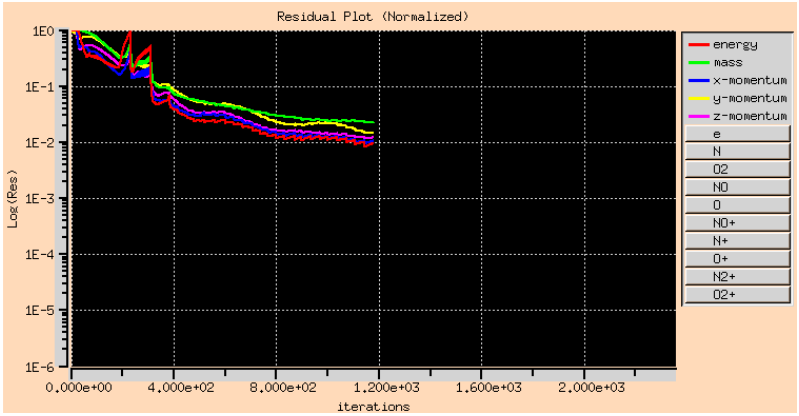

(d) Residuals for simulation with the mesh of 3.6 mil. cells

Figure 5.10: Investigation of convergence independence of mesh

5.2.2.2 Whole Body

The mesh generation of the entire body case of Apollo 4 is completed in the following steps. An explanatory picture compliments each step for better understanding:

1. As already mentioned in the previous section, the geometry is split in 4 different

parts, each containing one boundary surface, while the Fluid and Solid parts are created. This configuration is illustrated in figure 5.11.

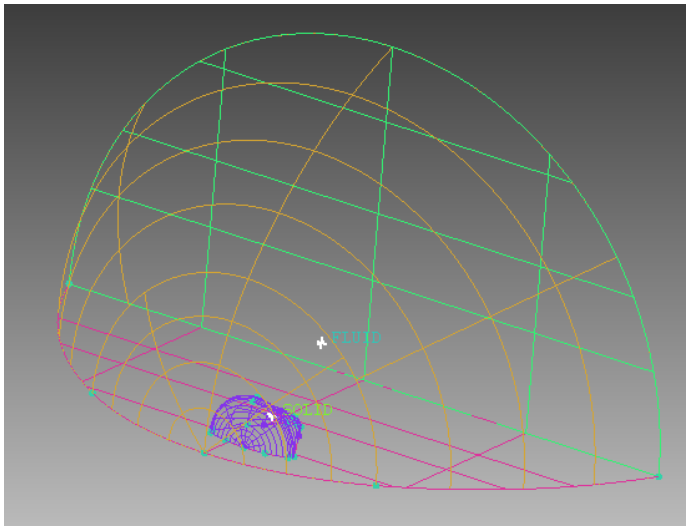

Figure 5.11: The geometry of the Apollo 4 flow domain as configured in ICEM

2. The initial block is generated and is split in the y direction one time, while the associated vertices are being snapped on to the domains boundary surfaces (see figure 5.12).

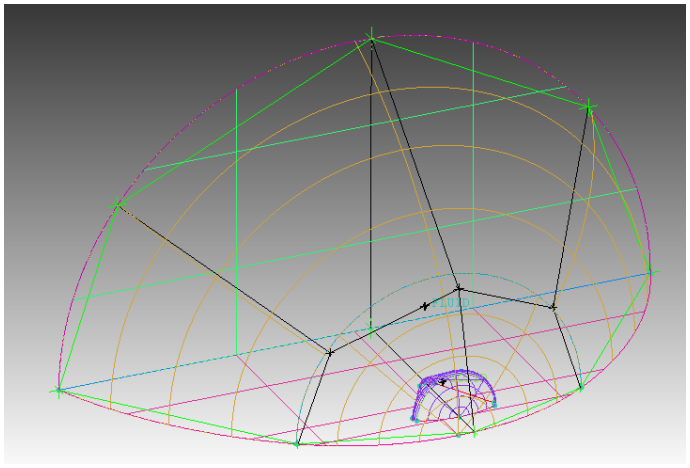

Figure 5.12: First split of blocking

3. Several consecutive O-grid splits with starting surfaces for the O-grid the surfaces on the wall boundary of the front body lead to the configuration shown in figure 5.13. An O-grid split is done for the volumes in the front part of the Apollo Body, just as presented in the previous section.

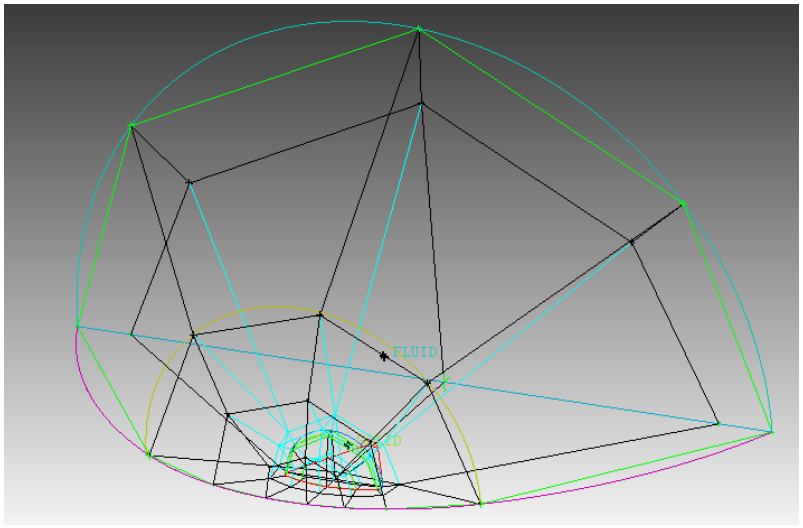

(a)

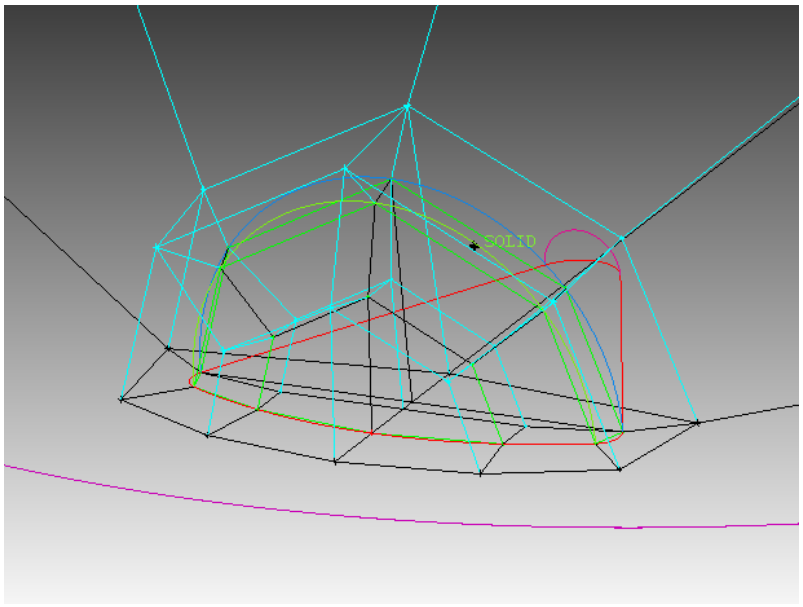

(b) Detail of the mesh around the body

Figure 5.13: O-grid splits of the blocking

4. The blocks created by the last O-grid split in the back body are unnecessary and should be deleted. This step is shown in figure 5.14. The two figures present the same part of the domain before and after the deletion of the 4 unnecessary blocks. To be exact, these blocks interfere with the mesh strategy required, as the back flow of the body should not be meshed with an O-grid.

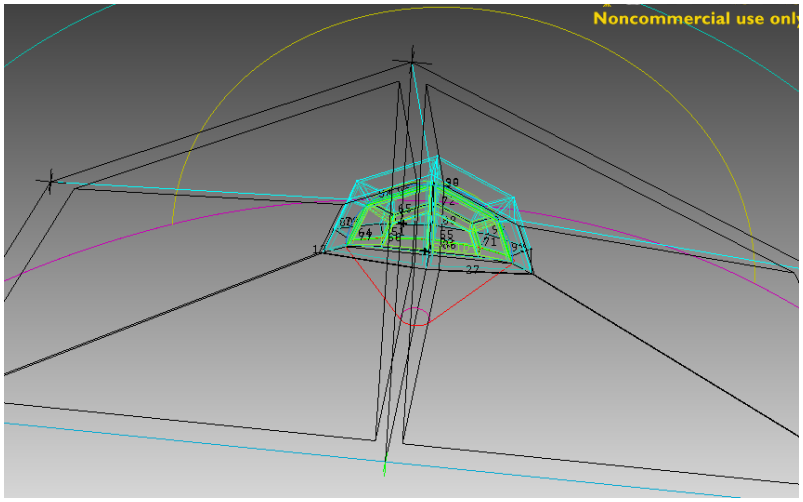

(a)

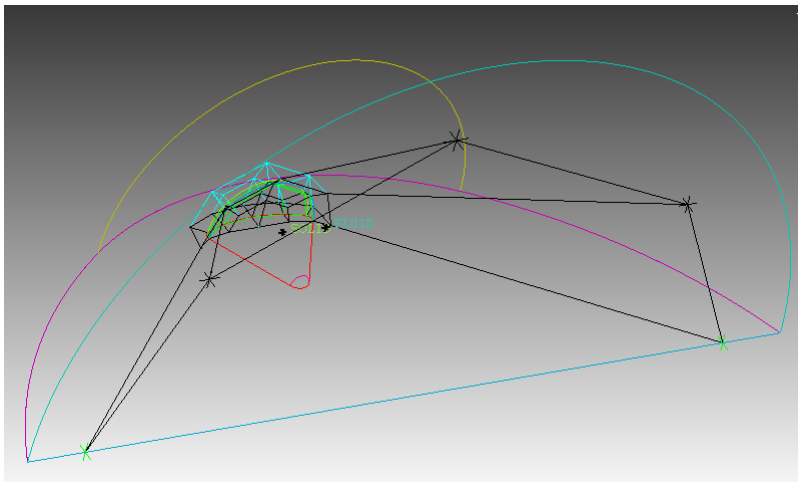

(b)

Figure 5.14: Deletion of unnecessary blocks

5. Afterwards, new blocks are created by extraction of the remaining surfaces. Attention should be payed in the direction of the extracted new blocks. The user has to have in mind that the new blocks should be created first from the surfaces that are neighboring with existent positive surfaces. Keeping this in mind, the first volumes created are the volumes in the back body of the solid part, the capsule itself. This step is shown in figure 5.15.

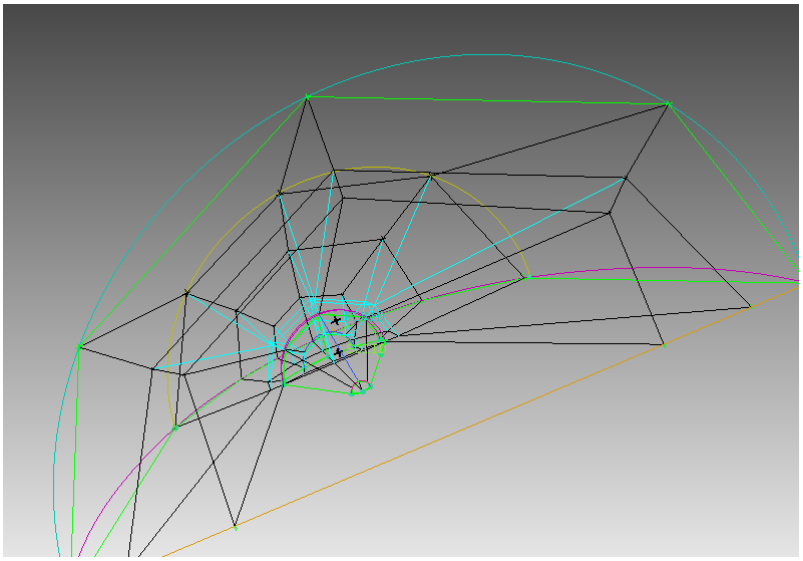

Figure 5.15: Creation of new hexa blocks for the back-flow part of the domain from existing surfaces

6. The final image of the blocking is illustrated in figure 5.16. The blocking of this case consists of 50 mapped blocks.

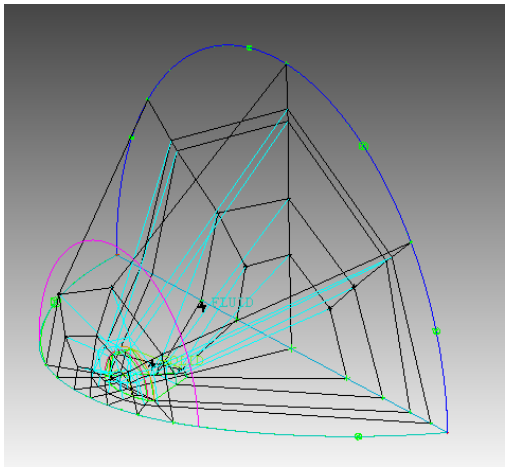

(a) Overview

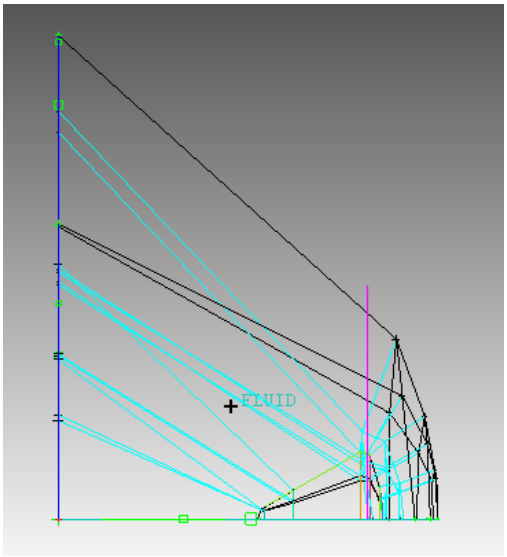

(b) Side view

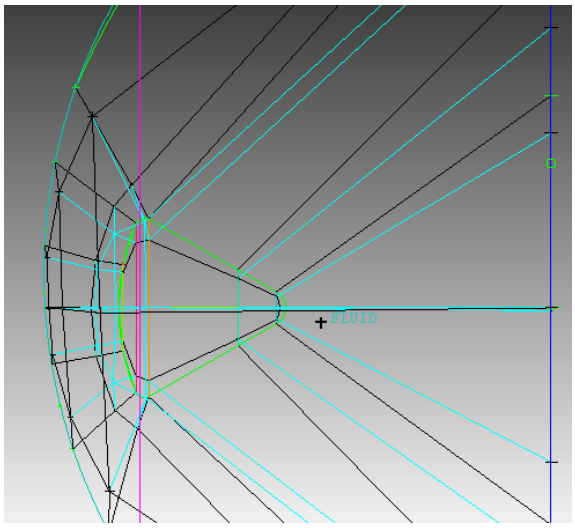

(c) Top view

Figure 5.16: Final view of the blocking

7. After the set up and the refinement of the mesh the final view of the domain is the one illustrated in figure 5.17. The mesh consists of ≈ 20 mil. cells. For the whole-body case the quality control with the Determinant 3x3x3 criterion proved that the blocking was excellent, as it is noticed in table 5.2 and in 5.18. As can be seen from the quality control panel, all the cells have a determinant 3x3 more than 0.903.

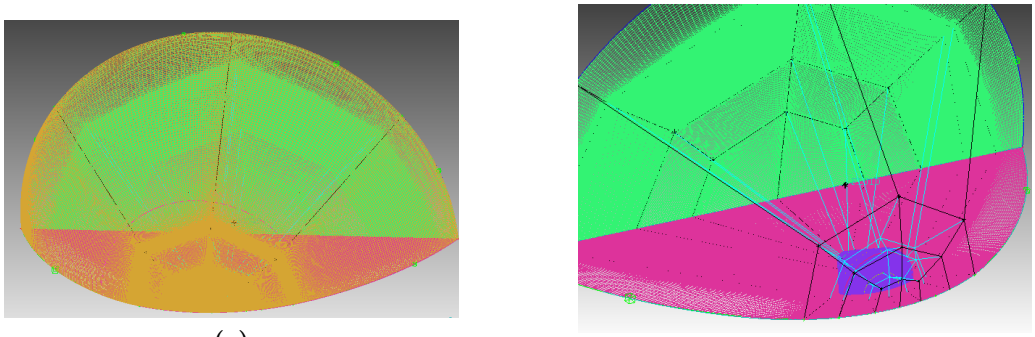

(a) (b)

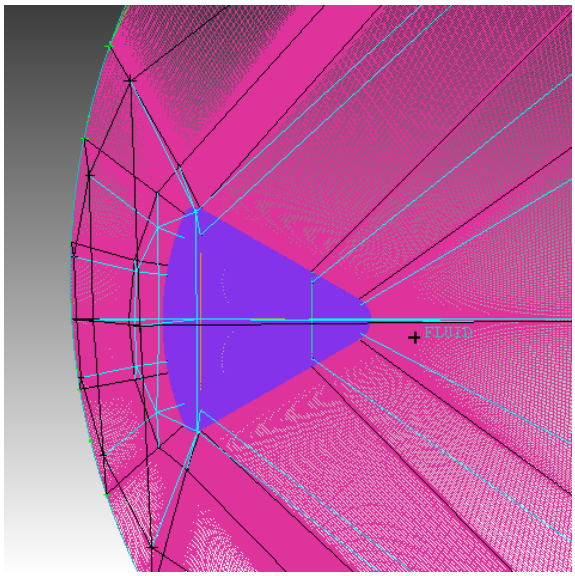

(c)

Figure 5.17: The mesh of the whole-body case

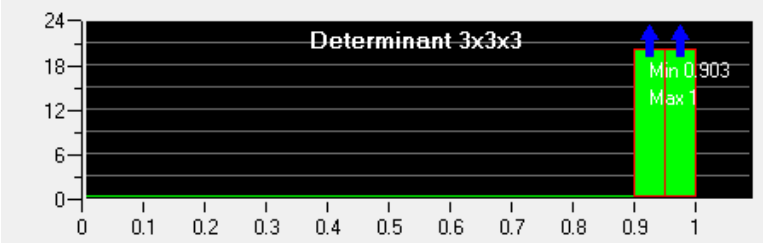

Figure 5.18: The 3x3x3 determinant quality check results for the blocking for the whole-body case

Determinant margin	Percentage of cells	Number of cells
$0 \rightarrow 0.9$	0.0%	0
$0.9 \rightarrow 0.95$	4.301%	864405
$0.95 \rightarrow 1.0$	95.699%	19232057

Table 5.2: The results for the quality check concerning the 3x3x3 determinant

Mesh Output Format

The structured mesh generated with ICEM CFD is exported as an unstructured mesh for the CFD++ solver and the input files for CFD++ are created with the use of the output file tool. On the other hand, the required mesh type for NSMB is a Multi-block mesh, which is created from the existent blocks in ICEM. The boundary conditions for NSMB are also defined in ICEM with the use of the Boundary Condition output tool of ICEM, using the Generic output format, and indicating each boundary condition with a specific integer, as indicated in the NSMB User Guide [42] . For the simulation cases of this work, the following boundary conditions have been selected: Inflow → 130 (Free-stream conditions), Outflow → 134 (Far field using Riemann invariants), Symmetry → 410 (General symmetry plane) and Apollo 4 wall → 300 (Solid Wall).

5.3 Fore-Body Simulations

The following section presents the results of the simulations concerning the front body of Apollo 4 with both the solvers used.

In the beginning the results of the CFD++ simulations for the front-body case: For a viscous flow model, five chemistry models are implemented and compared; a perfect gas model (total of 5 equations, equal to the 5 basic equations), a real-gas 5-species equilibrium model (a total of 9 equations= 5 basic and 4 species equations) and non-equilibrium model (a total of 10 equations= 5 basic, 4 species and 1 extra energy equation due to non-equilibrium) and a real-gas 11-species equilibrium (a total of 15 equations) and non-equilibrium model (total of 16 equations). The CFD++ cases are run with a radiative heat transfer wall boundary condition and a super-catalytic wall condition. In the second part of this section the results from the NSMB simulation cases are presented. The chemical model implemented fore this cases is a real gas 5-species model, whereas comparison is made between three gas state models; equilibrium, chemical non-equilibrium and thermal non-equilibrium.

The last part of this section compares the two solvers in means of accuracy of the solution and simulation time required for the 5-species thermal and chemical equilibrium model.

The following simulations are performed with the assumption of viscous flow, considering the flow to be laminar if viscous. This is accurate in Hypersonic flow-fields, as the Mach number is extremely high and the density extremely low due to the high altitudes.

The simulations are performed for the second of the three trajectory points of those given in table 2.1. This trajectory point was chosen, as it is the peak radiating point of the tra-

jectory and thus, the different thermo-chemical models are expected to make a difference in the results. The simulation parameters are summarized below:

Density $[kg/m^3]$	Mach	Velocity $[km/s]$	Temperature $[K]$	Pressure $[Pa]$
$3.41 \cdot 10^{-4}$	32.4	10.252	249.16	24.39

5.3.1 CFD++ Simulations

In the following section, the results for the CFD++ simulations are presented for 5 different thermo-chemical models: perfect gas, 5-species real gas equilibrium and non-equilibrium, 11-species real gas equilibrium and non-equilibrium.

The entire set of simulation results as contours are thoroughly presented in the Appendix. In this section the results are presented mainly extracted for the stagnation stream-line and the wall surface with the "xyz Extraction tool" from the CFD++ Meta-Visualizer.

5.3.1.1 Viscous Flow- Perfect gas model

For this simulation the wall boundary is considered to be a viscous (no-slip) adiabatic wall. This means that the temperature is not expected to reduce on the wall boundary. As can be seen in figure 5.19, the presented simulation is considered converged at 1000 iterations, as the residuals drop to the order 10^{-4}.

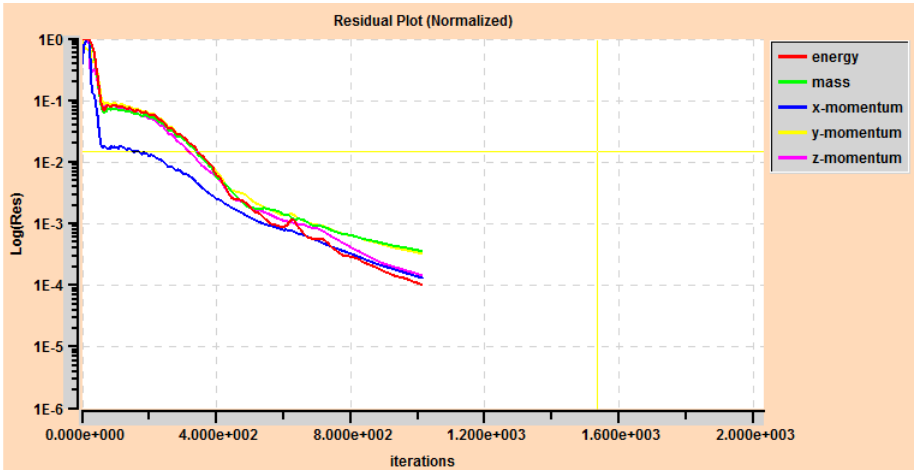

Figure 5.19: Convergence criteria for perfect gas model

The pressure and temperature contours in the flow-field are displayed in figure 5.20. It is obvious that the specific model is not a representative of the thermochemical phenomena occurring in the shock layer, as the temperature of the wall surface is greater than the temperature in the shock layer,while the maximum temperature value, 57854 K, which is a completely exaggerating value.

The zero velocity (figure 5.21) on the wall validates the no-slip boundary condition imposed on the wall. From the Mach number sub-figure, it is obvious that the mesh was not entirely suitable for this flow model. It is also worth-mentioning that the flow-field proves to be

non-symmetrical around the capsule face, due to the induced angle of attach. The shock-standoff distance for this case is 0.5 m. Finally, the Y+ maximum value for this case is 0.18, which is considered perfectly adequate.

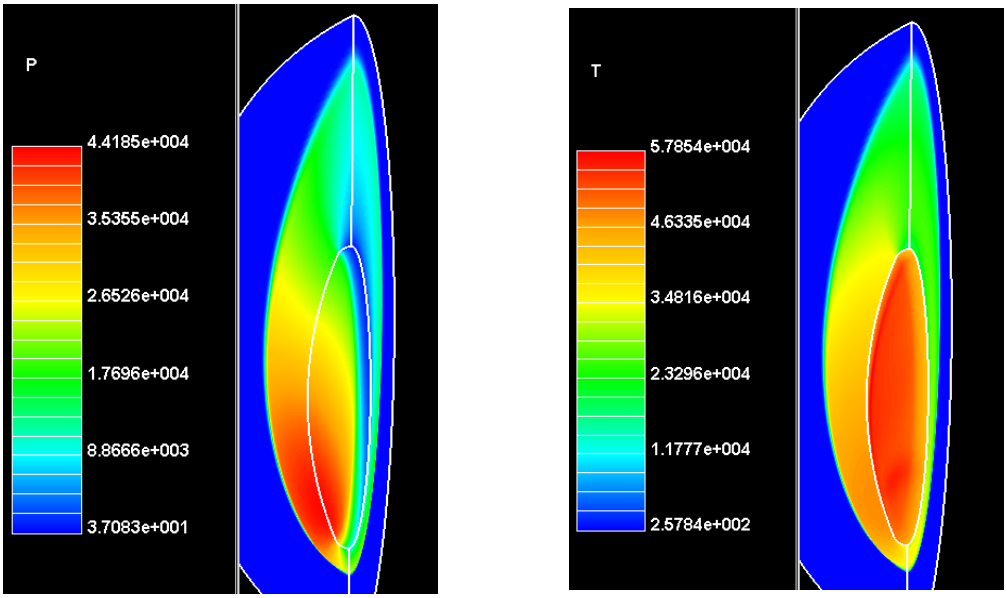

(a) Pressure field **(b)** Temperature field

Figure 5.20: Pressure and temperature field for perfect gas model

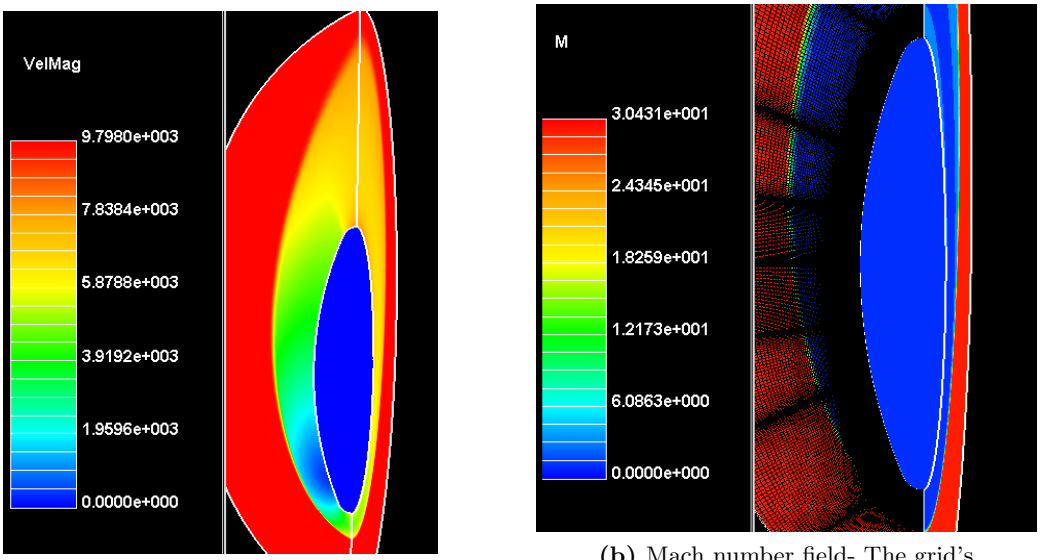

(a) Velocity magnitude field

(b) Mach number field- The grid's unsuitability to the flow model

Figure 5.21: Mach number and velocity field for perfect gas model

5.3.1.2 Real 5-species equilibrium gas model

For this simulation the chemical model used consists of 5 species: $N_2, O_2, NO, NandO$. The specific model is, therefore, not taking into consideration any ionization processes in the flow-field. The wall boundary is considered to be a super-catalytic, radiative heat transfer wall with the emissivity set to 0.85.

This simulation was considered converged after 630 iterations, as the residuals dropped to the order of 10^{-4}. Moreover, the quality and suitability of the mesh is validated by the smoothness of the convergence history for this case (figure 5.22).

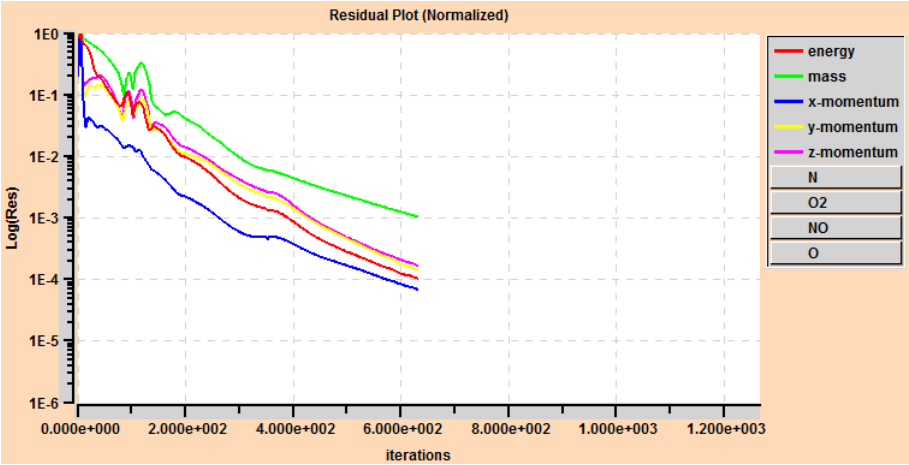

Figure 5.22: Convergence criteria for 5-species real gas model in equilibrium

For this case, the flow-field parameters are presented mainly along the stagnation line and the wall surface. Figure (5.23) shows the pressure and velocity profile along the stagnation line. It is observed that the shock stand-off distance is less than half of the one for the perfect gas case; its exact value is 0.15 m. This is correct and expected, as the existence of species in the shock layer increase the density of the shock layer, thus its size is reduced. From the Mach number contour detail (5.24), it is obvious that the grid is capturing better the shock in this case than the perfect gas one.

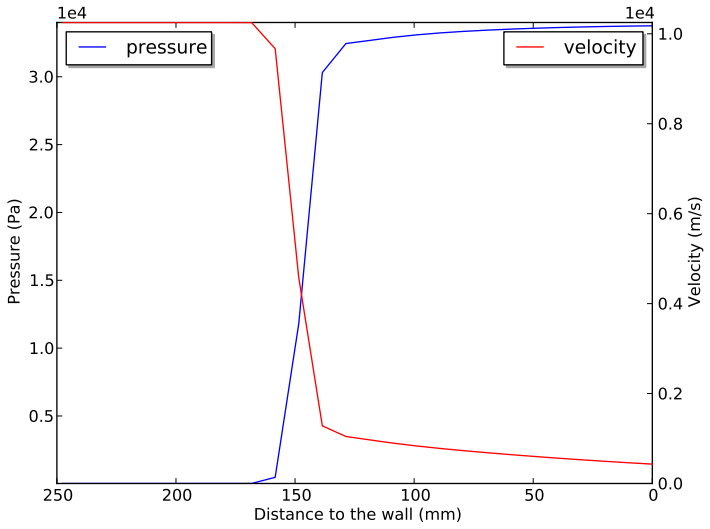

Figure 5.23: Pressure and velocity contour levels for real 5-species gas model in equilibrium

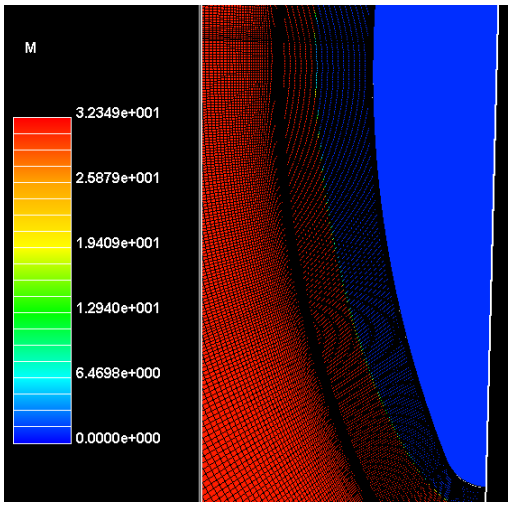

Figure 5.24: Mach number contours and check of the grid's suitability for this case

The temperature profile is presented in figure 5.25. It is clearly more accurate than the one calculated for the perfect gas case, as the maximum temperature value is 19289 K and on the edge of the shock layer. Due to the radiative and catalytic wall, the wall temperature stays low enough, less than 2500 K, a lot lower than the temperature of the shock layer. Figure 5.26 shows the 5 species mass-fractions along the stagnation line. The solution is correct, as the N_2 and O_2 species are consumed and the rest species are produced due to the reactions in the shock layer. Finally, the maximum Y+ value for this case is 1.18, which is still adequate.

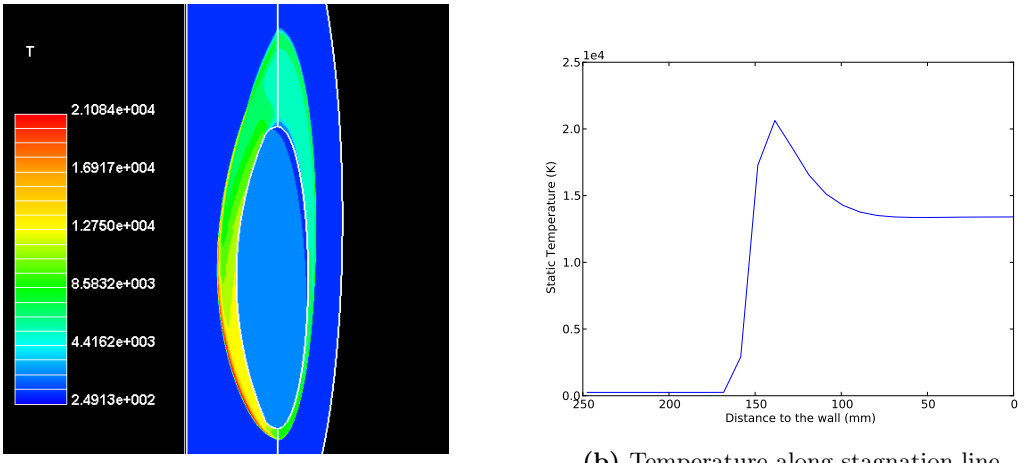

(a) Temperature field

(b) Temperature along stagnation line

Figure 5.25: Temperature field; 5 species equilibrium gas model

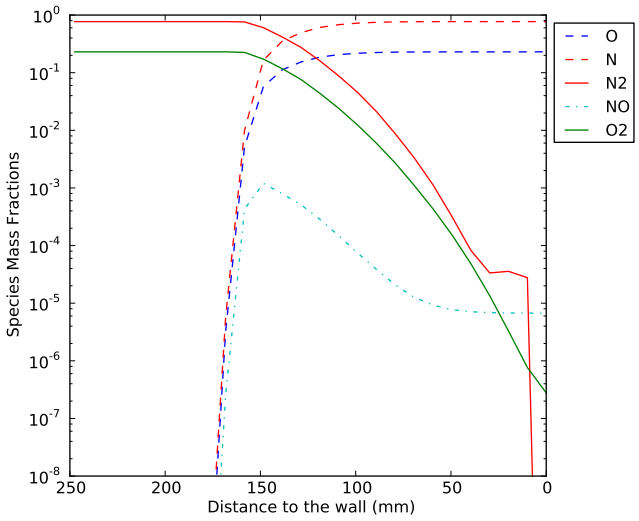

Figure 5.26: Species mass fractions; 5 species equilibrium model

5.3.1.3 Real 5-species non-equilibrium gas model

The same parameters as the previous case are set for this simulation. The gas state is now, however, considered to be non-equilibrium, and a non-equilibrium two-temperature model is implemented. The vibrational temperature is calculated along with the translational-rotational one.

This simulation was converged after 1000 iterations, as the residuals dropped to the order of 10^{-4} (figure 5.27).

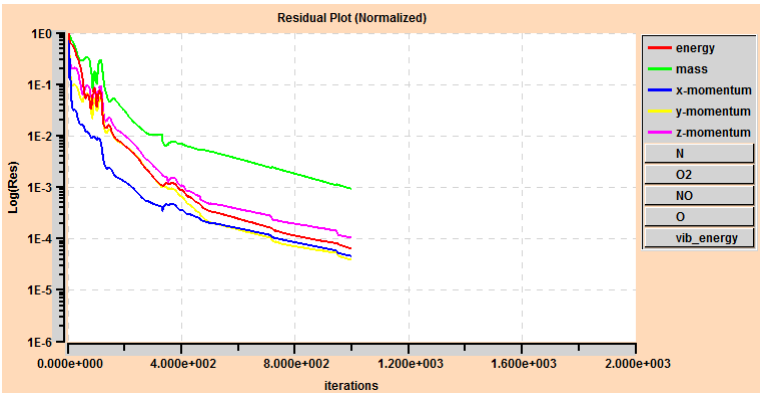

Figure 5.27: Convergence criteria for 5-species real gas model in non-equilibrium

From the pressure and velocity profiles along the stagnation line (5.28), the shock stand-off distance is observed to be 0.16 m, close to the equilibrium case. This is correct and expected, as no more species were included in the simulation.

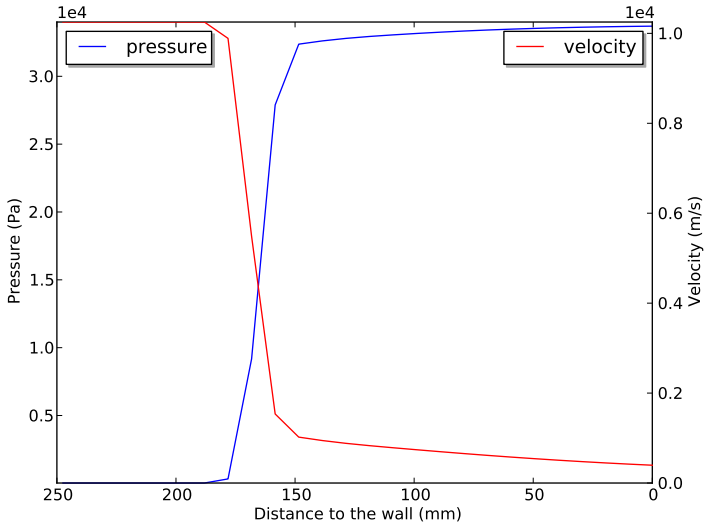

Figure 5.28: Pressure and velocity profile along stagnation line; real 5-species gas model in non-equilibrium

The temperature profiles can be seen in figure 5.29. The maximum value of the temperature is 22920 K, larger than the one of the equilibrium case. Due to the radiative and catalytic wall, the wall temperature stays low enough for this case as well. Correctly enough, the maximum value of the translational-rotational temperature is higher than the vibrational temperature maximum value, whereas they have very similar values in the rest shock layer.

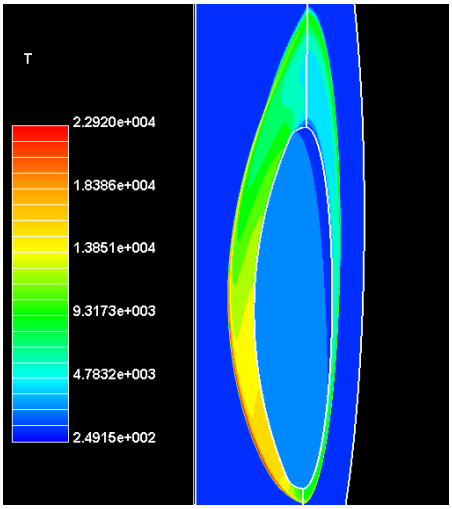

(a) Temperature field

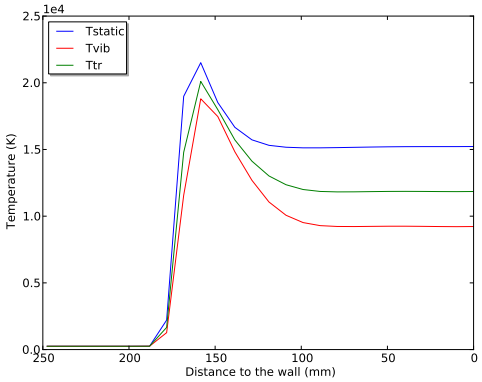

(b) Temperatures along stagnation line

Figure 5.29: Temperature field; 5 species non-equilibrium gas model

The profiles of the 5 species mass fractions in the shock layer are presented in figure 5.30. The maximum Y+ value for this case is 1.22, which means that the mesh should be a bit more refined on the wall. Finally, 5.31 shows the domain decomposition of the simulation domain and the CPU required for each section of the domain.

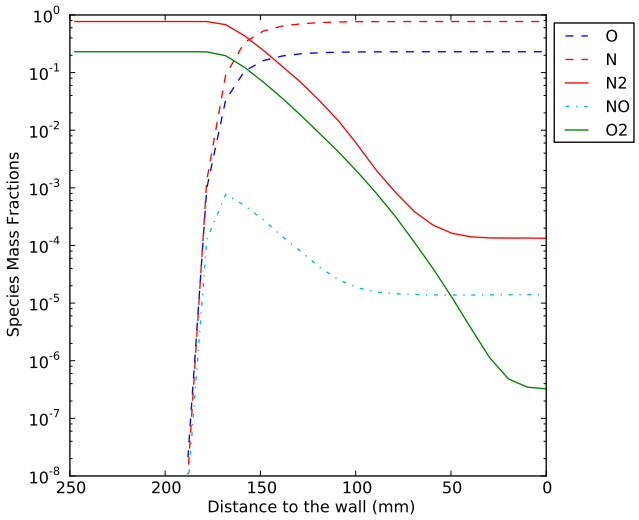

Figure 5.30: Species mass fractions; 5 species non-equilibrium model

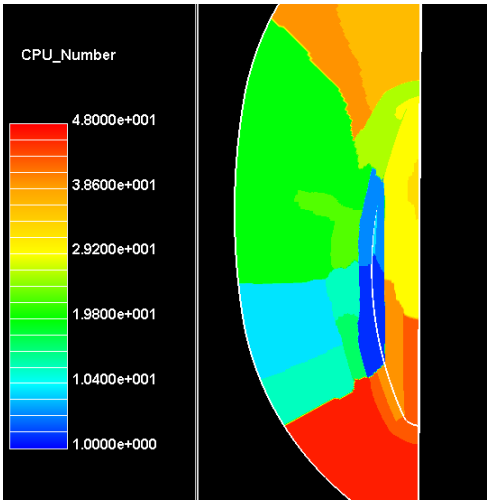

Figure 5.31: CPU Number required for the decomposed blocks of the domain

5.3.1.4 Real 11-species equilibrium gas model

This simulation was converged after 1000 iterations, as the residuals dropped to the order of 10^{-4}. The shock-standoff distance for this case is 0.13 m (see figure 5.32), smaller than the 5-species model case and the maximum temperature is 19289 K, smaller than the one for the 5 species equilibrium case, as the density of the shock layer is increased due to the existence of the more species. Figure 5.33 illustrates the velocity field in the shock layer, validating once again the quality of the results, as both the free-stream and the no-slip wall conditions are satisfied. Figure 5.34 illustrates the species mass fractions along the stagnation line for this case. Finally, the maximum value of Y+ is 1.18, as the 5 species equilibrium model.

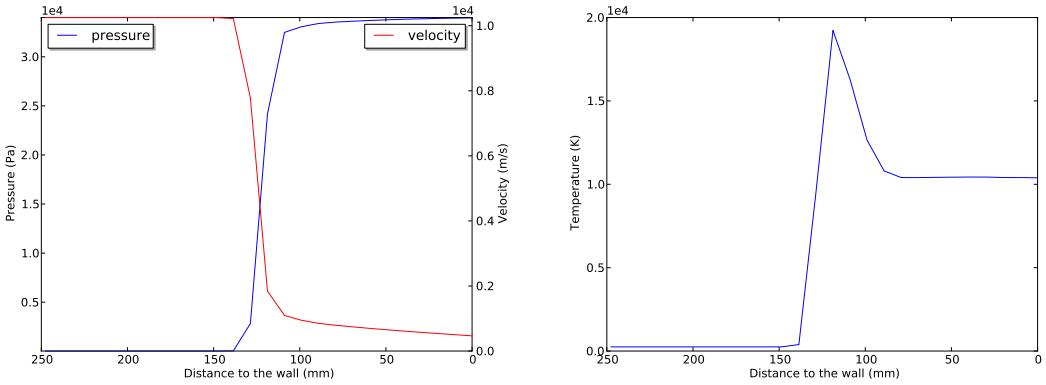

(a) Pressure and velocity **(b)** Temperature

Figure 5.32: Pressure and temperature field, 11-species equilibrium gas model

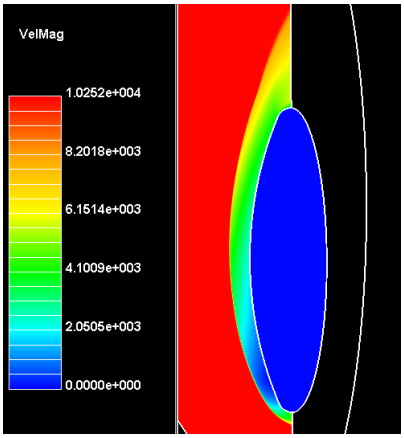

Figure 5.33: Velocity field; 11-species equilibrium gas model

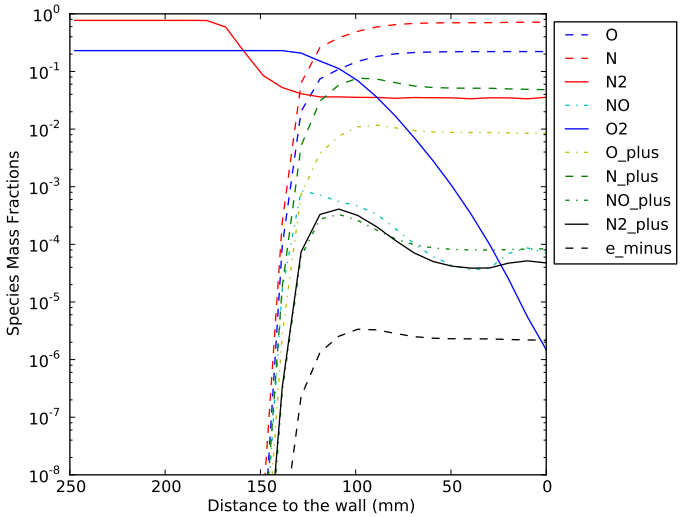

Figure 5.34: Species mass fractions; 11 species equilibrium model

5.3.1.5 Real 11-species non-equilibrium gas model

This simulation was converged after 1500 iterations, as the residuals dropped to the order of 10^{-4}(see figure 5.35. The shock-standoff distance for this case is 0.16 m, again larger than the corresponding equilibrium case, and the maximum temperature is 21976 K (see figure 5.36). The vibrational temperature is calculated to be smaller than the one calculated with the 5-species non-equilibrium model and is still smaller than the translational temperature. The rest of the figures present no important difference from the previous cases and therefore are overlooked in this section. The 11-species mass fraction profiles are presented in figure 5.37 and successfully depict the reactions taking place in the shock layer.For this model, the ionization reactions are taken into consideration as well. The maximum value of Y+ is 1.21.

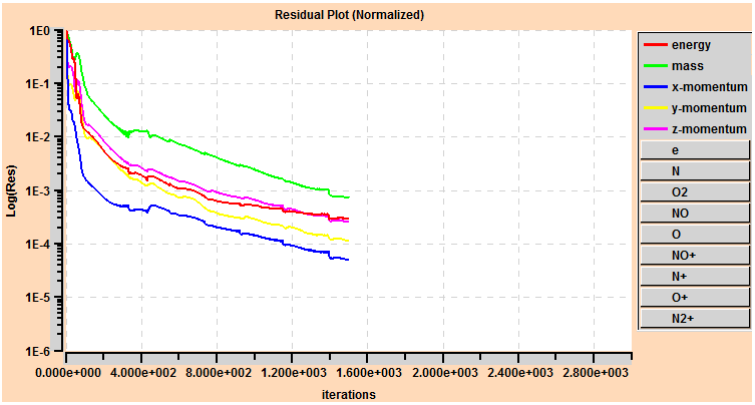

Figure 5.35: Convergence criteria for 11-species real non-equilibrium gas model

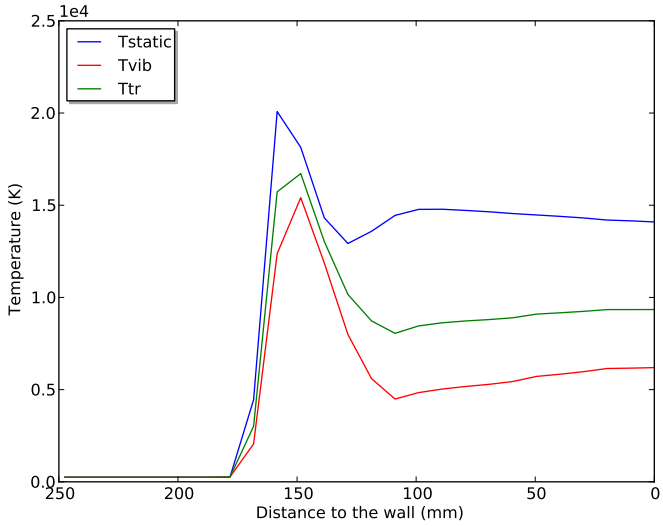

Figure 5.36: Translational and Vibrational temperature profiles along stagnation line, 11-species non-equilibrium gas model

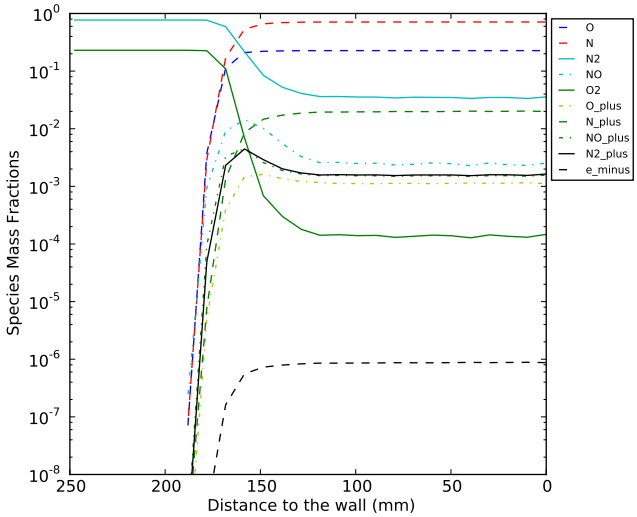

Figure 5.37: Species mass fractions; 11 species non-equilibrium model

Finally, for this case, a radiation calculation was performed in order to compare the spectra between the 2D and 3D simulations for the visocus case of a real 11-species gas model. The spectra was calculated only for the equilibrium region in the shock layer of the case and is depicted in figure 5.38. In comparison with figure 4.8, the VUV regime is the primary source of radiation for this case, whereas the peaks around the wavelength of 800 nm are considered irrelevant.

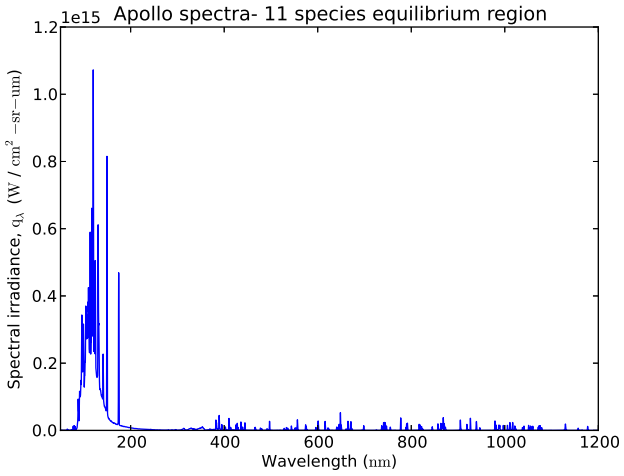

Figure 5.38: Spectral intensity, 11 species non-equilibrium gas model

5.3.1.6 Overview of CFD++ simulations results

The main results obtained by the CFD++ simulations are summarized, in table 5.3. The iterations presented are the ones required for each case to converge; the residuals to fall

to the order of 10^{-4}. d is the shock standoff distance for each case, T_{max} is the maximum temperature and $\dot{Q}_{max}$ is the maximum value of convective heat flux for each case.

Simulation case	Iterations	d [m]	$T_{max}[K]$	$Y+$	$\dot{Q}_{max}(W/m^2)$
Perfect gas	1000	0.5	57854	0.18	
Real 5-species equilibrium	630	0.15	21084	1.19	$4.63 \cdot 10^6$
Real 5-species non-equilibrium	1000	0.16	22920	1.22	$4.57 \cdot 10^6$
Real 11-species equilibrium	1300	0.13	19289	1.18	$4.68 \cdot 10^6$
Real 11-species non-equilibrium	1500	0.16	19289	1.18	$4.64 \cdot 10^6$

Table 5.3: Summary of the basic results from the CFD++ simulations

Figure 5.39 compares the temperature profiles along the stagnation line for each gas model. It is worth noticing that the shock standoff distance of the non-equilibrium gas models is the same. Figure 5.40 compares the heat-fluxes profiles along the boundary wall surface of the capsule for the 4 investigated gas models. It is obvious that as the number of species increases, the heat flux values on the surface decrease. The non-equilibrium cases calculate the same heat flux profile on the surface.

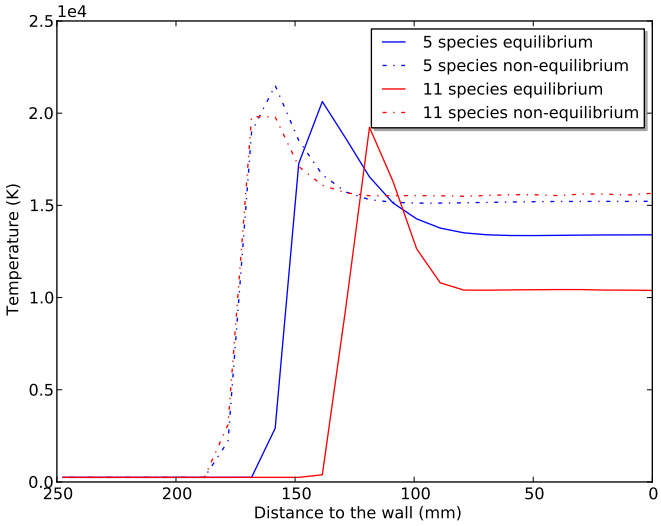

Figure 5.39: Temperature profile along stagnation line for different gas models

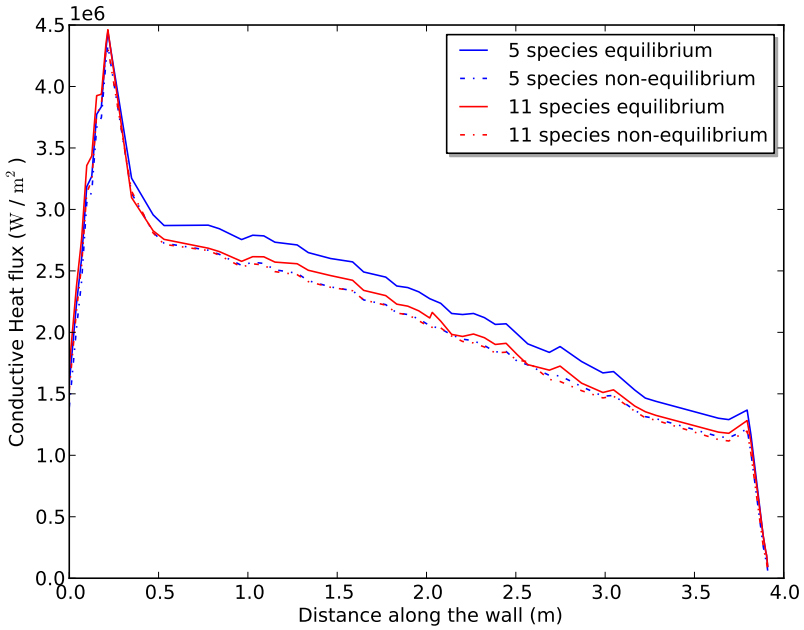

Figure 5.40: Heat flux profile along wall surface for different gas models

Finally, for the non-equilibrium 11-species gas model case, the convective heat flux on the surface has been calculated and is illustrated in figure 5.41. From a comparison between the 3D results obtained with CFD++ with the 2D results obtained with Eilmer3 for the viscous without ablation cases (only the 11 atmospheric species), using the Ramshaw-Chang diffusion model, the maximum value of the convective heat flux is similar between the two cases for the peak heating point is calculated as shown in table 5.4:

	2D Eilmer3	3D CFD++
Peak convective heating value (W/m^2)	$4.0577 \cdot 10^6$	$4.6434 \cdot 10^6$

Table 5.4: Peak convective heating values calculated for 2D and 3D calculations on the stagnation point

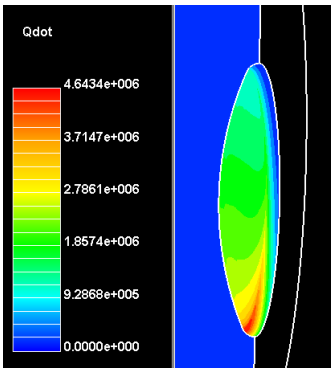

Figure 5.41: Heat flux on the wall, 11-species model

5.3.2 NSMB Simulations

The following section presents the main results obtained for a real 5-species gas model, in equilibrium, non-equilibrium and thermal-non-equilibrium gas state. The radiation field is also calculated with the use of the NSMB output file. The simulation results are compared to each other.

The inflow parameters used for each simulation case are presented in the following table:

Density $[kg/m^3]$	Mach	Velocity $[km/s]$	Temperature $[K]$	Pressure $[Pa]$
$3.41 \cdot 10^{-4}$	30	10.252	249.16	24.39

The solution strategy that was applied for these calculations is the following: At first, calculations with smaller Mach number (=25) and no angle of attack were performed and converged. Then, these solutions were used to perform the calculations with the actual inflow parameters. It was a way to gradually ramp up the difficulty and, therefore, accelerate the convergence of the cases. In the input file, the wall temperature was set to 2500 K, which is the wall temperature that corresponds to the flight data for the second trajectory point and the emissivity of the wall was set to 0.8.

5.3.2.1 Equilibrium gas model

The main results for the real equilibrium gas case are presented in this section for the converged solution after 3000 iterations. Figure 5.42 presents the pressure and temperature fields. The maximum temperature values for this case are: $T_{max,shock} = 8.0 \cdot 10^3$ and $T_{max,wall} = 3.76 \cdot 10^3$.

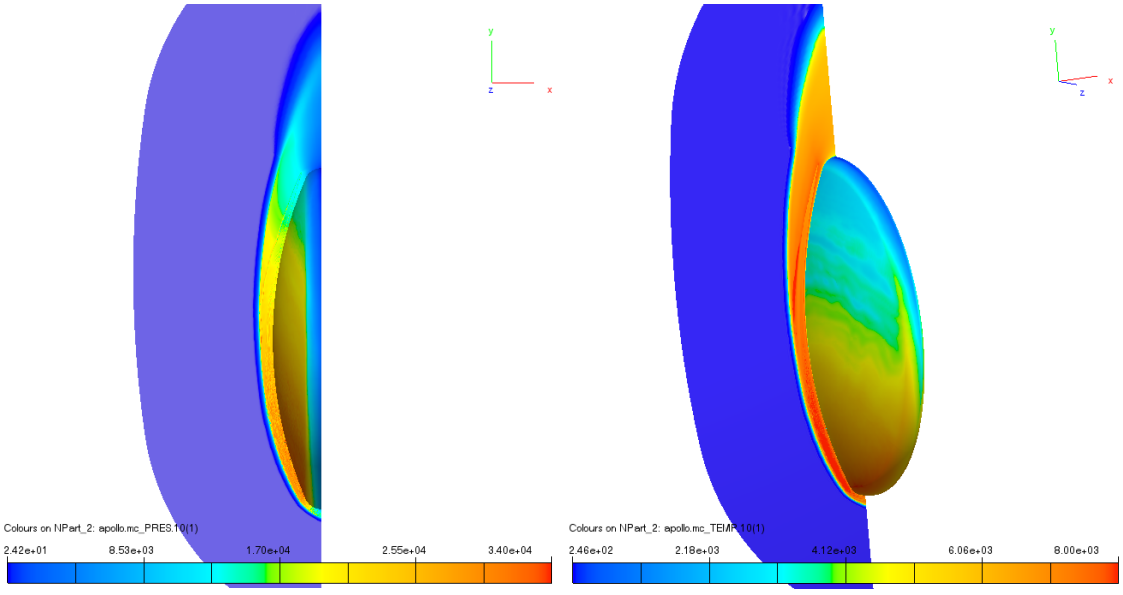

(a) Pressure field (Pa) **(b)** Temperature field (K)

Figure 5.42: Pressure and temperature field, 5-species equilibrium gas model

The velocity field applied to the flow domain is presented in figure 5.43. The first obser-

vation of the velocity field is the value of the shock standoff distance, D = 0.22 m, which is similar to the one calculated with the use of CFD++. From the u velocity graph, it is evident that the velocity on the wall tends to zero, thus, the no-slip wall condition is satisfied.

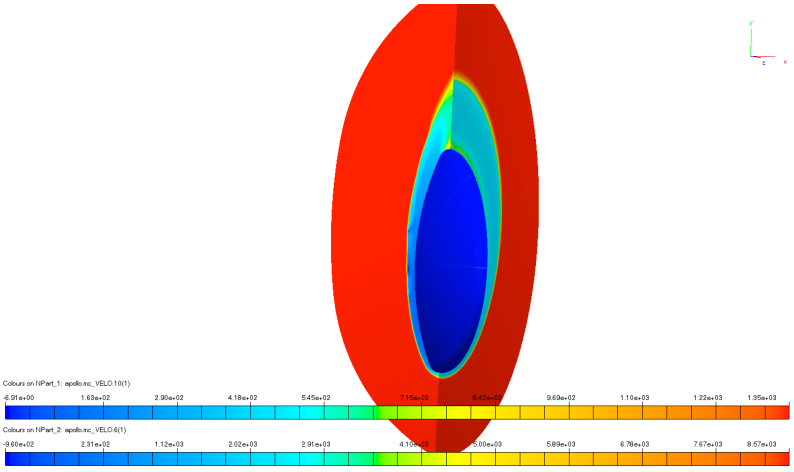

(a) Velocity u (m/s^2)

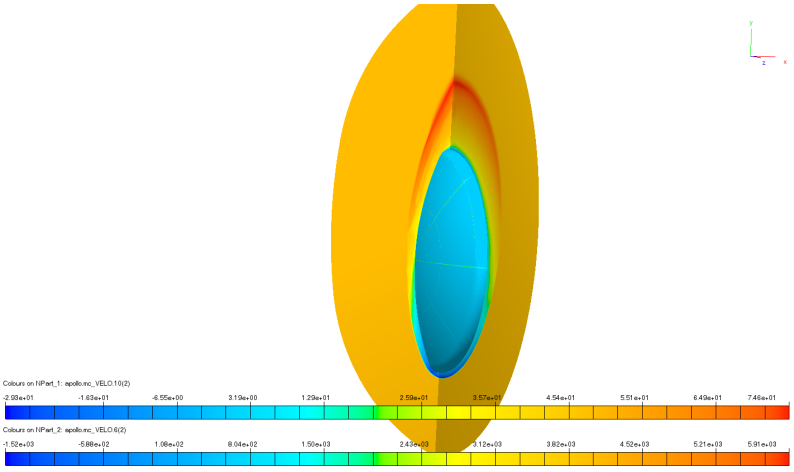

(b) Velocity v (m/s^2)

Figure 5.43: Velocity field, 5-species gas model in equilibrium

The 5-species mass fractions are presented in figure 5.44 and successfully summarize the processes of dissociation and exchange reactions in the shock layer.

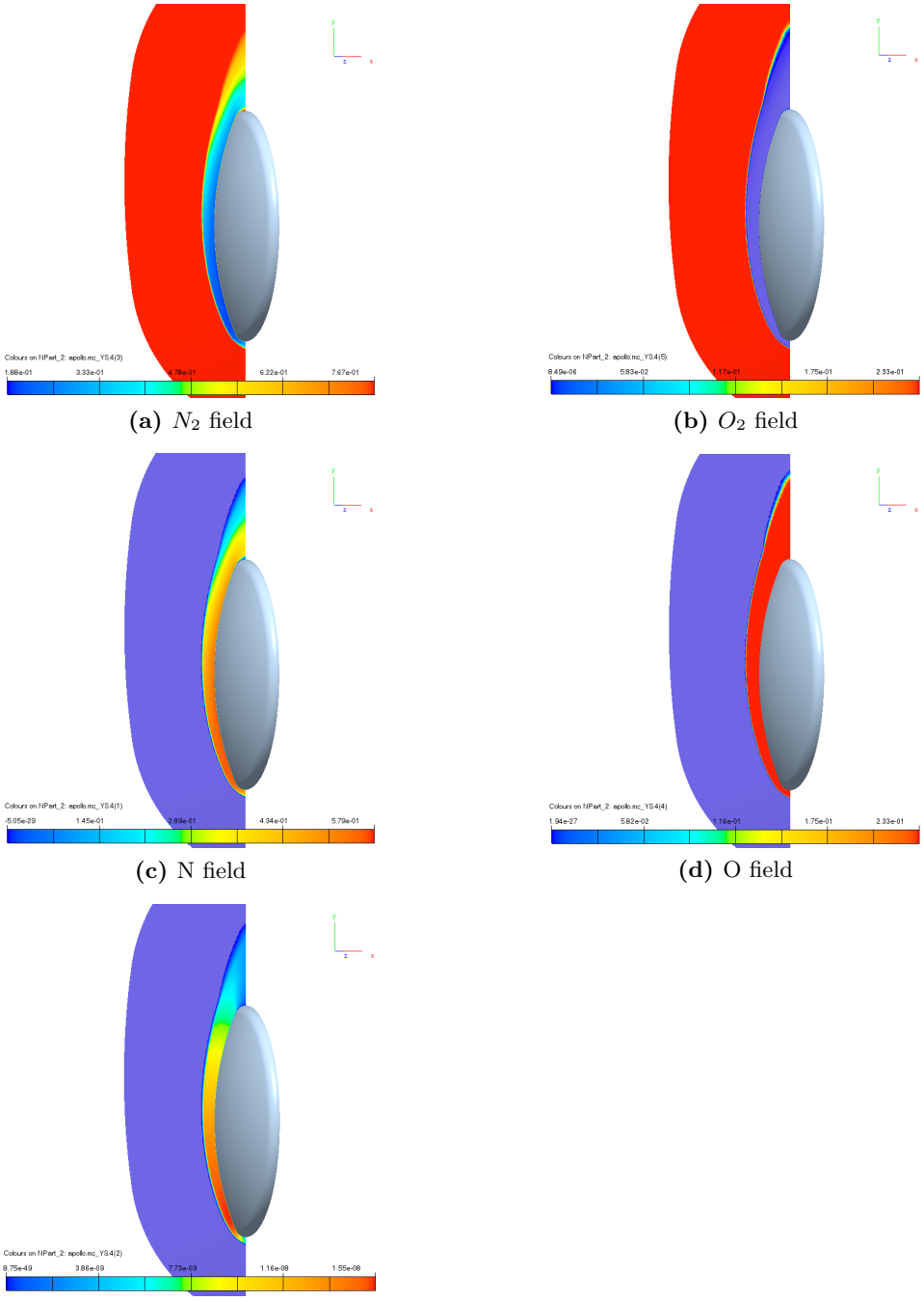

(a) N_2 field

(b) O_2 field

(c) N field

(d) O field

(e) NO field

Figure 5.44: Species distributions, 5-species equilibrium gas model case

5.3.2.2 Chemical non-equilibrium gas model

The converged results after 3500 iterations for the real non-equilibrium gas case are presented in this section. Figure 5.45 presents the pressure and density field. The convergence of this solution is evident from the pressure and density streamlines along the surface of Apollo 4. The velocity and Mach number field applied to the flow domain are presented in figure 5.47and figure 5.46 respectively. The shock standoff distance for this case is D

= 0.25 m. Exactly as the previous case, the velocity on the wall tends to zero, thus, the no-slip wall condition is satisfied.

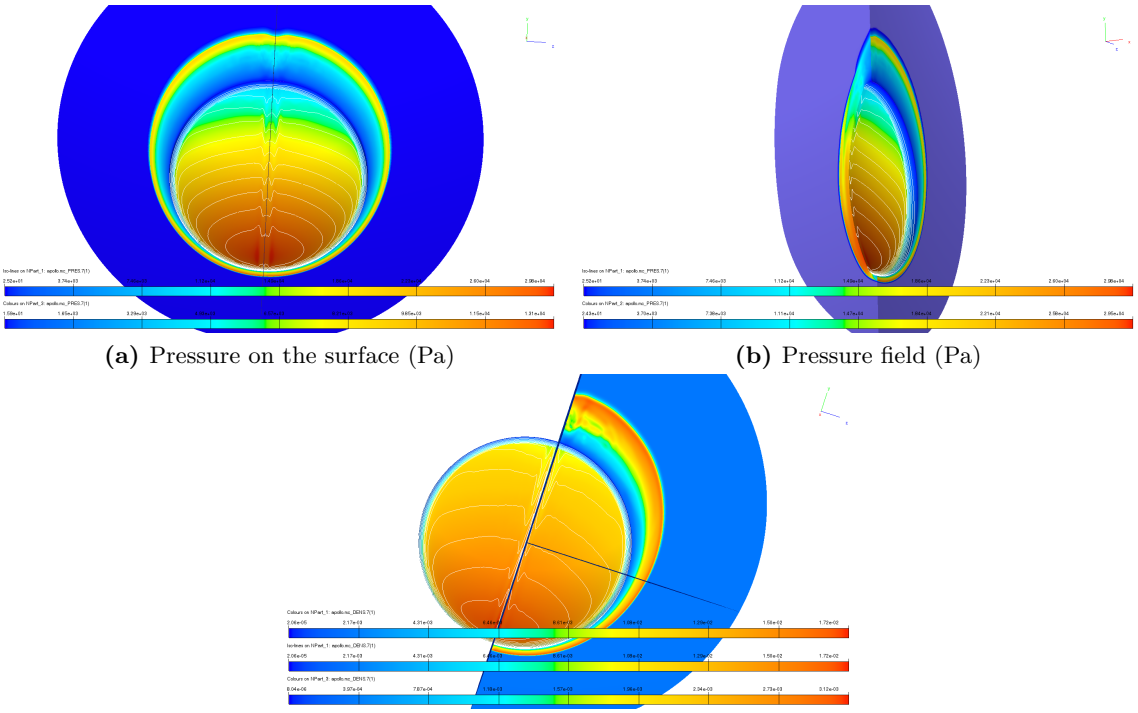

(a) Pressure on the surface (Pa)

(b) Pressure field (Pa)

(c) Density field (Pa)

Figure 5.45: Pressure and density field, 5-species non-equilibrium gas model

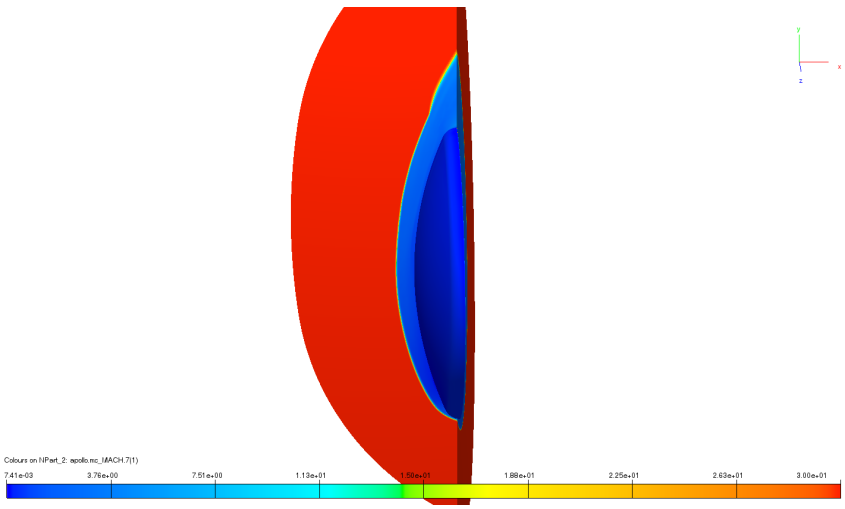

Figure 5.46: Mach Number field, 5-species non-equilibrium gas model

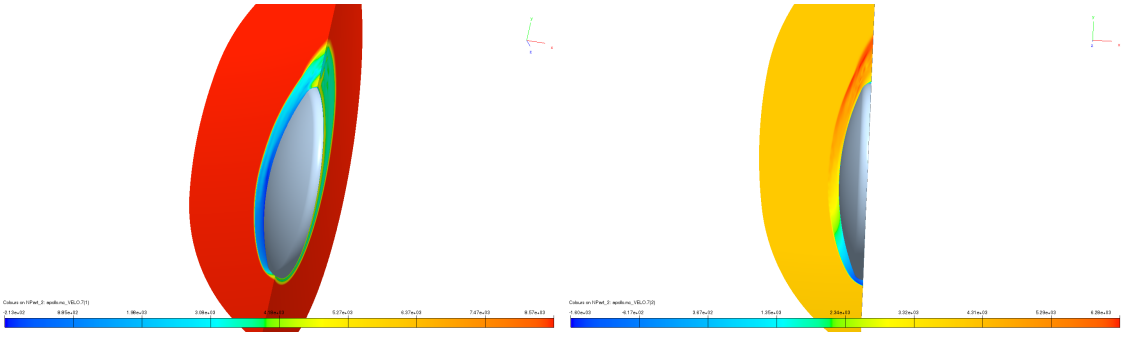

(a) Velocity u (m/s^2) **(b)** Velocity v (m/s^2)

Figure 5.47: Velocity field, 5-species non-equilibrium gas model

The temperature field is applied in figure 5.48. The value of the temperature on the wall boundary is again smaller than the temperature in the shock layer: $T_{max,shock} = 1.64 \cdot 10^4$ and $T_{max,wall} = 2.89 \cdot 10^3$, as indicated by the wall boundary condition of temperature.

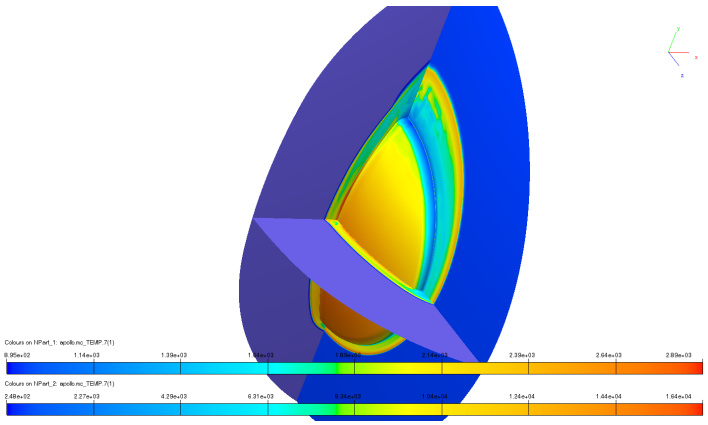

Figure 5.48: Temperature field, 5-species non-equilibrium gas model

The 5-species mass fractions are presented in figure 5.49 and successfully summarize the processes of dissociation and exchange reactions in the shock layer.

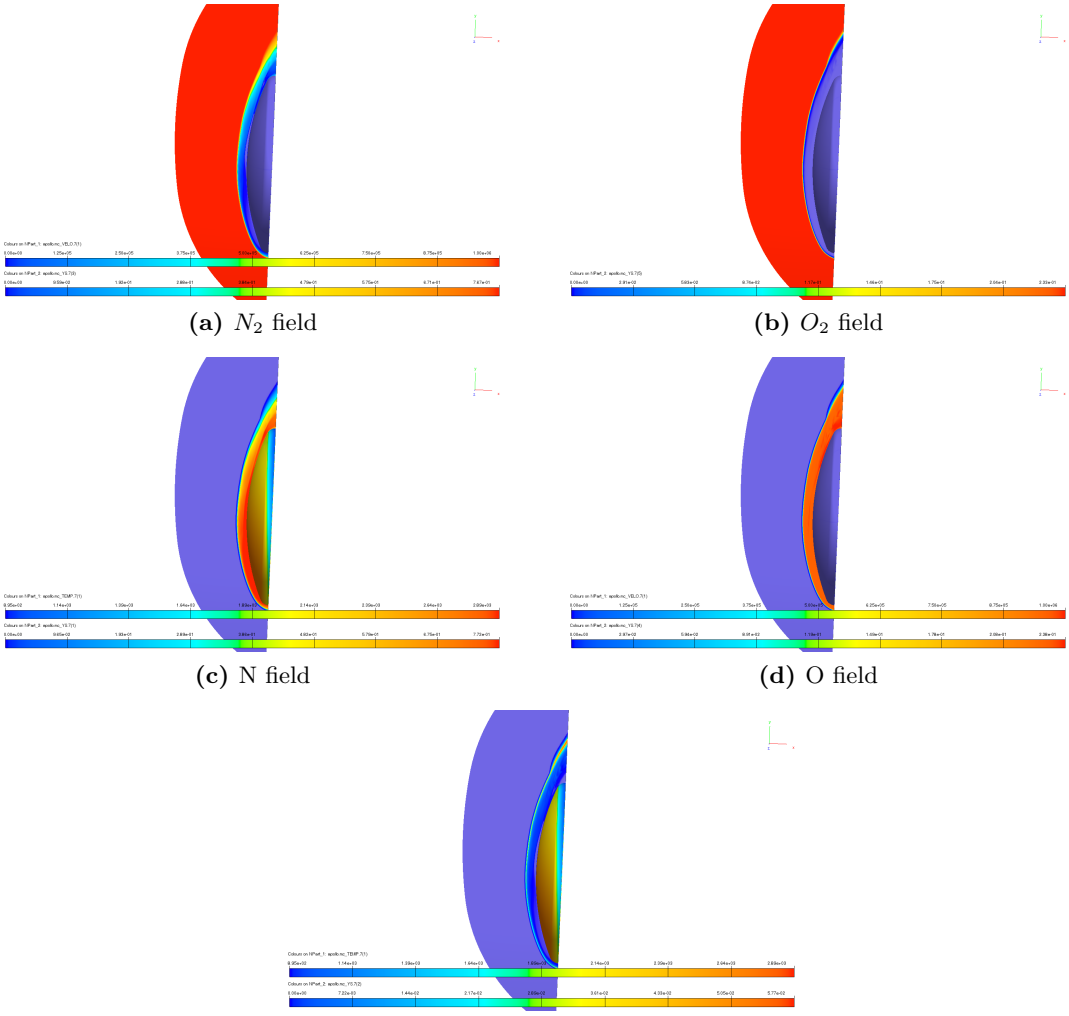

(a) N_2 field

(b) O_2 field

(c) N field

(d) O field

(e) NO field

Figure 5.49: Species distributions, 5-species non-equilibrium gas model case

5.3.2.3 Thermal and chemical non-equilibrium gas model

Regarding the thermal-non equilibrium case, the presented results are the ones achieved after 4000 iterations, with the energy equation's residuals to drop to the order of 10^{-3}. From the pressure field for the case, it is obvious that the pressure values are almost identical to the ones of the previous case (see figure 5.50. From the density streamlines on the surface of the capsule in the same figure it is evident that the quality of the results is not sufficient.

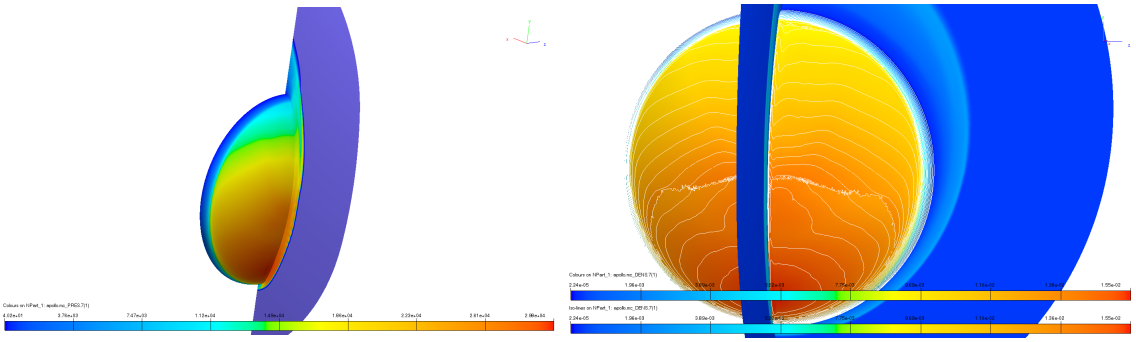

(a) Pressure field (Pa) **(b)** Density field (Pa)

Figure 5.50: Pressure and density field, 5-species thermal non-equilibrium gas model

In reality, the only result that differentiates this case from the chemical non-equilibrium case of the previous section is the change of the temperature values, when inserting the conservation equation of the vibrational energy. More specifically (see 5.51), the maximum value of the temperature of the field ascends to $T_{shock,max} = 2.46 \cdot 10^4$ and the vibrational temperature in the shock layer reaches the value of $T_{vib,max} = 4.02 \cdot 10^4$. The calculated value of the vibrational temperature is considered to be totally exaggerating. This will be investigated in the following section.

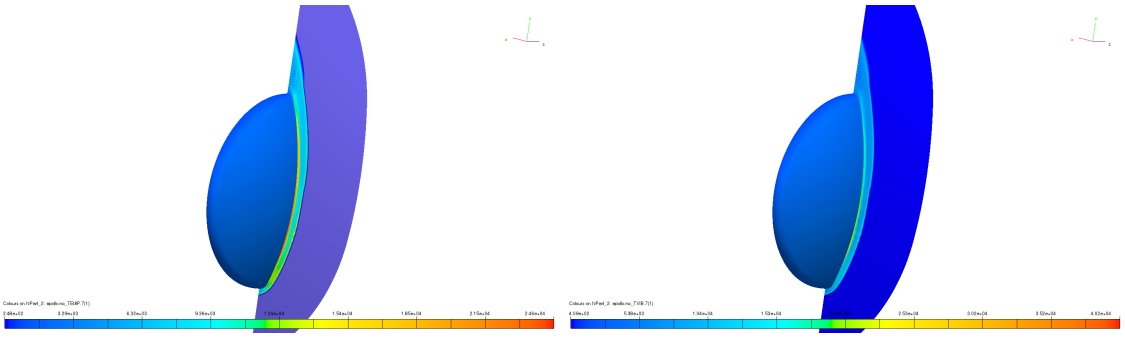

(a) Static temperature (K) **(b)** Vibrational temperature (K)

Figure 5.51: Temperature field, 5-species gas model in thermal and chemical non-equilibrium

5.3.2.4 Overview of the NSMB simulations

In this section the main results obtained by the NSMB simulations are summarized, in table 5.5. It is noticed that all the cases made use of the 5-species gas model by Park (ref.Park). The five species implemented are : N_2, O_2, NO, N, O.

Simulation case	Iterations	Standoff [m]	T_{max} [K]
Equilibrium	2000	0.2	8000
Chemical non-equilibrium	3500	0.19	16400
Thermal, Chemical non-equilibrium	3500	0.18	24600

Table 5.5: Summary of the basic results from the NSMB simulations for the front body

From the presented results, it is observed that the values of the temperature in the flow-field change in an exaggerating way, depending on the thermo-chemical state of the flow, which should not be happening. Therefore, this is commented out as an issue of the code itself to be addressed.

5.3.3 Comparison of the two solvers

The following section compares the two solvers used for the 3D simulations for one case of the front body of Apollo 4. The selected case is the one set for two cases: the real gas 5-species euilibrium and chemical-thermal non-equilibrium models. The solvers are compared according to their sensitivity to grid quality, computational time and accuracy of results.

The comparative results of the two codes are summarized in table 5.6

	CFD++	NSMB
Equilibrium model		
Order of convergence achieved	10^{-4}	10^{-2}
Iterations to convergence	630	2000
Computational time (s)	5229	4950
Max. pressure value (Pa)	$3.4047 \cdot 10^4$	$3.4 \cdot 10^4$
Max temperature value (K)	$2.1084 \cdot 10^4$	$8.0 \cdot 10^3$
Number of grid-cells	$7 \cdot 10^6$	$2 \cdot 10^6$
Non-Equilibrium model		
Order of convergence achieved	10^{-4}	10^{-2}
Iterations to convergence	1000	2500
Computational time (s)	11625	8222
Max. pressure value (Pa)	$3.3932 \cdot 10^4$	$3.38 \cdot 10^4$
Max temperature value (K)	$2.292 \cdot 10^4$	$2.46 \cdot 10^4$
Number of grid-cells	$7 \cdot 10^6$	$2 \cdot 10^6$

Table 5.6: Comparison criteria of the two solvers for the 5-species equilibrium and chemical and thermal non-equilibrium models, Apollo 4 front body case

From the above comparative results, it is obvious that both the solvers presented similar

results for the thermal- chemical non-equilibrium case, which validates the qualitative results of the two solvers.

General Comments on the two solvers

NSMB

Regarding the NSMB solver, the code presented an incapability to successfully handle cases with the high flow transients, such as the cases with Mach-numbers greater or equal to 30. More specifically, with the same mesh (number of cells = $2 \cdot 10^6$), the 5-species equilibrium case was run for a Mach number equal to 25, as well as for a Mach number equal to 30. In both cases, an angle of attack was introduced to the flow. The residual graphs for both the cases are presented in figure 5.52. With reference to the residuals graph and figure 5.53, the better convergence and quality of the results of the case with M=25 is undeniable. It is worth mentioning that the same case of M=30 was ran with a finer mesh (number of cells = $7 \cdot 10^6$) as well, but the quality of the results was not better.

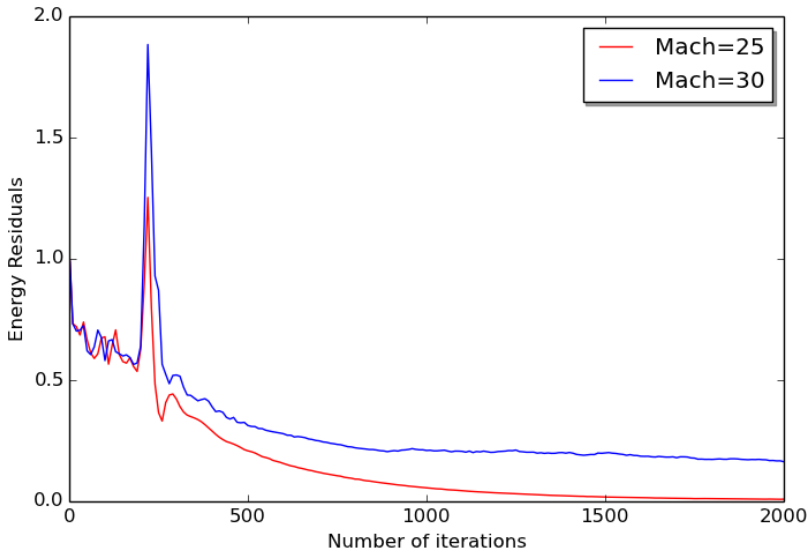

Figure 5.52: Comparison of the residuals graphs for two NSMB cases with different Mach numbers

.

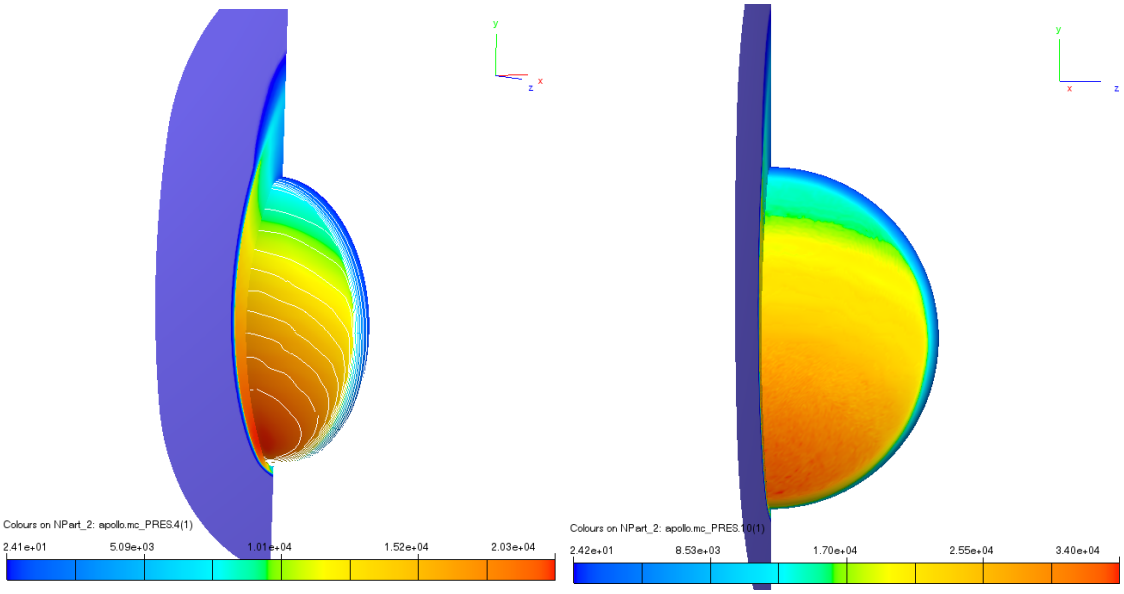

(a) Mach = 25 **(b)** Mach = 30

Figure 5.53: Pressure field, 5-species gas model in equilibrium for different Mach-number cases

CFD++

Regarding the CFD++ solver, the code itself seems to need a really refined mesh, especially close to and on the surface. Its highly advanced heat-transfer calculator requires the values of the cell-Reynolds number to be kept low enough for cases with Radiative Heat transfer wall Boundary Conditions and high Mach numbers. Indicatively, the cell Reynolds number should be kept close to unit. This leads to big-in-size and very refined meshes for such cases.

Finally, the non-equilibrium cases in CFD++ are a lot more sensitive than the equilibrium ones. This sometimes leads to the solver not being able to cope with such cases so well when they are run in steady state mode. The user should be ready to set such cases up as quasi-steady-state cases, selecting the transient time intergation mode, but applying a larger time step than would normally be used in a transient simulation. For instance, the 11-species non-equilibrium case was run both as a steady-state and as a quasi-steady-state simulation case. The residuals of both simulations are presented in figure 5.54. It is obvious that the quasi-steady-state case led to smoother results, which were finally used.

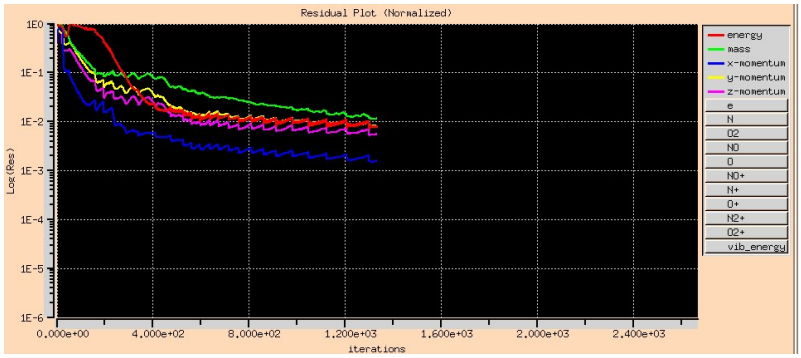

(a) Steady-state time integration scheme

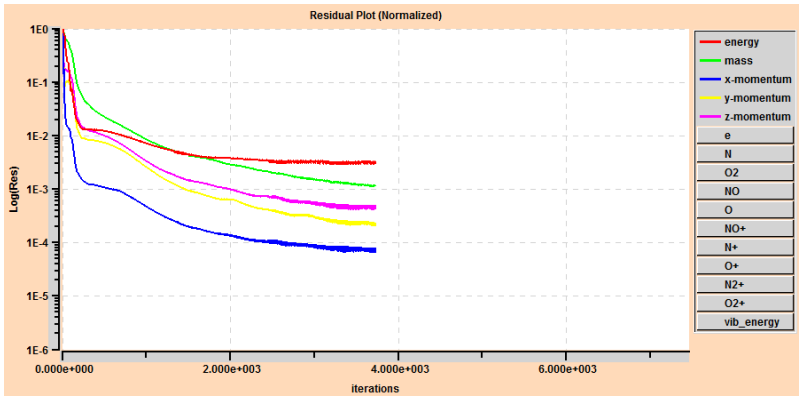

(b) Transient time integration scheme

Figure 5.54: Residuals for two time integration modes for the non-equilibrium cases in CFD++

5.4 Whole Body Simulations

The simulations for the Whole body of the Apollo Command Module were performed only with the use of the NSMB solver, because of the computational expense of the CFD++ solver. The following sections present the main results for the equilibrium, chemical non-equilibrium and thermal-chemical non-equilibrium cases for a real 5-species gas model.

5.4.1 Equilibrium gas model

The converged results after 3000 iterations for the real non-equilibrium gas case are presented in this section. The energy residuals for this number of iterations dropped to the order of 10^{-2}. Figure 5.55 presents the pressure and density field. In the same figure, the streamlines of the case are depicted. The velocity and Mach number field applied to the flow domain are presented in figure 5.56. It is obvious from the velocity field that the no-slip condition is satisfied.

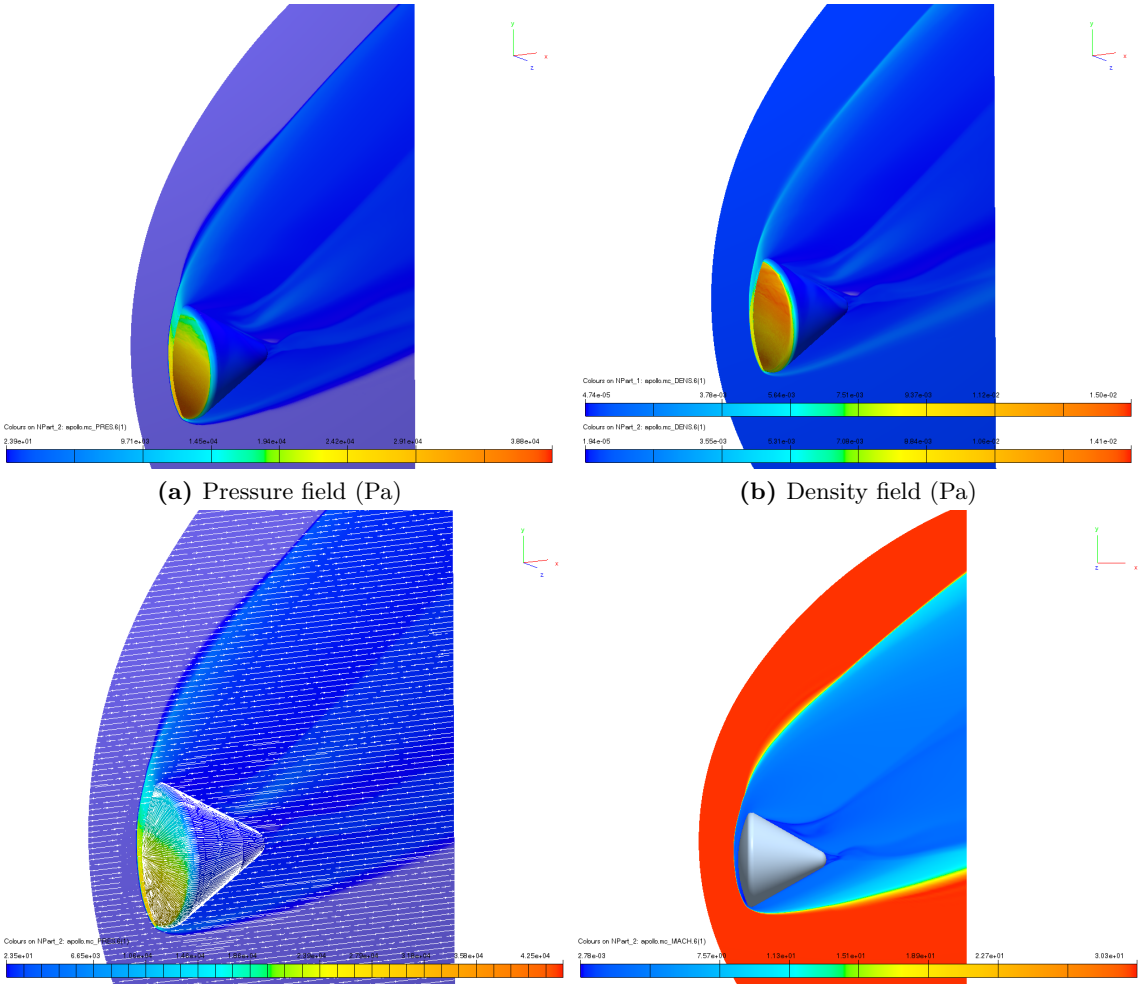

(a) Pressure field (Pa)

(b) Density field (Pa)

(c) Flow-field streamlines

(d) Mach Number

Figure 5.55: Pressure, density and Mach-number field, real equilibrium gas model

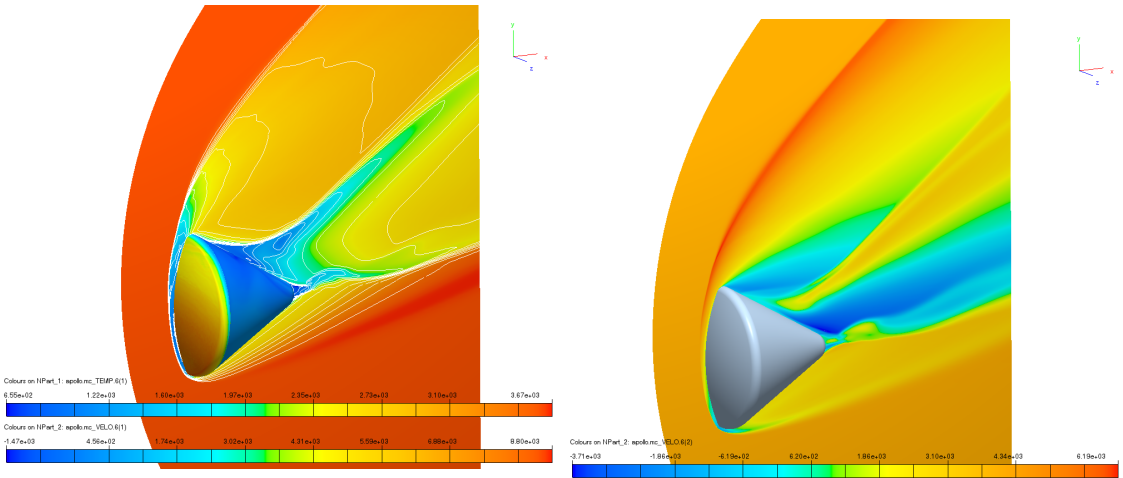

(a) Velocity u (m/s^2) in the field, Temperature in the body surface

(b) Velocity v (m/s^2)

Figure 5.56: Velocity field, real equilibrium gas model

The temperature field is applied in figure 5.57. The value of the temperature on the wall boundary and in the shock layer: $T_{max,shock} = 8.0 \cdot 10^3$ and $T_{max,wall} = 3.67 \cdot 10^3$ match the values calculated for the front body equilibrium case.

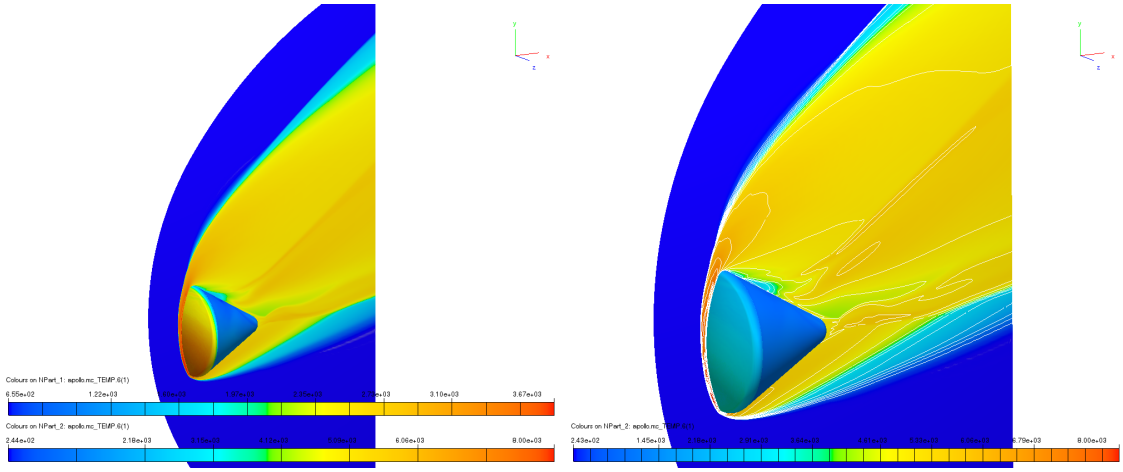

(a) Temperature field **(b)** Temperature isolines

Figure 5.57: Temperature field, 5-species equilibrium gas model

The 5-species mass fractions are presented in figure 5.58 and successfully summarize the processes of dissociation and exchange reactions in the shock layer and in the back flow of the Apollo 4 body. Specifically, as the temperature is still high enough, exchange reactions are mostly important in this part of the flow, as the inflow O_2 has been consumed due to the front-body shock layer dissociation reactions. N_2, on the other hand is reformed in the back-flow, due to back rate reactions.

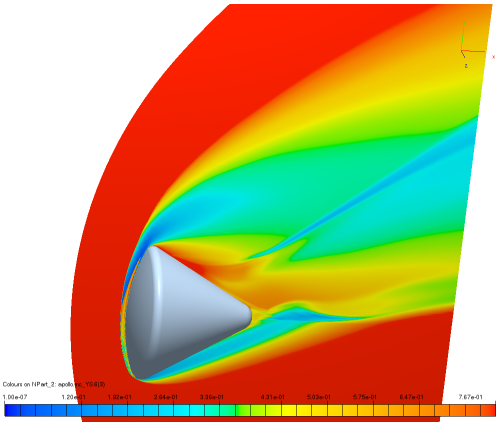

(a) N_2 field

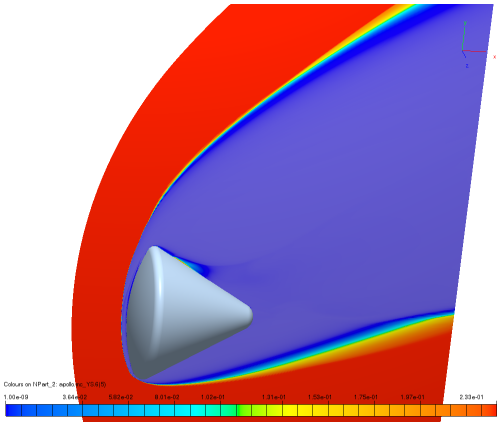

(b) O_2 field

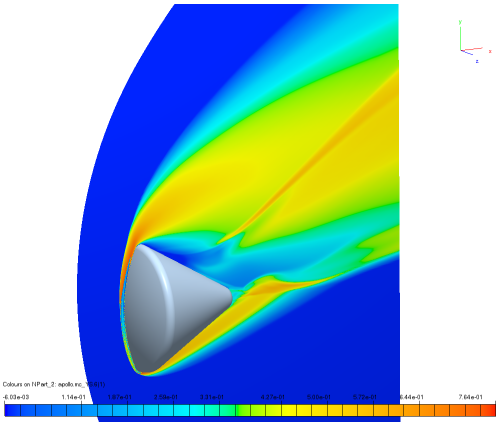

(c) N field

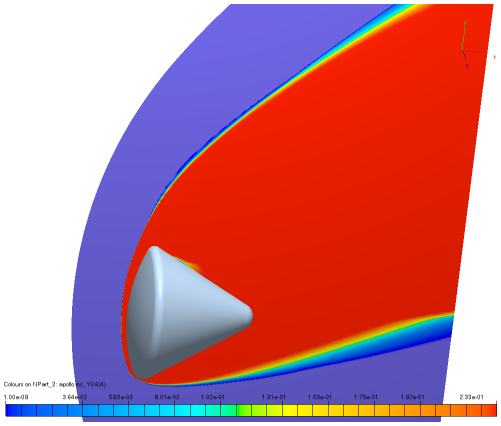

(d) O field

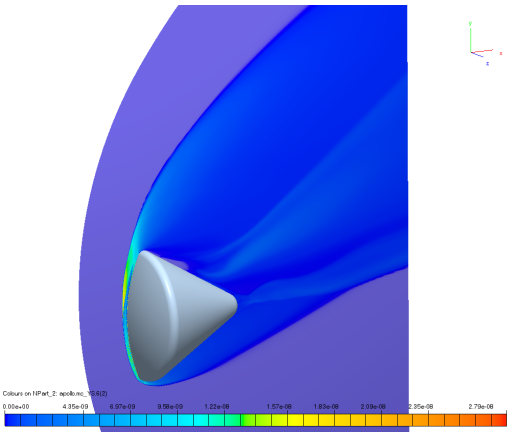

(e) NO field

Figure 5.58: Species distributions, 5-species equilibrium gas model case

5.4.2 Thermal Non-Equilibrium gas model

The converged results after 3500 iterations for the real non-equilibrium gas case are presented in this section. The energy residuals for this number of iterations dropped to the order of 10^{-1}. Figure 5.59 presents the pressure, density and mach number field.

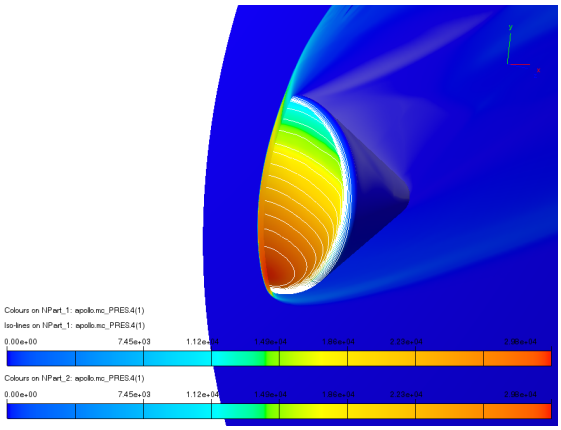

(a) Pressure field (Pa)

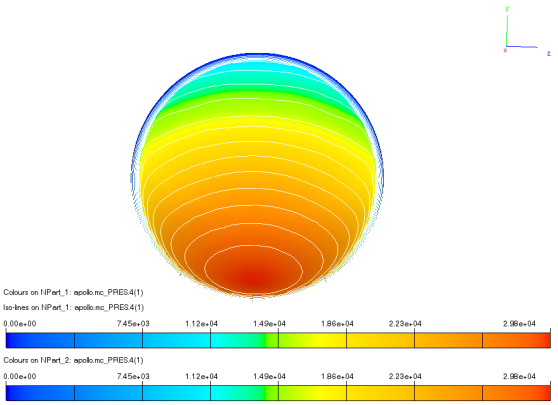

(b) Pressure isolines (Pa)

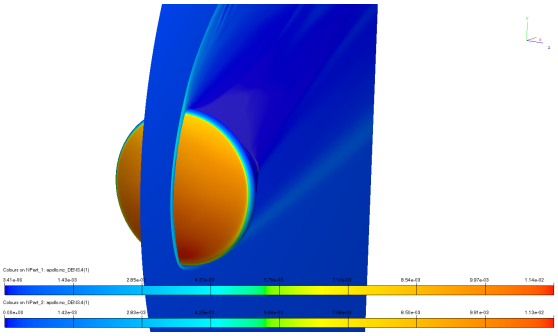

(c) Density field (Pa)

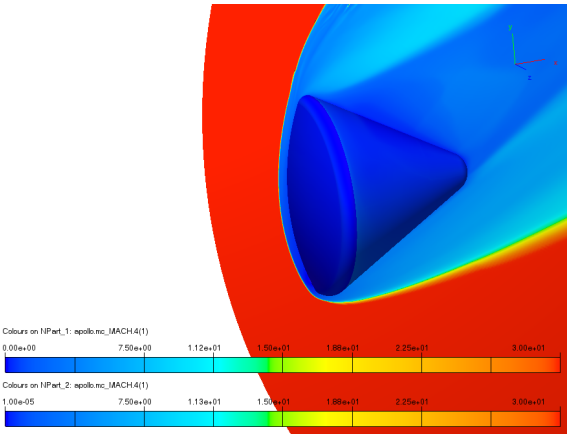

(d) Mach Number

Figure 5.59: Pressure, density and Mach-number field, real equilibrium gas model

The maximum value of the temperature $T_{max,shock} = 2.73 \cdot 10^4$ does not entirely match the one calculated for the front-body case. The maximum value of the vibrational temperature is calculated equal to $T_{max,vib} = 3.51 \cdot 10^4$, which is extremely large and not considered correct.

Part IV

Conclusion

Chapter 6

Conclusions and Recommendations

This chapters discusses the main results of the present work and concludes to recommendations for future work related to the present one.

6.1 Conclusions

This work was a part of the ARC (Ablation-Radiation Coupling) project, aiming to numerical simulate the ablation-flow-field and radiation-flow-field coupling for certain points of the Apollo Command Module reentry trajectory. The thesis is divided into two parts. The first part contains the two-dimensional simulation analysis for the front body of the Apollo Command Module. These simulation cases were run with the use of an equivalent sphere radius, implementing the Eilmer3 Compressible Flow solver, a code developed by the University of Queensland, Australia. Simulations for the viscous cases, with and without ablation effects, were performed with the use of two different diffusion models, the Constant-Lewis-Number and the binary Ramshaw-Chang model. Furthermore, the radiation field was calculated with the viscous and the ablative cases as initial solutions, using two different Radiation transport models, the tangent slab and the ray-tracing Monte-Carlo method. The main results obtained from this set of simulations are summarized below:

- Comparisons were made between the different simulation cases, including inviscid, viscous ablation and non-ablation cases, implementing two different diffusion models for one trajectory point. The discussed results proved that the Ramshaw-Chang model was more suitable for the diffusion calculations than the Constant-Lewis number and that the Monte Carlo ray-tracing method was a lot unstable compared to the tangent slab radiation transport model.

- Comparisons were made between the three trajectory points, resulting in the fact that the second trajectory point is the peak radiative heating point, whereas the third point is the peak convective heating point. The results were finally compared to certain correlations and flight data, proving good agreement with them. This was a way of validating the code's accuracy and results' quality.

The second part of the thesis contains the three-dimensional simulation analysis for the fore-body of Apollo 4 using two different solvers and for the whole body of Apollo 4 using the one of the two. The simulations were performed in order to compare the different gas models implemented, from a perfect gas to a real gas of 5 and 11 species in equilibrium or non-equilibrium. Furthermore, the two solvers were compared by means of the speed of the calculations and the quality of the results. The main results obtained are summarized below:

- The CFD++ solver was used to compare different gas models. The simulation cases performed include the cases of the following gas models: perfect gas, real gas 5-species, equilibrium and non-equilibrium, real gas 11-species, equilibrium and non-equilibrium. For all the cases the flow was considered viscous. The comparison of the results of the mentioned cases showed the good agreement of the cases with the 2D simulation results, both for flow-field parameters and heat-fluxes. Moreover, the spectral intensity was calculated in the equilibrium region of the shock layer in front of the Apollo4 capsule. The comparison with the spectra obtained from the 2D calculation proves the good agreement between the 2D and 3D cases.
- The NSMB solver was used to simulate the equilibrium, chemical non-equilibrium and chemical and thermal non-equilibrium cases for the 5 species real gas model. The comparison of the results of the two solvers proved the simulations performed with NSMB to be accurate and faster than the ones performed with CFD++. Therefore, the whole body simulations were performed with the NSMB solver.
- The results from the whole body simulations present a wider image of the flow- and the thermal field around the entire capsule body. It is worth mentioning that the values of all the parameters calculated on the front-body surface were in full agreement with the front-body cases.

6.2 Recommendations

The present work studied the flow-field and the thermal field of the Apollo 4 vehicle during the atmospheric reentry both in 2D and 3D. Recommendations for future work apply for both the 2D and 3D cases.

Regarding the 2D simulations, applying the Eilmer3 solver, a fully-coupled investigation of the flow-field and the ablation and radiation field is highly recommended, in order to

investigate differences in the results because of the strong coupling and agreement with the flight data. Moreover, it is crucial the entire set of calculations to be performed again, this time using the actual geometry of the Apollo 4 capsule,thus simulating the domain not as an axisymmetric one, in order the choice of the equivalent sphere radius to be evaluated.

On the other hand, the 3D simulations should be performed for the whole Apollo 4 body, both in CFD++ and NSMB, implementing the 11 species model, in order for more accurate results to be available. Moreover, using the wall bleeding condition provided in CFD++, it is possible to introduce ablative species in the flow, investigating the effects of ablation for the 3D simulation cases. Finally, the 3D simulation cases should be performed for the rest trajectory points, so that the results can be compared to the flight data and the 2D simulation cases.

Bibliography

[1] John D.Jr. Anderson. An Engineering Survey of Radiating Shock Layers. *AIAA Journal*, 7(9):1665–1675, 1969.

[2] John D.Jr. Anderson. *Hypersonic and high temperature gas dynamics*. American Institute of Aeronautics and Astronautics, Inc, Virginia, second edition, 2000.

[3] AVCO Corporation. Apollo Heat Shield Test Plan. Technical report, 1962.

[4] John J. Bertin. *Hypersonic Aerothermodynamics*. 1994.

[5] John J. Bertin and Russell M. Cummings. Fifty years of hypersonics: where we've been, where we're going. *Progress in Aerospace Sciences*, 39(6-7):511–536, August 2003.

[6] F.S. Billig. Shock-wave shapes around spherical-and cylindrical-nosed bodies. *Journal of Spacecraft and Rockets*, (4):0–1, 1967.

[7] Jay P. Boris and Elaine S. Oran. Numerical Simulation of Reactive Flow. Second Edition. *Measurement Science and Technology*, 12(11):2021–2022, November 2001.

[8] Deepak Bose and Michael J Wright. View-Factor Based Radiation Transport in a Hypersonic Shock Layer. *Journal of Thermophysics and Heat Transfer*, 18(4):553–555, October 2004.

[9] R.K. Crouch and G.D. Walberg. An Investigation of Ablation Behavior of Avcoat 5026/39M Over a Wide Range of Thermal Environments. (April), 1969.

[10] K.T. Edquist, A.A. Dyakonov, M.J. Wright, and C.Y. Tang. Aerothermodynamic environments definition for the Mars Science Laboratory entry capsule. *AIAA paper*, pages 1–21, 2007.

[11] J.A. Fay and N.H. Kemp. Theory of stagnation-point heat transfer in a partially ionized diatomic gas. Technical report, AVCO Corporation, Everett, Massachusetts, 1963.

[12] Gabriel Gnaegi. 3D Numerical Simulation of a re-entry capsule. Technical report, EPFL, Lausanne, 2012.

[13] R.N. Gupta and J.M. Yos. A review of reaction rates and thermodynamic and transport properties for an 11-species air model for chemical and thermal nonequilibrium calculations to 30000 K. *NASA STI/Recon ...*, 1990.

[14] Basil Hassan, Graham V Candler, and David R Olynick. Thermo-chemical nonequilibrium effects on the aerothermodynamics of aerobraking vehicles. *Journal of Spacecraft and Rockets*, 30(6):647–655, November 1993.

[15] E.R. Hillje. Entry flight aerodynamics from Apollo Mission AS-202. (October), 1967.

[16] J. R. Howell. The Monte Carlo Method in Radiative Heat Transfer. *Journal of Heat Transfer*, 120(3):547, August 1998.

[17] P.A. Jacobs, R.J. Gollan, A.J. Denman, B.T. O'Flaherty, D.F. Potter, P.J. Petrie-Repar, and I.A. Johnston. Eilmer s Theory Book : Basic Models for Gas Dynamics and Thermochemistry, 2012.

[18] C.O. Johnston, P.A. Gnoffo, and Alireza Mazaheri. Influence of Coupled Radiation and Ablation on the Aerothermodynamic Environment of Planetary Entry Vehicles. pages 1–36, 2013.

[19] Ojas Joshi. *Fluid-Structure Thermal Coupling And Ablation Effects In Atmospheric Entry.* Phd, EPFL, Lausanne, 2013.

[20] D. B. Lee and W. D. Goodrich. The aerothermodynamic environment of the Apollo command module during superorbital entry. April 1972.

[21] D.B. Lee. Apollo experience report: aerothermodynamics evaluation. (June 1972), 1972.

[22] Derek Liechty, Christopher Johnston, and Mark Lewis. Comparison of DSMC and CFD Solutions of Fire II Including Radiative Heating. *42nd AIAA Thermophysics Conference*, pages 1–14, June 2011.

[23] Y. Liu, D. Prabhu, and K.A. Trumble. Radiation modeling for the reentry of the Stardust sample return capsule. *Journal of Spacecraft ...*, pages 1–21, 2010.

[24] Valentin Marguet. *Ablation-Raditation coupling modeling for Hayabusa reentry vehicle.* Master's, Georgia Tech, 2013.

[25] John Joseph Martin. *Atmospheric reentry: an introduction to its science and engineering.* 1966.

[26] BJ McBride and Sanford Gordon. Computer program for calculating and fitting thermodynamic functions, 1992.

[27] Metacomp. CFD ++ User Manual, 2012.

[28] James N. Moss, Christopher E. Glass, and Francis A. Greene. DSMC Simulations of Apollo Capsule Aerodynamics for Hypersonic Rarefied Conditions. *9th AIAA/ ASM Thermophysics and Heat transfer Conference*, (June):5–8, 2006.

[29] Chul Park. Stagnation-Point Radiation for Apollo 4. *Journal of Thermophysics and Heat Transfer*, 18(3):349–357, July 2004.

[30] Chul Park. Stagnation-Region Heating Environment of the Galileo Probe. *Journal of Thermophysics and Heat Transfer*, 23(3):417–424, July 2009.

[31] Chul Park, Eloret Corporation, and Moffett Field. Chemical-Kinetic Parameters of Hyperbolic Earth Entry. 15(1), 2001.

[32] Chul Park and Seokkwan Yoon. Fully coupled implicit method for thermochemical nonequilibrium air at suborbital flight speeds. *Journal of Spacecraft and Rockets*, 28(1):31–39, January 1991.

[33] J.E. Pavlosky and L.G. Stleger. Apollo experience report: Thermal protection subsystem. (January 1974), 1974.

[34] Daniel F. Potter. *Modelling of radiating shock layers for atmospheric entry at Earth and Mars*. Phd, The University of Queensland, Brisbane, Australia, 2011.

[35] J. D. Ramshaw and C. H. Chang. Ambipolar diffusion in two-temperature multicomponent plasmas. *Plasma Chemistry and Plasma Processing*, 13(3):489–498, September 1993.

[36] Jr. Ried, R.C., W.C. Rochelle, and J.D. Milhoan. Radiative Heating to the Apollo Command Module: Engineering Prediction and Flight Measurement. Technical report, NASA, Manned Spacecraft Center, Houston, Texas, 1972.

[37] L.C. Scalabrin and I.D. Boyd. Numerical simulations of the FIRE-II convective and radiative heating rates. *AIAA Paper*, (June), 2007.

[38] Yannick Schlaeppi. 3D hypersonic numerical simulation of the Phoebus re-entry capsule using NSMB. Technical report, EPFL, Lausanne, 2012.

[39] K. Sutton. Air radiation revisited. In *19th Thermophysics Conference*, Fluid Dynamics and Co-located Conferences. American Institute of Aeronautics and Astronautics, June 1984.

[40] Dabir S. Viswanath, Tushar K. Ghosh, Dasika H.L. Prasad, Nidamarty V.K. Dutt, and Kalipatnapu Y. Rani. *Viscosity of Liquids: Theory, Estimation, Experiment, and Data*. 2010.

[41] Antonio Viviani, Giuseppe Pezzella, and Salvatore Borrelli. Effect of Finite Rate Chemical Models on the Aerothermodynamics of Reentry Capsules. In *15th AIAA International Space Planes and Hypersonic Systems and Technologies Conference*, International Space Planes and Hypersonic Systems and Technologies Conferences. American Institute of Aeronautics and Astronautics, April 2008.

[42] J. B. Vos, P. Leyland, V. Van Kemenade, C. Gacherieu, N. Duquesne, P. Lotstedt, C. Weber, A. Ytterstrom, and C. Saint Requier. NSMB User Guide, 2011.

[43] J. B. Vos, P. Leyland, V. Van Kemenade, C. Gacherieu, N. Duquesne, P. Lotstedt, C. Weber, A. Ytterstrom, and C. Saint Requier. *NSMB Handbook*. 6.0 edition, 2014.

Appendix A

Contours 3D Simulations

In this Appendix the entire solution set of the 3D Simulations performed with CFD++ is presented.

A.1 Perfect gas

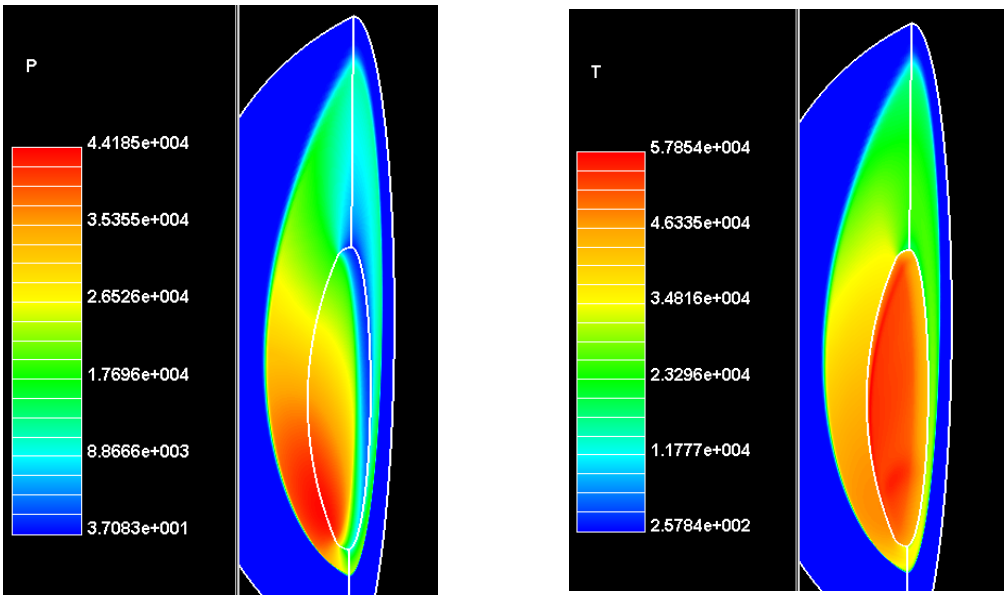

(a) Pressure field

(b) Temperature field

Figure A.1: Pressure and temperature field for perfect gas model

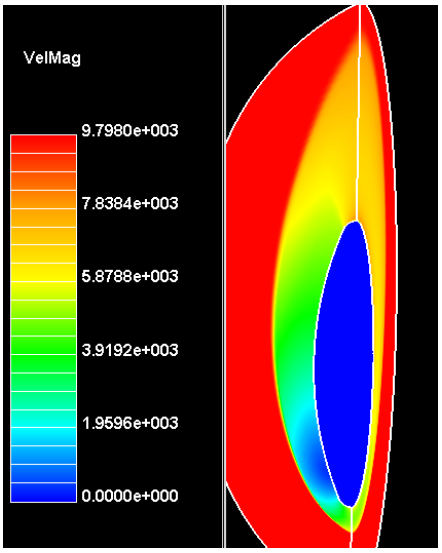

(a) Velocity magnitude field

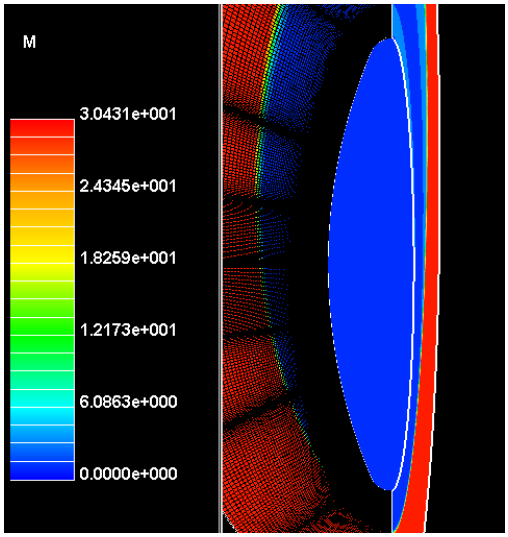

(b) Mach number field- The grid's unsuitability to the flow model

Figure A.2: Mach number and velocity field for perfect gas model

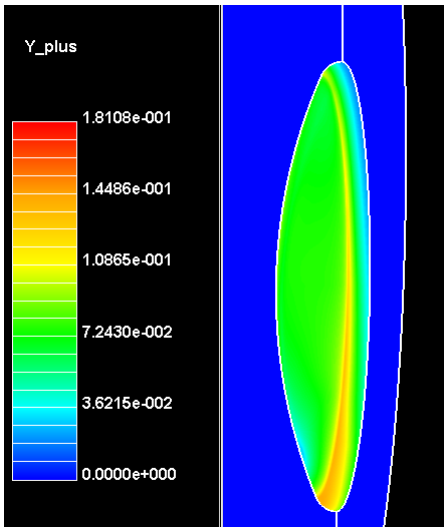

Figure A.3: Y+ for the perfect gas model case

A.2 5-species equilibrium

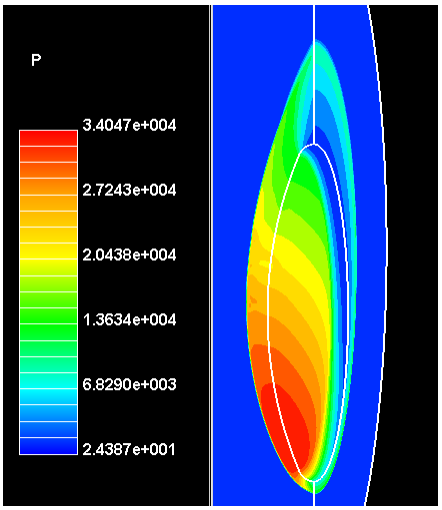

(a) Pressure field

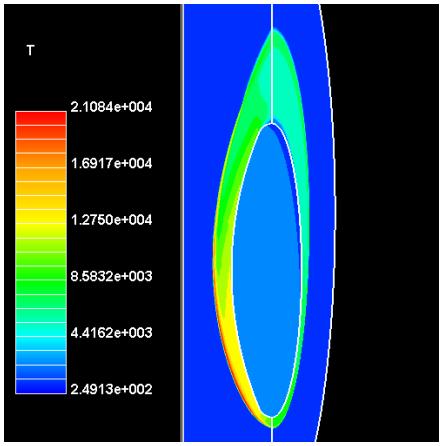

(b) Temperature field

Figure A.4: Pressure and temperature field

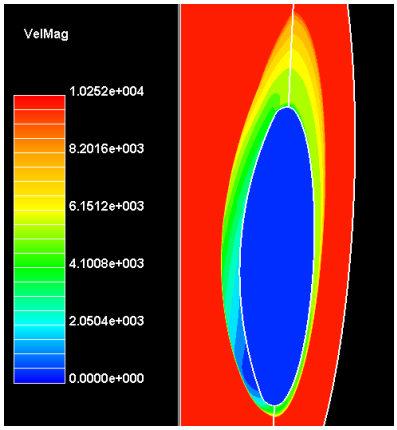

(a) Velocity magnitude field

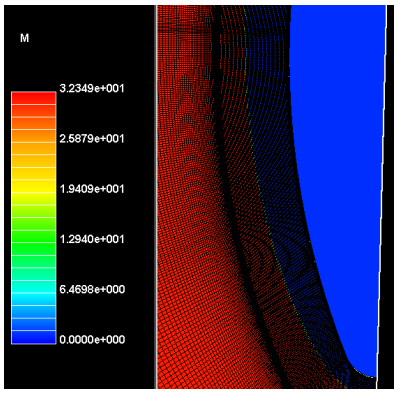

(b) Mach number field

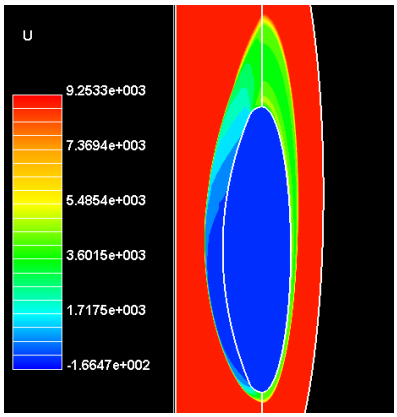

(c) u Velocity field

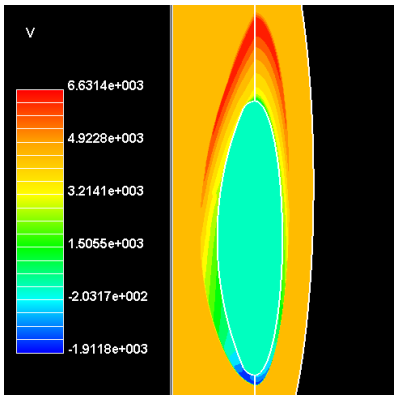

(d) v Velocity field

Figure A.5: Mach number and velocity field

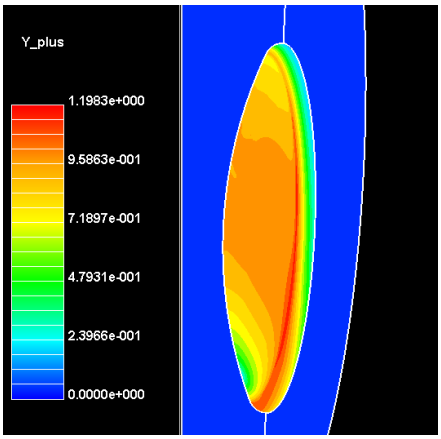

(a) Y+ field

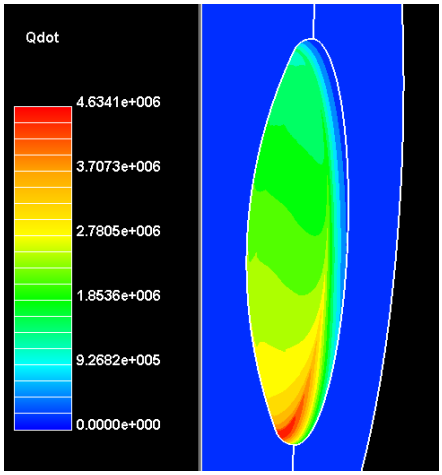

(b) Conductive heat flux field

Figure A.6: Surface parameters

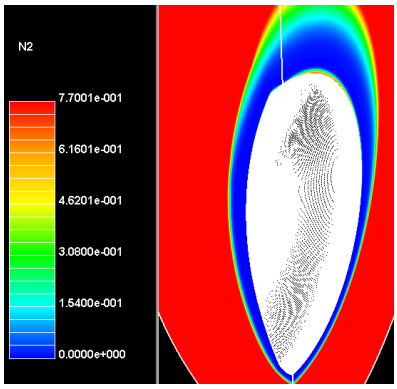

(a) N_2 is consumed by dissociation and exchange reactions

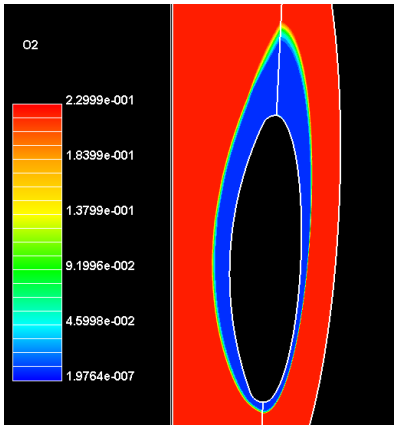

(b) O_2 is consumed by dissociation and exchange reactions

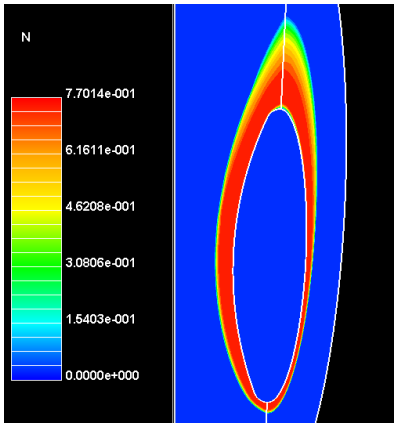

(c) N is produced by the shock-layer reactions

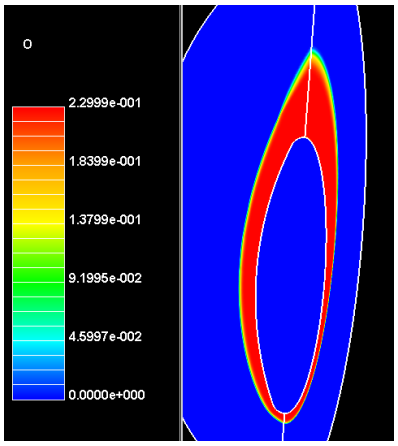

(d) O is increasing due to the shock-layer reactions

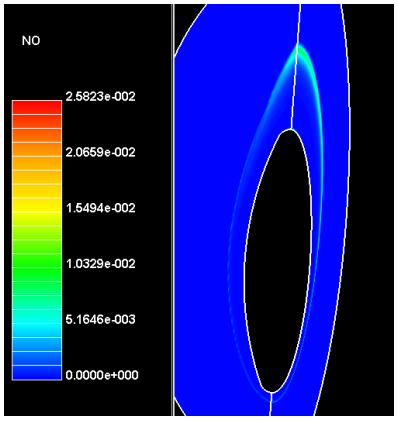

(e) NO is produced and quickly consumed by dissociation reactions

Figure A.7: Species distributions for the 5 species equilibrium case

A.3 5-species non-equilibrium

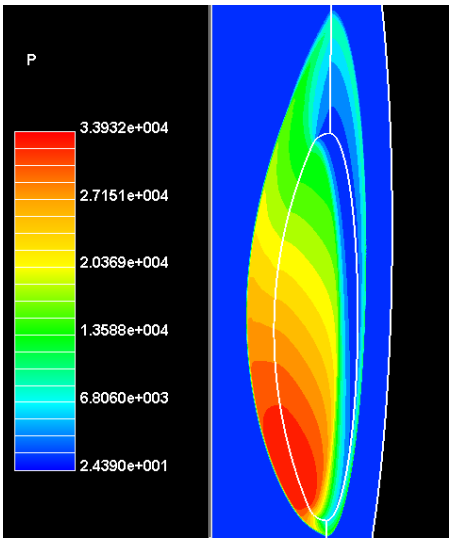

(a) Pressure field

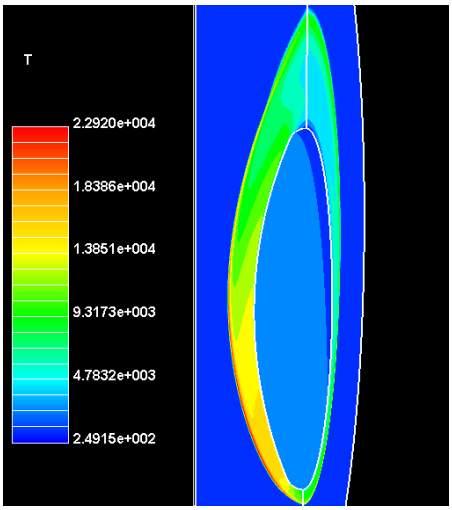

(b) Temperature field

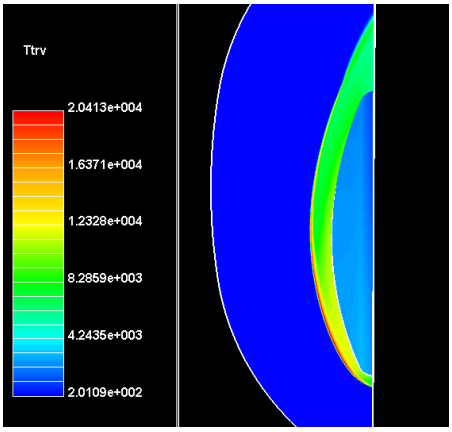

(c) Translational temperature

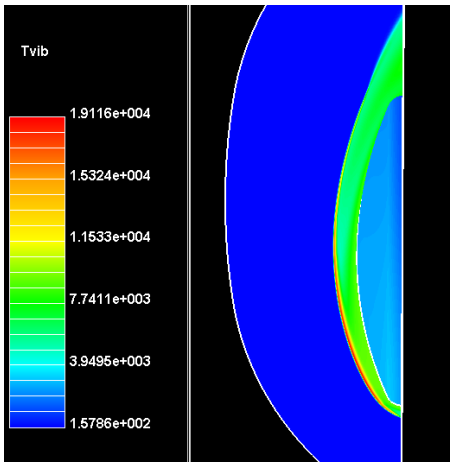

(d) Vibrational temperature

Figure A.8: Pressure and temperature field

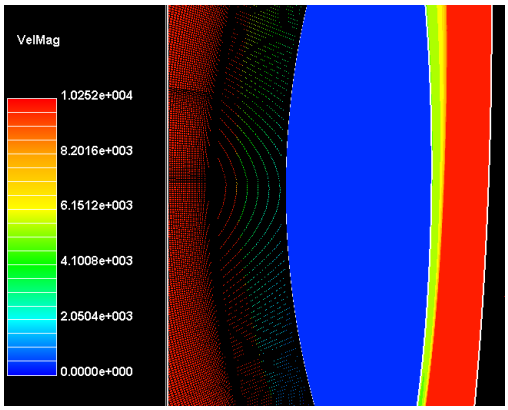

(a) Velocity magnitude field

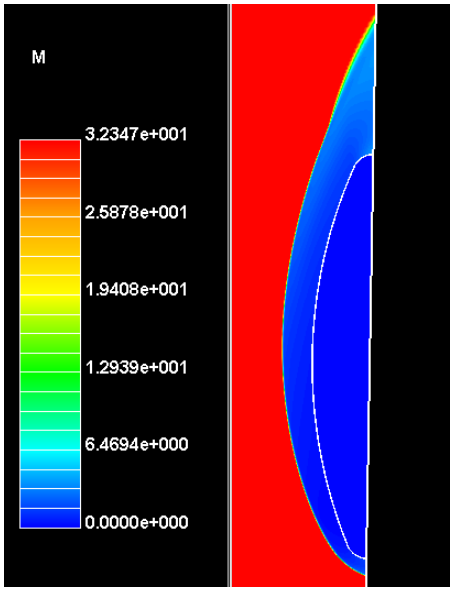

(b) Mach number field

Figure A.9: Mach number and velocity field

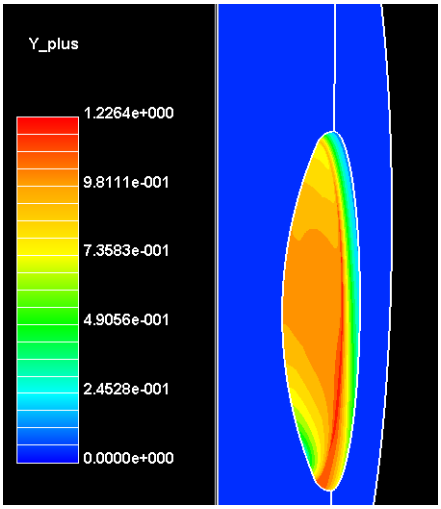

(a) Y+ field

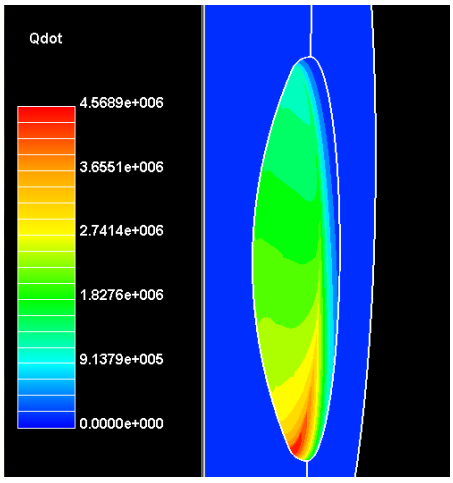

(b) Conductive heat flux field

Figure A.10: Surface parameters

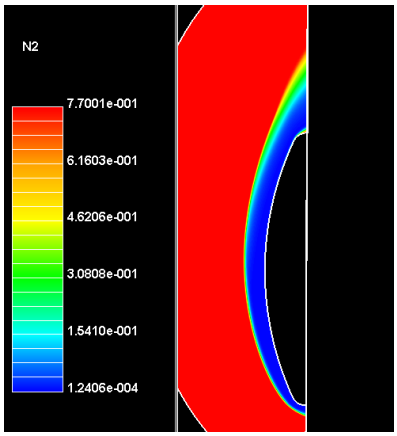

(a) N_2

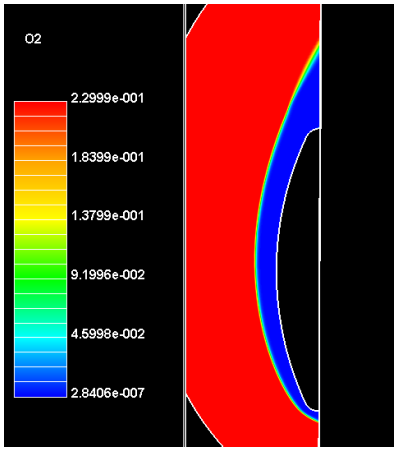

(b) O_2

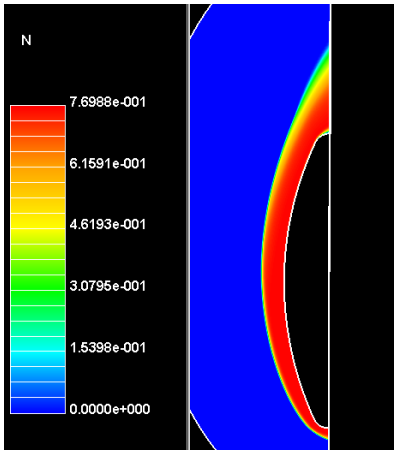

(c) N

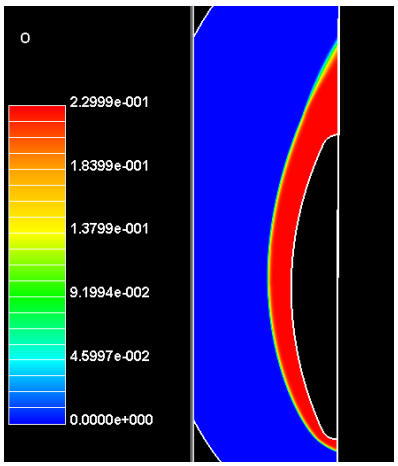

(d) O

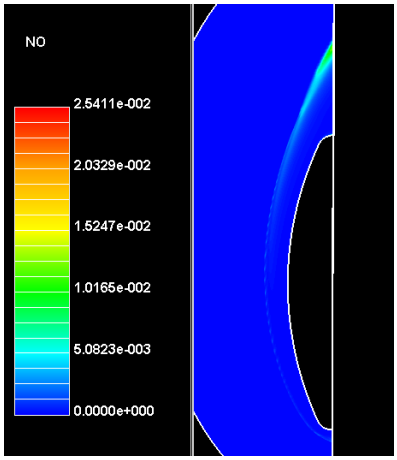

(e) NO

Figure A.11: Species distributions for the 5 species non-equilibrium case

A.4 11-species equilibrium

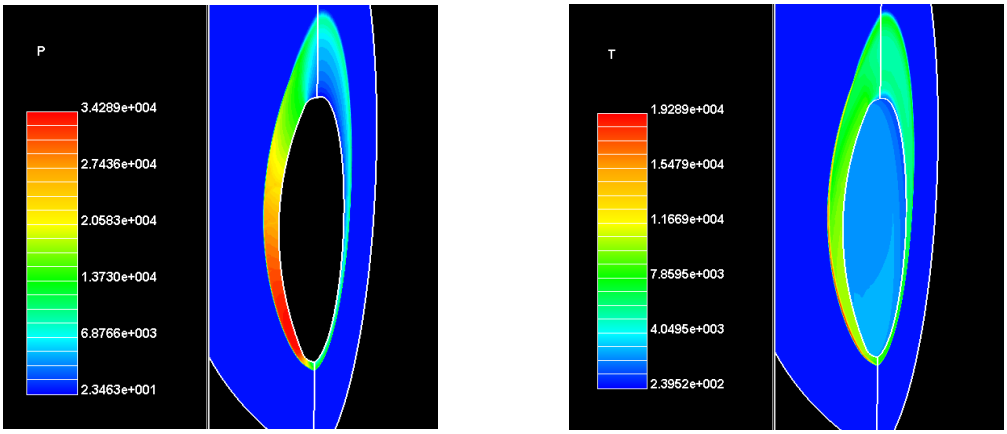

(a) Pressure field **(b)** Temperature field

Figure A.12: Pressure and temperature field

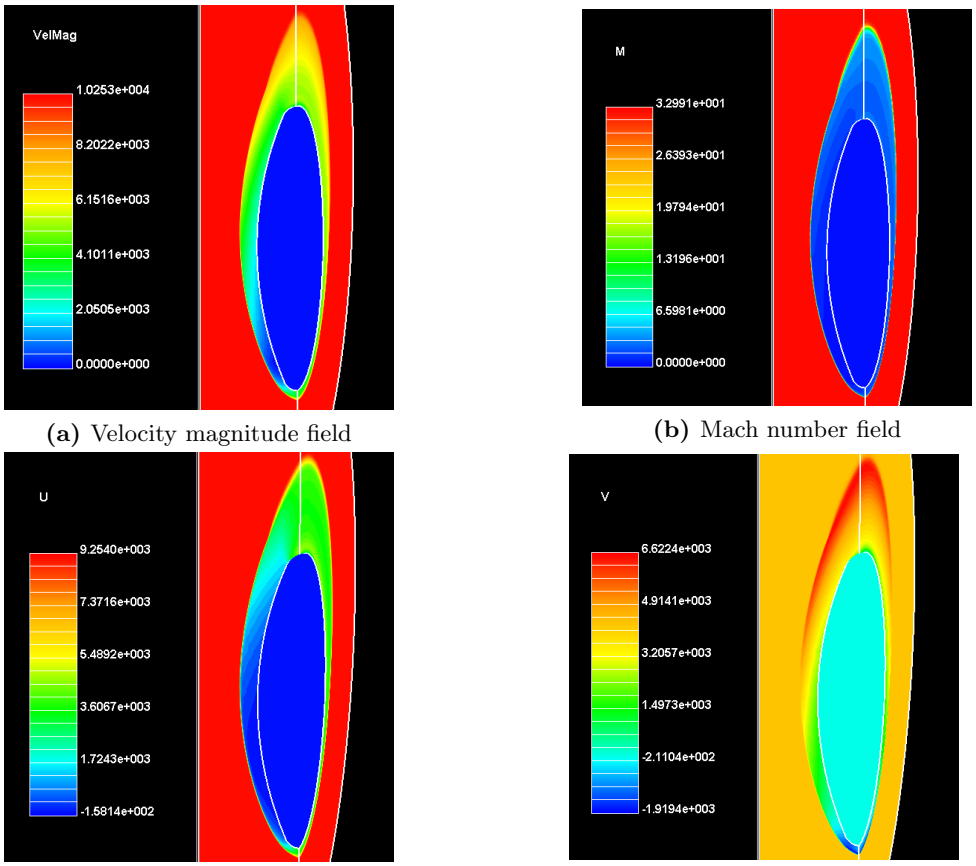

(a) Velocity magnitude field **(b)** Mach number field

(c) u Velocity field **(d)** v Velocity field

Figure A.13: Mach number and velocity field

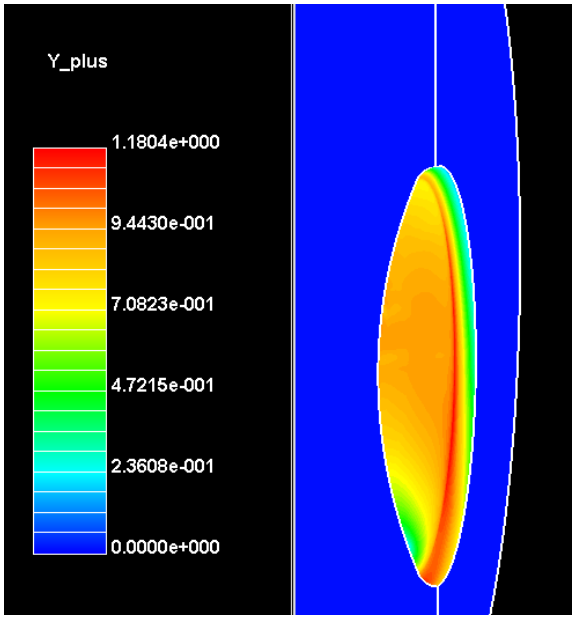

(a) Y+ field

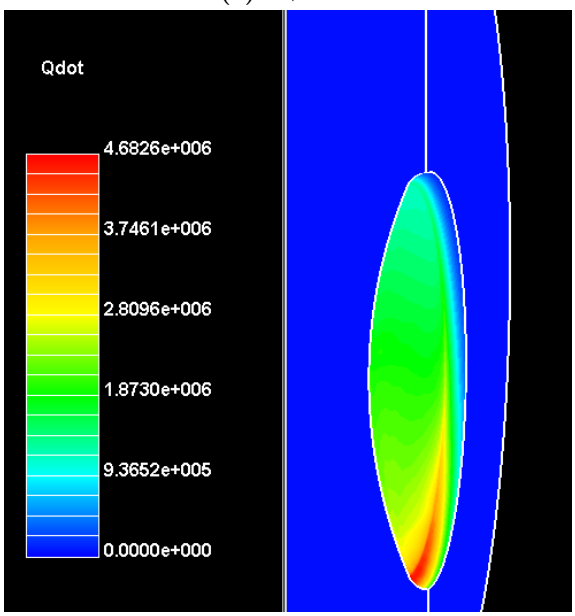

(b) Conductive heat flux field

Figure A.14: Surface parameters

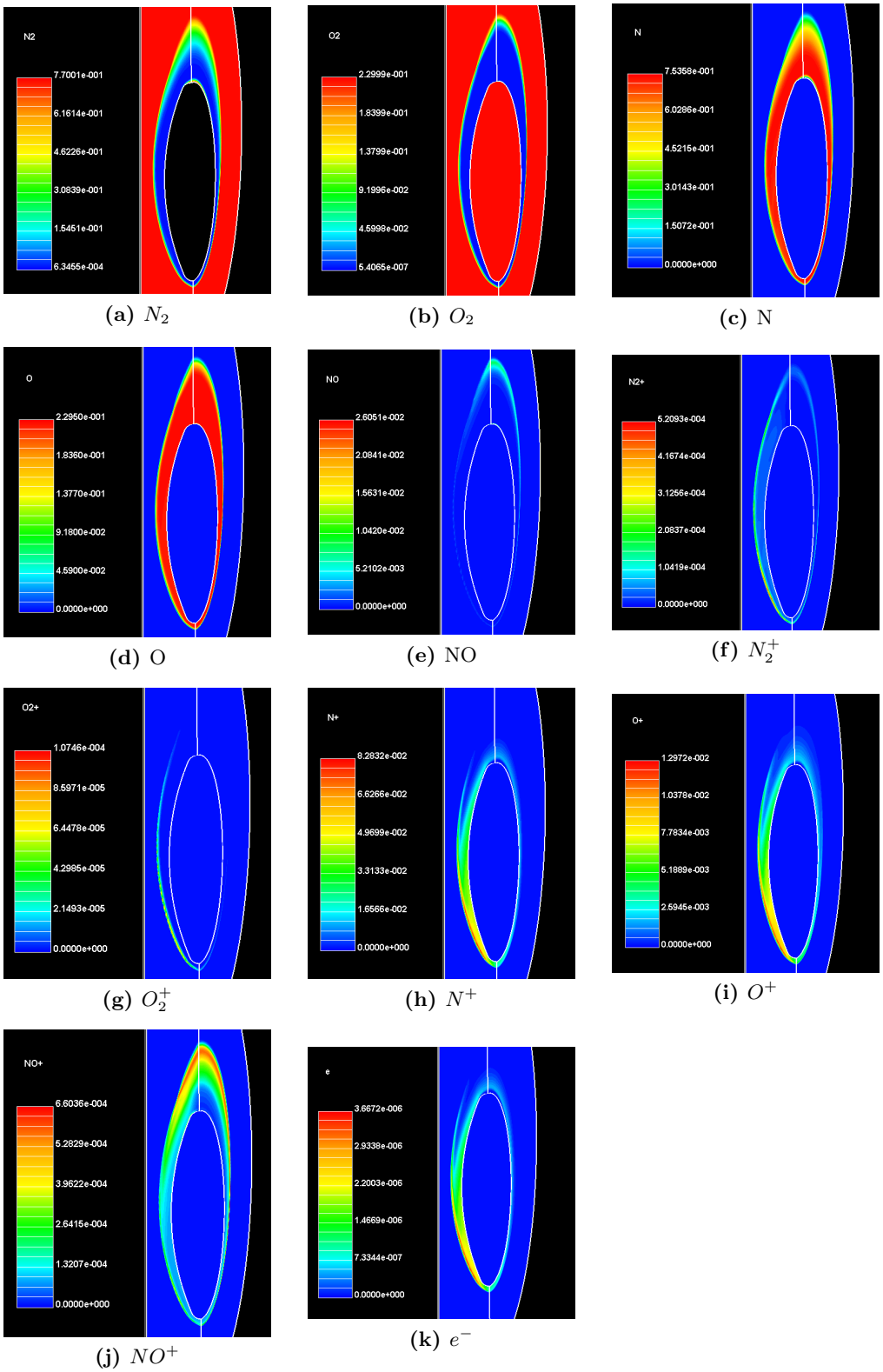

(a) N_2 **(b)** O_2 **(c)** N

(d) O **(e)** NO **(f)** N_2^+

(g) O_2^+ **(h)** N^+ **(i)** O^+

(j) NO^+ **(k)** e^-

Figure A.15: Species distributions for the 11 species equilibrium case

A.5 11-species non-equilibrium

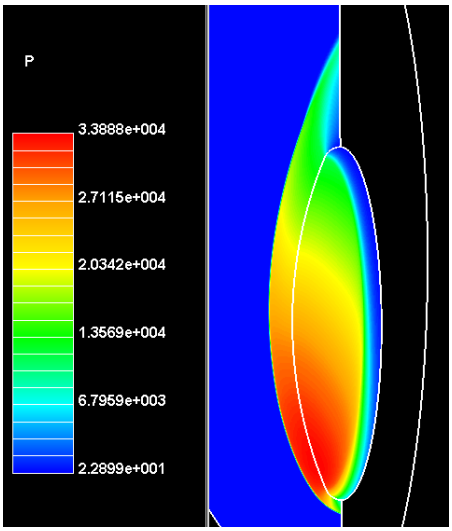

(a) Pressure field

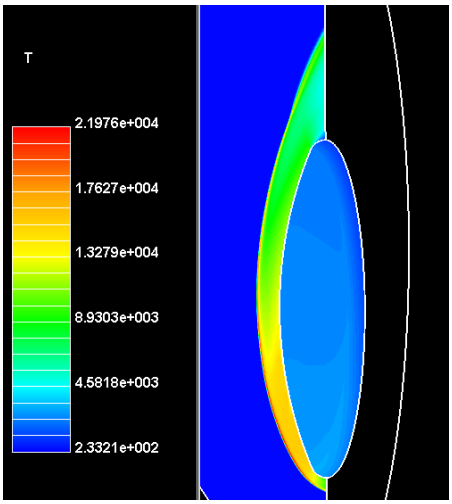

(b) Temperature field

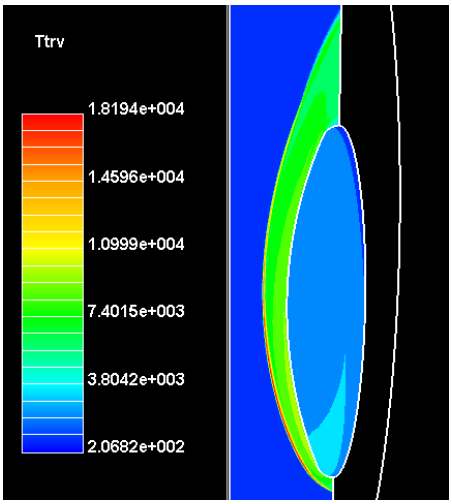

(c) Translational temperature

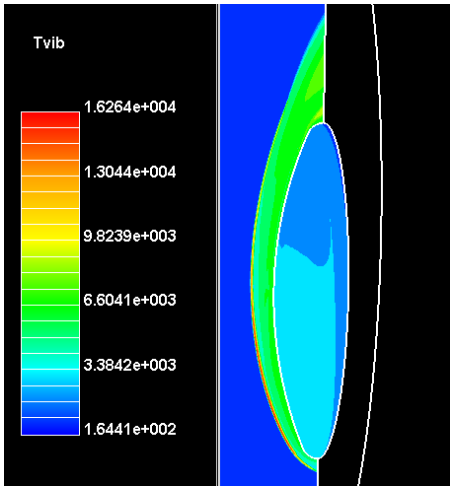

(d) Vibrational temperature

Figure A.16: Pressure and temperature field

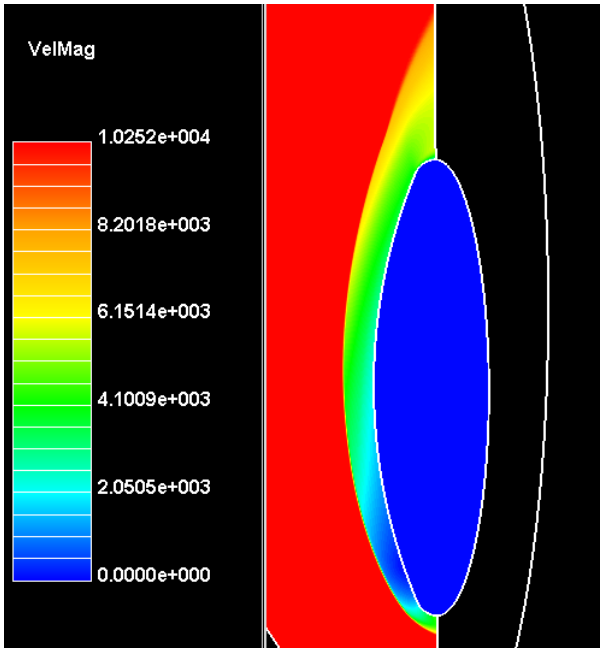

Figure A.17: Velocity field

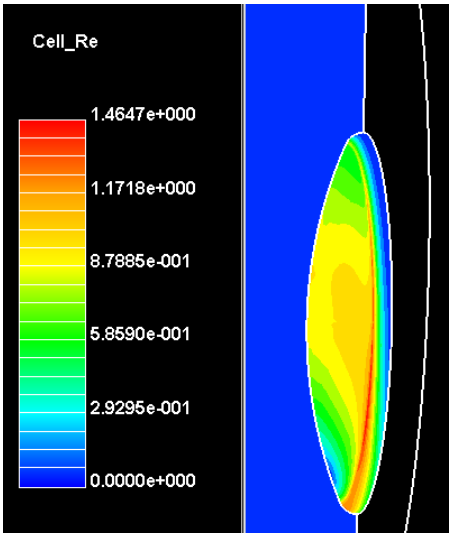

(a) Cell Reynolds Number

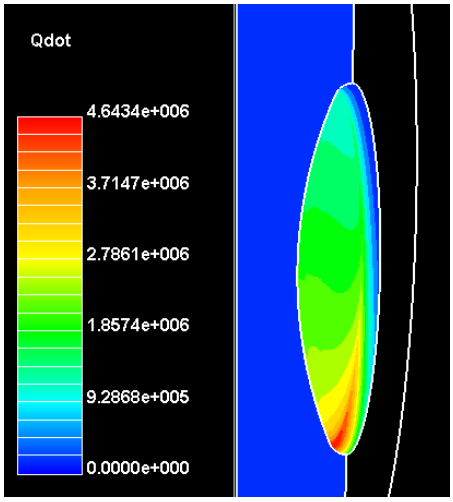

(b) Conductive heat flux field

Figure A.18: Surface parameters

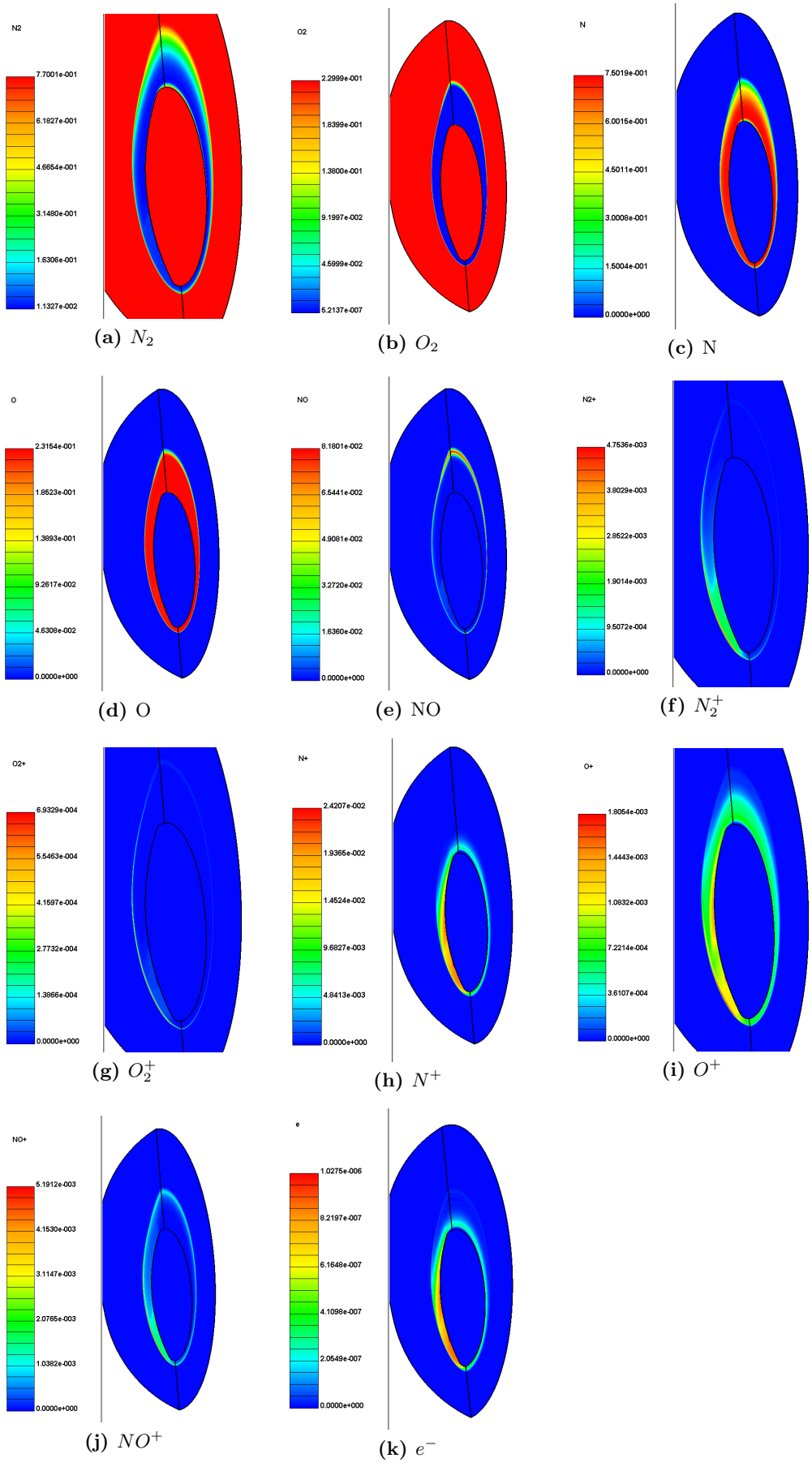

(a) N_2 **(b)** O_2 **(c)** N

(d) O **(e)** NO **(f)** N_2^+

(g) O_2^+ **(h)** N^+ **(i)** O^+

(j) NO^+ **(k)** e^-

Figure A.19: Species distributions for the 11 species non-equilibrium case